Chapter 7 | Application of Radiative Transfer Principles to Remote Sensing

7.1 Introduction

Remote sensing is differentiated from *in situ* measurements whereby specific observations are made within the medium. Remote sensing involves the interpretation and inversion of radiometric measurements of electromagnetic radiation measured some distance away, where the radiation is characterized by a specific wavelength that is sensitive to some physical aspect of the medium. The interpretation and inversion require the use of fundamental light scattering and radiative transfer theories. The physical principle of remote sensing can be understood from the simple configuration illustrated in Fig. 7.1. Basically, an electromagnetic signal is recorded by a detector after it interacts with a target containing molecules, particulates, and/or surfaces. If T and S denote the target and signal, respectively, then we may write symbolically

$$S = F(T),$$

where F represents a function, not necessarily linear. This function governs the processes involving the transfer of electromagnetic radiation. The inverse of the preceding relation gives

$$T = F^{-1}(S),$$

where F^{-1} represents a function of F. Generally, if a functional relationship can be established, one may carry out the inversion directly. However, because of the complexity of F, its inverse cannot be performed in a straightforward manner. In those cases where a specific functional form does not exist, one may search the desired parameters of the target that would best fit the measured signals.

The fundamental obstacle in all remote sensing inversion problems is the *uniqueness* of the solution. The nonuniqueness arises because the medium under investigation may be composed of a number of unknown parameters, a combination of which may lead to the same radiation signature. In addition to this physical problem, there are also mathematical problems associated with the existence and stability of the solution, and the manner in which the solution is constructed.

There are two basic types of remote sensing: *active* and *passive*. Active remote sensing employs a radiation source generated by artificial means such as the lasers
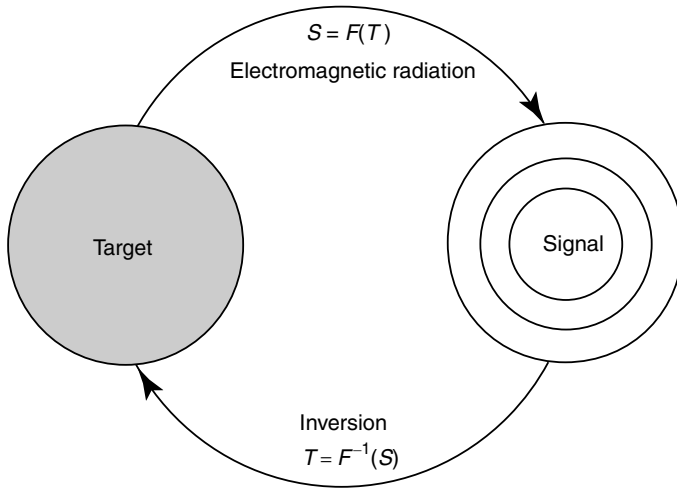
Figure 7.1   Principle of remote sensing. The symbols T and S denote target and signal, respectively, F represents a function which is generally nonlinear and cannot be represented by analytic equations, and F^{-1} is the inverse of this complicated function.

used in lidar or the microwaves used in radar. The radiant energy source corresponding to a specific wavelength is sent to the atmosphere. Some of the energy is scattered back to the detector and recorded. From the recorded scattered energy, one analyzes the composition and structure of the atmosphere with which the radiant energy has interacted. Active remote sensing is normally concerned with backscattering; i.e., the transmitter and detector are collocated. In recent years, significant developments in lidar systems based on differential absorption and depolarization techniques and in millimeter (mm)-wave radar have been made in conjunction with the detection of aerosols, clouds, water vapor, and trace gases. Deployment of lidar and mm-wave radar on space platforms is being continuously explored in ongoing research and development programs.

Passive remote sensing utilizes the natural radiation sources of the sun or the earth–atmosphere system. For example, spectral solar radiation interacts with a cloud and leaves a scattered signature, which may be used for its identification. Similarly, spectral thermal infrared or microwave radiation emitted from the earth–atmosphere system may be utilized to understand its thermodynamic state and composition. In reference to Fig. 1.1 regarding the electromagnetic spectrum, all wavelengths are possible from the emitting medium. However, for atmospheric applications, the ultraviolet (UV), visible, infrared (IR), and microwave spectra are most important.

Passive remote sensing allows the global inference of atmospheric and surface temperatures, composition profiles, surface properties, and radiative budget components from orbiting meteorological satellites. The first meteorological satellite experiment was an array of hemispheric sensors flown on the Explorer 7 satellite launched in 1959 to measure the radiation balance of the earth–atmosphere system. Shortly after,

a five-channel scanning radiometer was carried on board TIROS 2. The scanning radiometer has provided the general characteristics of sounding instrumentation for research and operational satellites over the past four decades. In April 1969, two spectrometers providing spatial infrared measurements for the determination of the vertical profiles of temperature, water vapor, and ozone were flown on the Nimbus 3 satellite. On board was another instrument for measuring reflected UV radiation, which allowed the determination of the global ozone concentration. Also on board was an infrared radiation interferometer spectrometer (IRIS) for measurement of the emitted infrared spectrum. The concept of using the detailed emission spectrum for remote sensing and climate studies has been revisited only recently. The launch of Nimbus 5 in December 1972 marked the first use of microwave techniques for the remote sensing of atmospheric temperature and total water content. These are the key milestones of atmospheric sounding from orbiting meteorological satellites.

In this chapter, we first discuss the information content of transmitted and reflected sunlight. Following a description of the principle of temperature and gaseous profile determination from thermal infrared emission, the use of microwave emissions for atmospheric studies is introduced. These sections emphasize the application of radiative transfer principles to the remote sensing of atmospheric temperature, aerosols, ozone, water vapor, clouds, and precipitation from satellites. The principle of active remote sensing utilizing backscattered energy is subsequently presented with an emphasis on the propagation of laser energy in the atmosphere. Determination of the radiation budget of the earth–atmosphere system from satellites for use in radiation and climate studies will be discussed in Chapter 8.

7.2   Remote Sensing Using Transmitted Sunlight

The remote sensing of aerosols and ozone from ground-based radiometers utilizes the direct beam of solar radiation transmitted through the cloudless atmosphere. Specific wavelengths in the UV and visible spectra are normally selected to optimize the effects of aerosols and ozone for retrieval purposes. Considering the geometry illustrated in Fig. 7.2 and following the Beer–Bouguer–Lambert law presented in Section 1.4.2, the solar intensity of a given wavelength measured at the ground at a given time of the year can be written in the form

$$\hat{I}(\lambda) = \left(\frac{r_0}{r}\right)^2 I_\odot(\lambda) \exp[-\tau(\lambda)m(\theta_0)], \tag{7.2.1}$$

where r and r_0 are the actual and mean sun-earth distances, respectively (Section 2.2.1); $I_\odot$ denotes the known solar intensity at the top of the atmosphere corresponding to r_0; the air mass factor $m(\theta_0) = 1/\cos\theta_0$, where θ_0 is the solar zenith angle involving the latitude, the solar declination angle, and the hour angle defined in Eq. (2.2.1); and the total optical depth is the sum of the individual values contributed from aerosols (A), Rayleigh molecules (R), ozone (3) and nitrogen dioxide (2), respectively, as follows:

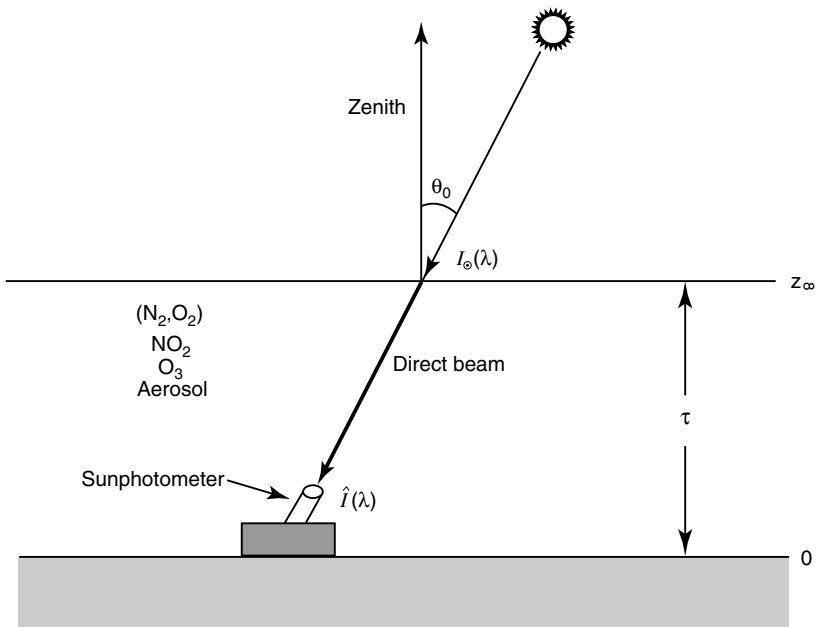$$\tau(\lambda) = \tau_A(\lambda) + \tau_R(\lambda) + \tau_3(\lambda) + \tau_2(\lambda). \tag{7.2.2}$$

Figure 7.2   Geometry of a ground-based radiometer for the measurement of a direct solar beam. The solar zenith angle is defined by θ_0, the optical depth is denoted by τ, and the solar intensity and measured intensity are given by $I_\odot$ and $\hat{I}$, respectively. A sunphotometer can have a number of different filters to record direct solar radiation in component wavelengths.

The optical depths of Rayleigh molecules and NO_2 for a given wavelength (Section 3.3.1) are generally assumed to be known quantities in the determination of aerosol and ozone properties.

7.2.1   Determination of Aerosol Optical Depth and Size Distribution

In Section 5.1, we reviewed the origin of atmospheric aerosols. Aerosols not only scatter, but can also absorb incoming sunlight. Various kinds of aerosols can have a significant effect on the radiative balance of the earth–atmosphere system and hence on the earth's climate because of their global presence. Increasing concerns that aerosols in general and man-made pollution in particular have caused worldwide weather disturbances have prompted intensified observation of the concentrations and physical and chemical characteristics of aerosols from the ground and space. Determination of the optical properties of aerosols and their size distribution around the globe has been a significant contemporary research effort of late.

Observational methods to determine the dust loading of the atmosphere were developed during the 1920s by Linke and Ångström. In essence, aerosol total optical depth, sometimes also referred to as *turbidity,* is derived from direct spectral solar intensity measured on the ground. Wavelengths in the visible spectrum are normally

employed because absorption due to water vapor can be neglected and the effect of ozone absorption is small.

From Eqs. (7.2.1) and (7.2.2), aerosol optical depth is given by

$$\tau_A(\lambda) = \frac{1}{m(\theta_0)}[\ln I^*(\lambda) - \ln \hat{I}(\lambda)] - [\tau_R(\lambda) + \tau_3(\lambda) + \tau_2(\lambda)], \qquad (7.2.3a)$$

where we define $I^* = I_\odot(r_0/r)^2$. This term can be evaluated from the known solar spectral data or can be directly evaluated from the Langley plot (Section 2.3.2). In the determination of aerosol optical depth, the optical depths associated with NO_2 and O_3 molecules are usually computed from the following parameterizations:

$$\tau_R(\lambda) = (a + bH)\lambda^{-(c+d\lambda+e/\lambda)}p/p_s,$$
$$\tau_2(\lambda) = k_2(\lambda)\,C(NO_2), \qquad (7.2.3b)$$
$$\tau_3(\lambda) = k_3(\lambda)\,C(O_3),$$

where the empirical coefficients for Rayleigh scattering are $a = 0.00864$, $b = 6.5 \times 10^{-6}$, $c = 3.916$, $d = 0.074$, and $e = 0.050$; H is the radiometer height in kilometers; p is atmospheric pressure at the radiometer; p_s is 1013.25 mb; k_2 and k_3 are absorption coefficients for NO_2 and O_3, respectively; and C denotes the concentration notation and $C(NO_2) \cong 4 \times 10^{15}$ cm^{-2}. Table 7.1 lists the pertinent values of six typical wavelengths used for aerosol measurements (Russell *et al.,* 1993). Ozone concentration is determined using other methods (see Section 7.2.2). Further, some diffuse light that enters the radiometer can be taken into account by empirical adjustments. Thus, once these optical depths have been evaluated and the position of the sun is known, a measurement of the direct solar intensity can be used to infer the aerosol optical depth. In the following, we wish to show that in addition to the optical depth, the aerosol size distribution can also be retrieved. We shall first demonstrate the principle of using two wavelengths for this purpose.

The aerosol optical depth corresponding to the entire atmospheric column can be expressed in terms of the extinction coefficient in the form

$$\tau_A(\lambda) = \int_0^{z_\infty} \beta_e(\lambda, z)\,dz. \qquad (7.2.4)$$

Let the height-dependent aerosol size distribution be defined by $n(z, a)(\text{cm}^{-3}\mu\text{m}^{-1})$.

Table 7.1

Useful Scattering or Absorption Coefficients for a Number of Solar Wavelengths for Molecules, O_3, and NO_2

$\lambda(\mu m)$	0.382	0.451	0.526	0.778	0.861	1.060
k_R	0.4407	0.2198	0.1175	0.0240	0.0159	0.00069
k_3 (atm − cm^{-1})	—	0.004	0.061	0.009	—	—
k_2 (cm^2)	5.39×10^{-19}	4.66×10^{-19}	1.74×10^{-19}	—	—	—

Then the extinction coefficient (cm^{-1}) is given in the form [Eq. (5.2.115)]

$$\beta_e(\lambda, z) = \int_{a_1}^{a_2} \sigma_e(a, \lambda) n(z, a) \, da, \qquad (7.2.5)$$

where σ_e represents the extinction cross section (cm^2) for an individual particle. The size distribution of aerosols in the atmosphere has been a subject of extensive research in the past four decades, as pointed out in Section 5.1. For the purpose of discussing retrieval, the aerosol size distribution can best be defined by the Junge distribution displayed in Fig. 5.1 in the form

$$n(z, a) = C(z, a) a^{-(\nu^*+1)}, \qquad (7.2.6)$$

where C is a scaling factor directly proportional to the aerosol concentration and is, therefore, a function of height z in the atmosphere, and ν^* represents a shaping constant which is normally found to lie in the range $2 \le \nu^* < 4$. As shown in Fig. 5.1, the size distribution of aerosols typically covers the range from about 0.01 to about 10 μm.

Using the Junge size distribution, the aerosol optical depth is given by

$$\tau_A(\lambda) = k\lambda^{(-\nu^*+2)}, \qquad (7.2.7)$$

where k is a certain constant (see Exercise 7.1). When $\nu^* = 3.3$, k is known as the *Ångström turbidity coefficient*. If the aerosol optical depth is measured at two wavelengths, then we have

$$\hat{z} = \frac{\tau_A(\lambda_1)}{\tau_A(\lambda_2)} = \left(\frac{\lambda_1}{\lambda_2}\right)^{(-\nu^*+2)} = y^{(-\nu^*+2)}. \qquad (7.2.8a)$$

Thus, the shaping factor can be inferred from

$$\nu^* = 2 - \ln \hat{z} / \ln y. \qquad (7.2.8b)$$

We may also retrieve the aerosol size distribution directly if a number of aerosol optical depths are measured with a multispectral instrument known as a *sunphotometer* (Fig. 7.2). A sunphotometer tracks the sun and measures the intensity of a solar beam in several spectral channels. For the retrieval of aerosol size distribution, we shall use Eqs. (7.2.4)–(7.2.6) and define the column aerosol size distribution in the form

$$n_c(a) = \int_0^{z_\infty} n(a, z) \, dz = f(a) h(a), \qquad (7.2.9.a)$$

where we have separated $n_c(a)$ into slowly and rapidly varying functions represented by $f(a)$ and $h(a) = a^{-(\nu^*+1)}$, respectively (King *et al.,* 1978). Thus, we have

$$\tau_A(\lambda) = \int_{a_1}^{a_2} f(a)[h(a)\pi a^2 Q_e(m, a/\lambda)] \, da. \qquad (7.2.9.b)$$

In Eq. (7.2.9b), we have expressed, based on the Lorenz–Mie theory, the extinction cross section in terms of the extinction efficiency Q_e, which is a function of the

aerosol radius, wavelength, and complex refractive index. In the retrieval, the refractive index for aerosols must first be assigned. The objective of the retrieval is now to determine $f(a)$.

To simplify the introduction of the inversion method we let $g = \tau_A(\lambda)$ and $K_\lambda(a) = \pi a^2 Q_e(m, a/\lambda)h(a)$. Thus, we have

$$g_\lambda = \int_{a_1}^{a_2} f(a)K_\lambda(a)\,da. \tag{7.2.10}$$

This is the well-known Fredholm equation of the first kind in which $K_\lambda(a)$, the weighting function, is the kernel, and $f(a)$ is the function to be recovered from a set of g_λ. In practice, because only finite values of g_λ are available, the solution for $f(a)$ is mathematically ill-conditioned, even if the weighting function and the measured data are without errors.

Weighting functions based on Lorenz–Mie calculations involving seven sunphotometer wavelengths for a typical Junge aerosol size distribution are illustrated in Fig. 7.3. The peaks of the weighting functions shift from larger to smaller radius
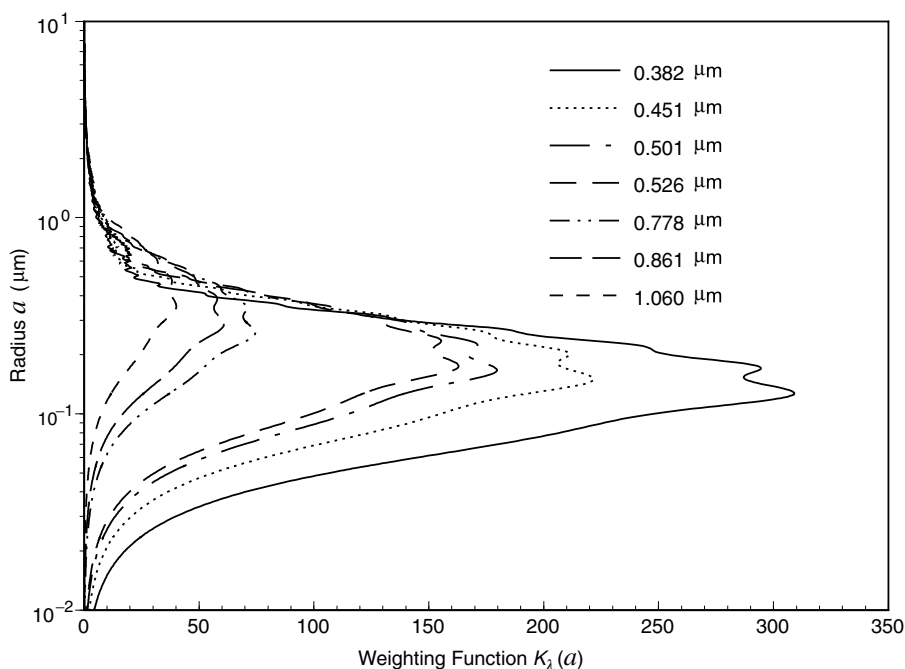

Figure 7.3   Weighting function as a function of aerosol radius for seven sunphotometer wavelengths. The calculations use the Junge size distribution depicted in Fig. 5.1 with $\nu^* = 3$ and an index of refraction of 1.45. The second peak above the maximum for each weighting function is associated with the extinction efficiency curve computed from the Lorenz–Mie spherical particles (see Fig. 5.7 for $m_i = 0$).

corresponding to the increase in wavelength. The weighting functions cover a range of aerosol radii from about 0.01 to 1 μm. In the following, we introduce the direct linear inversion method, which has been frequently used for the retrieval of aerosol size distribution.

7.2.1.1   DIRECT LINEAR INVERSION

Consider the following Fredholm equation of the first kind:

$$g_i = \int_{a_1}^{a_2} f(a)K_i(a)\,da, \qquad i = 1, 2, \ldots, M, \qquad (7.2.11)$$

where the index i (replacing λ) denotes a discrete set of M observations. Thus, a set of M integral equations is to be used to recover the unknown function $f(a)$ given the known kernels $K_i(a)$. It is clear that the solution is an ill-posed problem, because the unknown profile is a continuous function of particle radius and because only a finite number of observations are available.

It is convenient to express $f(a)$ in a series such that

$$f(a) = \sum_{j=1}^{N} f_j W_j(a), \qquad (7.2.12)$$

where f_j are unknown coefficients and W_j are the known representation functions, which can be orthogonal functions, such as polynomials or Fourier series. Substituting Eq. (7.2.12) into Eq. (7.2.11) we obtain

$$g_i = \sum_{j=1}^{N} A_{ij} f_j, \qquad i = 1, 2, \ldots, M, \qquad (7.2.13a)$$

where

$$A_{ij} = \int_{a_1}^{a_2} W_j(a)K_i(a)\,da. \qquad (7.2.13b)$$

To find $f_j(j = 1, \ldots, N)$, we require the observations $g_i(i = 1, \ldots, M)$ and the general condition that $M \geq N$.

For convenience of analysis, we can use vectors and matrices to represent the fundamental parameters. The observations and unknown coefficients are denoted by the following column vectors:

$$\mathbf{g} = \begin{bmatrix} g_1 \\ g_2 \\ \vdots \\ g_M \end{bmatrix}, \quad \mathbf{f} = \begin{bmatrix} f_1 \\ f_2 \\ \vdots \\ f_N \end{bmatrix}. \qquad (7.2.14a)$$

A matrix consisting of M rows and N columns is defined by

$$\mathbf{A} = \begin{bmatrix} A_{11} & A_{12} & \cdots & A_{1N} \\ A_{21} & A_{22} & \cdots & A_{2N} \\ \vdots & \vdots & & \\ A_{M1} & A_{M2} & \cdots & A_{MN} \end{bmatrix}. \tag{7.2.14b}$$

$\mathbf{A}$ is said to be an $(M \times N)$ matrix and can also be written as $\|A_{ij}\|$. Thus, Eq. (7.2.13a) can be expressed in matrix form:

$$\mathbf{g} = \mathbf{Af}. \tag{7.2.15}$$

The inverse of a matrix is denoted by $\mathbf{A}^{-1}$. In general, the inverse exists only when $\mathbf{A}$ is a square $(N \times N)$ and the determinant of the array set $(\mathbf{A})$ is not zero (nonsingular). Inversion of a matrix usually requires a computer. If $M = N$, then we can obtain $\mathbf{f}$ from direct inversion as follows:

$$\mathbf{f} = \mathbf{A}^{-1}\mathbf{g}. \tag{7.2.16}$$

Exercise 7.2 requires the direct inversion of a known mathematical function.

If $M > N$, i.e., the number of observations is more than the terms for the representation function, Eq. (7.2.15) cannot be inverted directly because there are more equations than unknowns, leading to the problem that the system is overdetermined. In practical terms, the matrix $\mathbf{A}$ cannot be inverted. The conventional approach to such a problem is to use the method of least squares. The difference between the left- and right-hand sides of Eq. (7.2.13a) can be written in the form

$$\varepsilon_i = g_i - \sum_{j=1}^{N} A_{ij} f_j, \qquad i = 1, 2, \ldots, M. \tag{7.2.17}$$

The least squares solution minimizes the quantity

$$\sum_{i=1}^{M} \varepsilon_i{}^2 = \sum_{i=1}^{M} \left(\sum_{j=1}^{N} A_{ij} f_j - g_i \right)^2 \tag{7.2.18a}$$

by setting the partial derivatives of this term with respect to $f_k (k = 1, 2, \ldots, N)$ equal to zero so that

$$\frac{\partial}{\partial f_k} \left[\sum_{i} \left(\sum_{j=1}^{N} A_{ij} f_j - g_i \right)^2 \right] = 0. \tag{7.2.18b}$$

Performing the operation leads to

$$\sum_{i} \left(\sum_{j=1}^{N} A_{ij} f_j - g_i \right) A_{ik} = 0. \tag{7.2.18c}$$

In matrix form, we have

$$\mathbf{A}^{\mathsf{T}}\mathbf{Af} = \mathbf{A}^{\mathsf{T}}\mathbf{g}, \tag{7.2.19}$$

where $\mathbf{A}^T$ is the transpose of $\mathbf{A}$, i.e., an $(N \times M)$ matrix. It follows that

$$\mathbf{f} = (\mathbf{A}^T\mathbf{A})^{-1}\mathbf{A}^T\mathbf{g}. \tag{7.2.20}$$

This is the least squares solution which requires the inverse of a symmetric and square matrix. Many studies have pointed out that the solution derived from Eq. (7.2.20) is unstable because it is under constraint.

7.2.1.2 CONSTRAINED LINEAR INVERSION

In addition to the instability due to the governing mathematical function itself, instability can also be traced to the following sources of error: (a) errors produced by the numerical quadrature used for the calculation of A_{ij} in Eq. (7.2.13b); and (b) numerical round-off errors. Further, radiometers have inherent instrument noise and thus the observed intensities probably generate errors in a random fashion. All of the preceding errors make direct inversion from the integral transfer equation impractical. In practice, the true g_i are never known and the measured data can be expressed in terms of its deviation from the true value as follows:

$$\hat{g}_i = g_i + \varepsilon_i. \tag{7.2.21}$$

From Eq. (7.2.17), it is clear that to within the measurement error, the solution f_j is not unique. The ambiguity in the solution can be removed by imposing an additional condition that would allow one of the possible sets of f_i to be selected.

Consider now a function that utilizes a least squares method with quadratic constraints in the form

$$\sum_i \varepsilon_i^2 + \gamma \sum_{j=1}^{N} (f_j - \bar{f})^2, \tag{7.2.22}$$

where γ is an arbitrary smoothing coefficient that determines how strongly the solution f_j is constrained to be near the mean $\bar{f}$, i.e., the constraint is given by the variance of f_j. We may select a solution such that the measurement error is minimized while the solution is constrained to be close to the mean $\bar{f}$ such that

$$\frac{\partial}{\partial f_k}\left[\sum_i \left(\sum_{j=1}^{N} A_{ij} f_j - \hat{g}_i \right)^2 + \gamma \sum_{j=1}^{N} (f_j - \bar{f})^2 \right] = 0. \tag{7.2.23}$$

This leads to

$$\sum_i \left(\sum_{j=1}^{N} A_{ij} f_j - \hat{g}_i \right) A_{ik} + \gamma(f_k - \bar{f}) = 0. \tag{7.2.24}$$

In matrix form, we have

$$\mathbf{A}^T\mathbf{A}\mathbf{f} - \mathbf{A}^T\hat{\mathbf{g}} + \gamma\mathbf{H}\mathbf{f} = 0, \tag{7.2.25}$$

where $\mathbf{H}$ is an $(N \times N)$ matrix given by

$$\mathbf{H} = \begin{bmatrix} 1 - N^{-1} & -N^{-1} & \cdots & -N^{-1} \\ -N^{-1} & 1 - N^{-1} & \cdots & -N^{-1} \\ \vdots & \vdots & & \vdots \\ -N^{-1} & -N^{-1} & \cdots & 1 - N^{-1} \end{bmatrix}. \tag{7.2.26}$$

Note that $\bar{f} = N^{-1} \sum_{k=1}^{N} f_k$. The solution is given by

$$\mathbf{f} = (\mathbf{A}^{\mathrm{T}}\mathbf{A} + \gamma\mathbf{H})^{-1}\mathbf{A}^{\mathrm{T}}\hat{\mathbf{g}}. \tag{7.2.27}$$

This is the equation for constrained linear inversion derived by Phillips (1962) and Twomey (1963). The quadrature constraint for smoothing can also be imposed on the first differences, i.e., $\sum(f_{j-1} - f_j)^2$, or the second differences, i.e., $\sum(f_{j-1} - 2f_j + f_{j+1})^2$, and so on (Exercise 7.3). In Exercise 7.4, interested readers may wish to carry out a numerical exercise for the retrieval of aerosol size distribution based on the direct inversion technique.

   If there is a considerable amount of background data available from direct methods, it can be advantageous to construct an appropriate set of base functions to approximate the unknown function f. Let the mean of all past data be $\bar{\mathbf{f}}$. Then we may find a constrained solution that would minimize the mean square departure from this mean. From Eq. (7.2.25), we can write

$$\mathbf{A}^{\mathrm{T}}\mathbf{A}\mathbf{f} - \mathbf{A}^{\mathrm{T}}\hat{\mathbf{g}} + \gamma(\mathbf{f} - \bar{\mathbf{f}}) = \mathbf{0}. \tag{7.2.28}$$

The solution is then

$$\mathbf{f} = (\mathbf{A}^{\mathrm{T}}\mathbf{A} + \gamma\mathbf{1})^{-1}(\mathbf{A}^{\mathrm{T}}\hat{\mathbf{g}} + \gamma\bar{\mathbf{f}}), \tag{7.2.29}$$

where $\mathbf{1}$ is an $(N \times N)$ identity matrix. This inversion will yield an improved measure of the solution if there is a reasonable basis for selecting $\bar{\mathbf{f}}$.

7.2.2   Determination of Total Ozone Concentration

A classic example of utilizing measured transmitted sunlight as a means of inferring composition information is the method proposed by Dobson (1957) for the estimate of total ozone concentration from a ground-based instrument. Basically, this method uses the Beer–Bouguer–Lambert law defined by Eq. (7.2.1) for the transfer of UV radiation to retrieve ozone concentration.

   For application to ozone retrieval, it is convenient to rewrite Eqs. (7.2.1) and (7.2.2) in the form

$$\hat{I}(\lambda) = I_{\odot}(\lambda) \exp\left[- \sum_i \tau_i(\lambda)m_i(\theta_0) \right], \tag{7.2.30}$$

so that

$$\log_{10} \frac{\hat{I}(\lambda)}{I_{\odot}(\lambda)} = -[\tau_3^*(\lambda) \sec Z + \tau_A^*(\lambda)m(\theta_0) + \tau_R^*(\lambda)m(\theta_0)], \tag{7.2.31}$$

where all the values with * should be multiplied by $\log_{10} e$. The solar zenith angle Z is in reference to the height of about 20 km corresponding to the maximum ozone concentration. The factor $(r_0/r)^2$ can be removed by a subtraction operation described later. Further, we define the total ozone concentration in the vertical column as

$$\Omega = \int_0^{z_\infty} \rho_3(z)\, dz.$$

Let the absorption coefficient be denoted by $k(\lambda)$. We may select a pair of wavelengths (λ_1, λ_2) in the Hartley–Huggins ozone absorption bands described in Section 3.2 such that $k(\lambda_1) > k(\lambda_2)$. Thus,

$$\log_{10} \frac{\hat{I}(\lambda_i)}{I_\odot(\lambda_i)} = -k^*(\lambda_i)\Omega \sec Z - \tau_A^*(\lambda_i)m - \tau_R^*(\lambda_i)m, \qquad i = 1, 2. \quad (7.2.32)$$

Subtraction and rearrangement operations lead to

$$N = \log_{10} \frac{\hat{I}(\lambda_1)}{\hat{I}(\lambda_2)} - \log_{10} \frac{I_\odot(\lambda_1)}{I_\odot(\lambda_2)} = -\Omega \sec Z \Delta k - m \Delta \tau_A - m \Delta \tau_R, \quad (7.2.33)$$

where $\Delta k = k^*(\lambda_1) - k^*(\lambda_2)$ and $\Delta \tau_{A,R} = \tau_{A,R}^*(\lambda_1) - \tau_{A,R}^*(\lambda_2)$. Two pairs of wavelengths have been selected to minimize the aerosol effect because $\Delta \tau_A$ is the most uncertain term due to aerosol scattering. In the standard procedure developed by the World Meteorological Organization (WMO), these pairs are (0.3055, 0.3254 μm) and (0.3176, 0.3398 μm). An instrument using these pairs is referred to as a *Dobson spectrometer* (Dobson, 1957). Applying these two pairs to Eq. (7.2.33), we have

$$\Omega = \frac{N^{(1)} - N^{(2)}}{a \sec Z} - b, \qquad (7.2.34a)$$

where the parameterized coefficients a and b are determined from known ozone absorption coefficients and the Rayleigh scattering theory in the forms

$$a = \Delta k^{(2)} - \Delta k^{(1)} \cong 1.388\,(\text{atm}^{-1}\text{cm}^{-1}),$$
$$b \cong 0.009\, p_s. \qquad (7.2.34b)$$

The superscripts (1) and (2) denote the two pairs of wavelengths and p_s is the surface pressure in units of atmospheres.

Total ozone concentration has traditionally been measured in milli atm-cm, called Dobson units (DU). A DU is a vertical thickness of atmosphere in thousandths of a centimeter that is occupied by O_3 when concentrated into a uniform layer of pure gas at the standard temperature and pressure. The total column ozone concentration normally ranges from 200 to 400 DU.

Total ozone has been measured by the Dobson spectrometer at some 80 ground stations around the world. As discussed in Section 3.2.2, observations by Farman *et al.* (1985) using this instrument first detected the springtime (November of the Northern Hemisphere) lowering of ozone, beginning in about 1976.
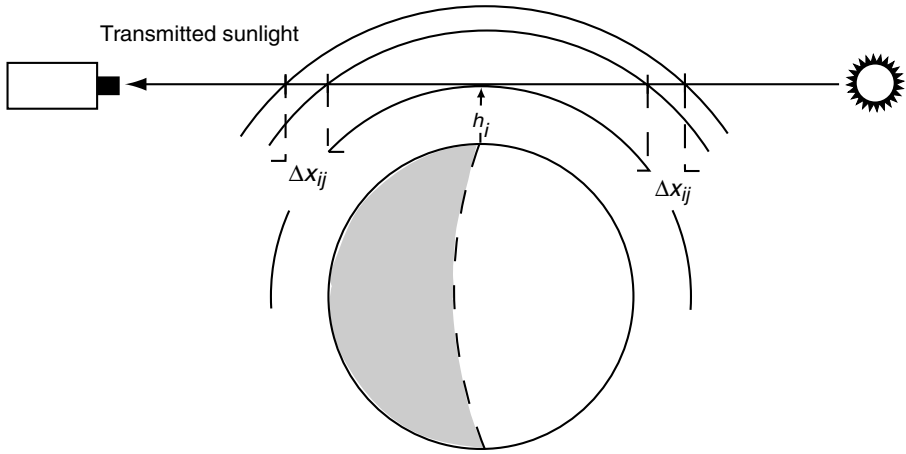
Figure 7.4 The geometry for limb extinction measurements, which are made from the satellite by scanning the sun's disk as the sun rises and sets relative to the motion of the satellite. In the retrieval of the atmospheric gaseous and aerosol profiles, the atmosphere is divided into many layers, in which h_i is the tangent height of the ith layer and Δx_{ij} corresponds to the horizontal distance.

7.2.3 Limb Extinction Technique

Analogous to ground-based sunphotometer measurements of transmitted sunlight, measurements can also be made from space by scanning the sun's disk as the sun rises and sets relative to the motion of the spacecraft, referred to as *solar occultation*. In reference to the geometry depicted in Fig. 7.4, let the intensity measured at the center of the scan be denoted by $I_\odot$, and the intensity determined from a scan at a lower altitude h_i be $I(h_i)$. The transmittance in this case is given by

$$T(\lambda) = I(\lambda, h_i)/I_\odot(\lambda) = \exp[-\tau(\lambda, h_i)], \qquad (7.2.35)$$

where the optical depth along the horizontal tangent path, shown in Fig. 7.4, is defined by the tangent height h_i as follows:

$$\tau(\lambda, h_i) = -\ln\left[\frac{I(\lambda, h_i)}{I_\odot(\lambda)}\right] = \int_{-\infty}^{\infty} \beta_e(\lambda, x)\, dx, \qquad (7.2.36a)$$

where the extinction coefficient is generally contributed by the extinction (scattering and absorption) of aerosols, Rayleigh molecules, O_3, and NO_2, as noted in Eqs. (7.2.2) and (7.2.4), in the form

$$\beta_e(\lambda, x) = \beta_{e,A}(\lambda, x) + \beta_{e,R}(\lambda, x) + \beta_{e,3}(\lambda, x) + \beta_{e,2}(\lambda, x). \qquad (7.2.36b)$$

The basic principle of the solar occultation technique is to take measurements at several wavelengths, similar to the sunphotometer, and at as many altitudes as possible

to obtain the profiles of aerosols and other trace gases. We may divide the atmosphere into an appropriate number of layers (e.g., 80) so that Eq. (7.2.36a) can be expressed in finite difference form such that

$$\tau(\lambda, h_i) = 2 \sum_j \beta_e(\lambda, z_j) \Delta x_{ij}, \qquad (7.2.36c)$$

where Δx_{ij} is the path length in the jth layer represented by z_j associated with the direct solar beam passing through the tangent height h_i. The geometrical factor Δx_{ij} can be devised as the weighting function for inverting the extinction coefficient profile from the optical depth measurements [see Eq. (7.2.13a)].

The limb extinction technique is specifically useful for the determination of aerosols and other minor gases in the stratosphere. It was explored by the Stratospheric Aerosol Measurement (SAM) experiment aboard the Nimbus 7 satellite in 1978. Subsequently, the Stratospheric Aerosol and Gas Experiment I (SAGE I) and SAGE II were conducted in 1979 and 1984, respectively. SAGE II contains seven channels centered at 0.385, 0.448, 0.453, 0.525, 0.6, 0.94, and 1.02 μm. The 0.94 and 0.6 μm channels were used to infer the water vapor and ozone amounts, while the difference between 0.448 and 0.453 μm was used to determine the NO_2 concentration. In this manner, aerosol extinction coefficient profiles can be derived from the seven measurements, following the constrained linear inversion method introduced in Subsection 7.2.1.2. Pioneering work in the solar occultation technique for stratospheric aerosol studies has been reported by McCormick *et al.* (1979).

The solar occultation technique is extremely sensitive to the presence of high-level clouds. As a by-product, the data from SAGE have been used to derive the frequency of occurrence of cirrus clouds based on the extinction values measured (Woodbury and McCormick, 1986). The cirrus results derived from SAGE have complemented those from other satellite remote sensing methods, particularly in view of the fact that it is difficult to determine thin cirrus with optical depths less than about 0.5 based on reflected sunlight and/or emitted infrared radiation from nadir-looking radiometers (see Sections 7.3.5 and 7.4.5 for discussions of the remote sensing of clouds).

7.3 Remote Sensing Using Reflected Sunlight

7.3.1 Satellite–Sun Geometry and Theoretical Foundation

In reference to Fig. 6.1, the sunlight (denoted as In) reflected from a position-vector on the earth and the atmosphere is detected by a satellite (denoted as Out). The position of the sun is defined by the solar zenith angle θ_0, while the satellite position is defined by the emergent zenith angle θ. The relative positions of the sun and the satellite are given by the azimuthal angle difference $\Delta\phi$. From spherical geometry (Appendix C and Fig. 6.1), the angle between the incoming and outgoing light

beams counterclockwise from the incoming beam, known as the scattering angle Θ, is defined by

$$\cos \Theta = \cos \theta \cos \theta_0 + \sin \theta \sin \theta_0 \cos \Delta\phi$$

$$= \mu\mu_0 + (1 - \mu^2)^{1/2}(1 - \mu_0^2)^{1/2} \cos \Delta\phi, \qquad (7.3.1)$$

where we set $\mu = \cos \theta$ and $\mu_0 = \cos \theta_0$.

Any radiometer on board a satellite will have a finite field-of-view on a horizontal plane that collects radiation from the earth and the atmosphere, referred to as *resolution,* which is dependent on the specific instrument designed and its scan angle. The orbit of a satellite is determined by the earth's gravitational attraction force and the centrifugal acceleration of the satellite and is governed by Kepler's laws discussed in Section 2.2. Nearly all the present meteorological satellites are in one of two orbits: sunsynchronous or geostationary.

The earth makes one complete resolution about the sun (2π radian) in one tropical year (365.2422 days). Thus, the right ascension of the sun changes at an average rate of about $1°\text{day}^{-1}$. If the inclination of the satellite is correctly chosen, the right ascension of its ascending node can be made to precess at the same rate. An orbit that is synchronized with the sun is called a *sunsynchronous orbit* or *polar orbit*. The point at which a satellite crosses the earth's equatorial plane from south to north is known as the ascending node; the point passed as it crosses the plane from north to south is known as the descending node. The point directly beneath the satellite is called the subsatellite point or nadir. For a satellite with a height of about 870 km, its inclination angle needs to be about $99°$ for its orbit to be sunsynchronous. This is the nominal height of the National Oceanic and Atmospheric Administration (NOAA) polar-orbiting weather satellites, which orbit the earth in a period of about 100 minutes and cross the equator at the same local standard time (LST) every day, as illustrated in Fig. 7.5a. Morning satellites ascend (or descend) between 06 and 12 h LST and descend (or ascend) between 18 and 24 h LST. Afternoon satellites ascend (or descend) between 12 and 18 h LST, and descend (or ascend) between 00 and 06 h LST.

The space–time coverage of a polar orbiting satellite depends on its orbit and the scanning geometry of its instruments. The poles or near poles are observed on every orbit and the instruments view every point on the earth at least twice per day. Most meteorological satellite instruments are designed such that the area viewed on one orbit touches or overlaps the area viewed on previous and successive orbits. The data is produced in the form of scan lines, each divided into elements or samples known as *pixels* or *scan spots*. Each pixel has a unique time associated with it and is defined by its latitude and longitude. The size of a pixel is controlled by the field-of-view of the instrument and its scan pattern.

If a satellite is moved farther from the earth, it would experience a weaker gravitational field and the centrifugal acceleration required to keep the satellite in orbit would be smaller. The rotation period of the satellite would also become longer. It is possible to select a distance at which the rotation period is exactly equal to the 1 day

(a) Polar

N

870 km

Equator

Orbit Path

S

(b) Geostationary

N

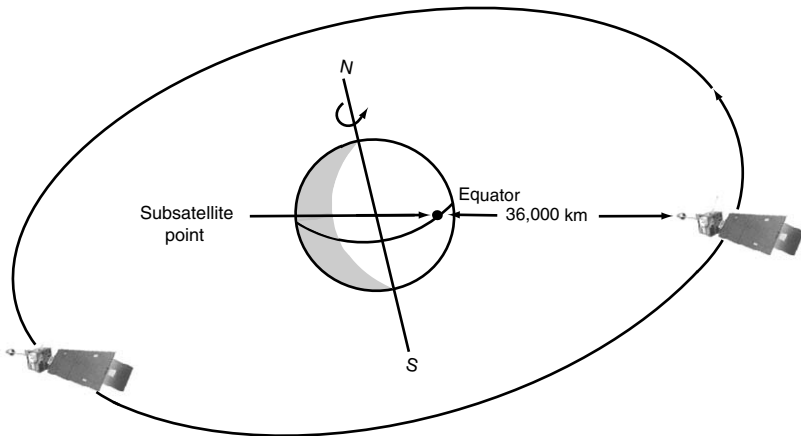Subsatellite
point

Equator
36,000 km

S
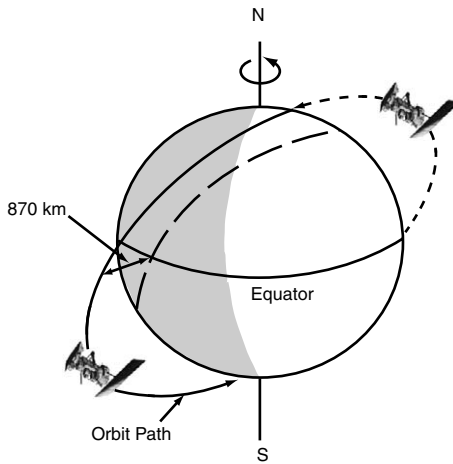
Figure 7.5   (a) Polar and (b) geostationary orbits for NOAA satellites. The polar orbit rotates $1°$ per day to make it synchronous with the sun. The geostationary satellite stays continuously above one spot on Earth.

rotation period of the earth in such a manner that the satellite moves in a counterclockwise fashion. This orbit is called a *geosynchronous* or *geostationary orbit*. To achieve this distance, the satellite must be about 36,000 km above the earth's surface (see Exercise 2.4). Geostationary satellites remain essentially stationary above a point on the equator and are classified by the longitude of their subsatellite points (Fig. 7.5b). They view a fixed area comprising about 42% of the globe at the same time so that

any point in this area can be observed as frequently as their instruments will allow. However, because each point has a fixed geometric relationship to the satellite, it is viewed at only one set of zenith and azimuthal angles. Presently, five geostationary satellites orbit the earth to gather weather data, including two operated by the United States, one by the European Space Agency (METEOSAT), one by Japan (GMS), and one by India (INSAT). The current U.S. system consists of two Geostationary Operational Environmental Satellites (GOES).

In Section 1.4.4, we introduced the basic equation of radiative transfer for plane-parallel atmospheres. In conjunction with satellite applications, we shall rewrite this equation for diffuse intensity as

$$\mu \frac{dI(\tau; \mu, \phi)}{d\tau} = I(\tau; \mu, \phi) - J(\tau; \mu, \phi), \tag{7.3.2a}$$

where the source function, representing the scattering contributions by the direct solar beam and by multiple scattering of the diffuse beam, is given by (Section 6.1)

$$J(\tau; \mu, \phi) = \frac{\tilde{\omega}}{4\pi} \int_0^{2\pi} \int_{-1}^1 I(\tau; \mu', \phi') P(\mu, \phi; \mu', \phi') \, d\mu' d\phi'$$

$$+ \frac{\tilde{\omega}}{4\pi} F_\odot P(\mu, \phi; -\mu_0, \phi_0) e^{-\tau/\mu_0}, \tag{7.3.2b}$$

where P is the phase function, which represents the angular distribution of scattered energy as a function of direction and is an important parameter associated with satellite remote sensing of aerosols and clouds, $F_\odot$ is the direct solar irradiance at the top of the atmosphere (TOA), and the single-scattering albedo $\tilde{\omega}$ is defined as the ratio of the scattering cross section σ_s to the extinction cross section σ_e. The phase function, single-scattering albedo, and extinction cross section are the three fundamental parameters in radiative transfer.

To seek a solution for Eq. (7.3.2a), we shall separate the atmosphere and the surface and assume that there are no diffuse intensities from the top and bottom of the atmosphere. Under this condition, the reflected intensity at TOA can be expressed in terms of the integral equation as follows:

$$I(0; \mu, \phi) = \int_0^\tau J(\tau'; \mu, \phi) e^{-\tau'/\mu} \frac{d\tau'}{\mu}. \tag{7.3.3}$$

Moreover, we may seek a solution by using the single-scattering approximation to obtain the nondimensional bidirectional reflectance introduced in Section 3.4.2 or *bidirectional reflection distribution function* (BRDF) defined by

$$R(\mu, \phi; \mu_0, \phi_0) = \frac{\pi I(0; \mu, \phi)}{\mu_0 F_\odot}$$

$$= \frac{\tilde{\omega}}{4(\mu + \mu_0)} P(\mu, \phi; -\mu_0, \phi_0) \left\{ 1 - \exp\left[-\tau \left(\frac{1}{\mu} + \frac{1}{\mu_0} \right) \right] \right\}.$$

$$\tag{7.3.4a}$$

If we consider an atmosphere such that its optical depth is extremely small, then Eq. (7.3.4a) can be further simplified in the form

$$R(\mu, \phi; \mu_0, \phi_0) = \frac{\tilde{\omega}\tau}{4\mu\mu_0} P(\mu, \phi; -\mu_0, \phi_0). \tag{7.3.4b}$$

Under the optically thin and single-scattering approximations, it is clear that the BRDF at TOA is directly proportional to the phase function and optical depth.

Consider now an underlying surface and account for multiple reflections between the atmosphere and the surface. For simplicity of presentation, let the surface be Lambertian with an albedo r_s (isotropic reflection, although it is not required in the formulation). The BRDF for the combined atmosphere and surface system is the summation of all the light beams emergent at TOA, as shown in Fig. 7.6. Thus, we have

$$\begin{aligned} R &= R_a + \tilde{T}_a r_s \tilde{T}_a^* + \tilde{T}_a r_s R_a^* r_s \tilde{T}_a^* + \cdots \\ &= R_a + \tilde{T}_a r_s \tilde{T}_a^* / (1 - R_a^* r_s), \end{aligned} \tag{7.3.5}$$

where R_a denotes the BRDF from the atmosphere only and the second term represents the surface contribution. In this equation, R_a^* is the BRDF of the atmosphere for radiation from below, and for practical purposes, $R_a^* \approx R_a$. The term $\tilde{T}_a(\mu_0)$ is the total transmission function (direct plus diffuse) from the sun to the surface, while $\tilde{T}_a^*(\mu)$ is the total transmission function from the surface to the satellite. These terms
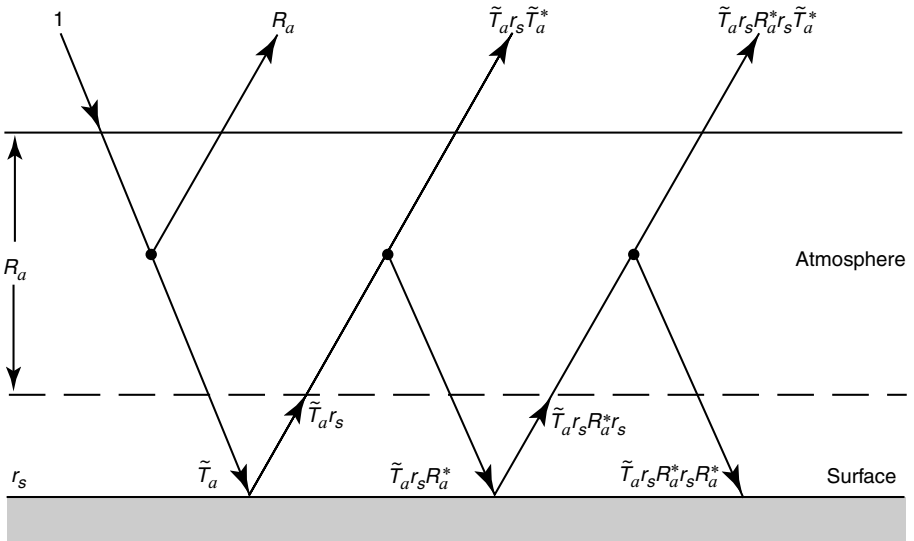

Figure 7.6   Contribution of the bidirectional reflectance from the atmosphere–surface system. The term R_a is the bidirectional reflectance from the atmosphere only, and r_s is the surface albedo, which can be directionally dependent. See also Fig. 6.9.

can be computed from the theory of radiative transfer such as the adding principle introduced in Section 6.4. Within the limits of single-scattering and optically thin approximations, however, we have the diffuse transmission function

$$T_{\text{dif}}(\mu, \phi; \mu_0, \phi_0) = \frac{\tilde{\omega}}{4(\mu - \mu_0)} P(-\mu, \phi; -\mu_0, \phi_0)\left(e^{-\tau/\mu} - e^{-\tau/\mu_0}\right)$$

$$\cong \frac{\tilde{\omega}\tau}{4\mu\mu_0} P(-\mu, \phi; -\mu_0, \phi_0), \quad \mu \neq \mu_0. \qquad (7.3.6)$$

The direct transmission function is simply $T_{\text{dir}} = \exp(-\tau/\mu_0)$. Equation (7.3.5) serves as the fundamental radiative transfer equation for the determination of aerosols and ozone in the atmosphere on the one hand, and for the inference of surface properties on the other.

7.3.2   Satellite Remote Sensing of Ozone

The basic principle involved in the estimation of ozone concentration utilizing reflected sunlight is to select a pair of wavelengths in the Hartley–Huggins ozone absorption band. The selection process is similar to that for the Dobson ozone spectrometer described in Section 7.2.2. Wavelengths near the long-wavelength end of the band at which absorption is relatively weak are chosen so that most of the photons reaching the satellite instrument have passed through the ozone layer and backscattered from within the troposphere. The two wavelengths are separated by about 200 Å so that the scattering effect is about the same at each wavelength, while absorption for one of these wavelengths is stronger than the other. A pair such as (3125, 3312 Å), for example, has been selected in the Nimbus 4 satellite experiment.

The backscattering radiance in the ozone band at the point of a satellite with a nadir-looking instrument depends on the attenuation of the direct solar flux through the ozone layer, the reflecting power of the atmosphere and the associated surface, and the attenuation of the diffusely reflected photons to the point of the satellite. If Z denotes the solar zenith angle at the level of maximum ozone concentration (about 20 km) at the subsatellite point, then the total attenuation path of the backscattered photons through the ozone layer is proportional to $1 + \sec Z$. Let $F_\odot$ and I be the incident solar irradiance and the measured backscattered intensity at TOA, respectively. Following the procedure described in Eq. (7.2.33), we then define

$$\hat{N}(\lambda_1, \lambda_2) = \log_{10} \frac{F_\odot(\lambda_1)}{\hat{I}(\lambda_1)} - \log_{10} \frac{F_\odot(\lambda_2)}{\hat{I}(\lambda_2)}. \qquad (7.3.7)$$

Determination of the total ozone concentration can be made by comparing the observed $\hat{N}$ with values precomputed for a series of different standard ozone profiles by means of the searching method.

The computational method for the transfer of solar radiation in a scattering and absorbing atmosphere for ozone studies usually follows Eq. (7.3.5). Writing this

equation in terms of scattered intensity we have

$$\hat{I}(\Omega, \mu_0, r_s) = I(\Omega, \mu_0, 0) + \frac{r_s T(\Omega, \mu_0)}{1 - r_s \bar{r}(\Omega)}, \qquad (7.3.8)$$

where $T(\Omega, \mu_0) = \mu_0 F_\odot \widetilde{T}_a(\mu = 1) \widetilde{T}_a(\mu_0)/\pi$, $\mu_0 = \cos Z$, $\bar{r}$ is a mean atmospheric reflection, and Ω denotes the total ozone concentration. The first term is the atmospheric contribution alone, while the second is produced by interaction with the underlying surface. In this equation, all the relevant parameters in the radiative terms are included in parentheses. Note that since the ozone instrument is normally looking in the nadir direction, the azimuthal dependence can be neglected.

The three basic procedures for the determination of total ozone concentration from the observed $\hat{N}$ are as follows: (a) A set of tables containing the computed quantities $I(\Omega, \mu_0, 0)$, $T(\Omega, \mu_0)$, and $\bar{r}(\Omega)$ for different values of μ_0 and Ω are prepared *a priori*. (b) The effective surface albedo is determined by utilizing the radiometric measurement at a wavelength outside the ozone absorption band, say $\lambda_3(3800 \text{ Å})$. At this wavelength, the ozone dependence drops out of all the terms in Eq. (7.3.8), and a measurement of $\hat{I}_3(\mu_0, r_s)$ permits the direct calculation of the surface albedo with the formula

$$r_s(\lambda_3) = \frac{\hat{I}_3(\mu_0, r_s) - I_3(\mu_0, 0)}{T(\mu_0) + \bar{r}[\hat{I}_3(\mu_0, r_s) - I_3(\mu_0, 0)]}. \qquad (7.3.9)$$

The assumption is made that r_s is independent of wavelength so that it can be used for the pair of wavelengths (λ_1, λ_2). However, an empirical adjustment may also be performed from known surface albedo measurements. (c) With the surface albedo known, computations are then carried out to generate $N(\lambda_1, \lambda_2)$ versus total ozone concentration Ω. Best estimates of Ω from the observed intensities via $\hat{N}$ can then be made by an optimized search method. The matching and search method has been used by Mateer *et al.* (1971) to estimate total ozone concentration from the Nimbus 4 satellite measurements of backscattered intensities. Dave (1978) further discussed the effect of atmospheric aerosols on the estimate of total ozone concentration.

As a result of environmental concerns and potential health hazards, ozone concentration has been monitored by satellites since the beginning of the sounding era. The Backscatter Ultraviolet Spectrometer (BUV) on board Nimbus 4 operated for seven years, from 1970 to 1977. The Total Ozone Mapping Spectrometer (TOMS) on Nimbus 7 produced daily global maps of total ozone at 50–150 km resolution in 1978. The Solar Backscatter Ultraviolet Radiometer (SBUV) on the NOAA satellites has provided daily ozone data over the globe on a routine basis since 1980.

7.3.3 Satellite Remote Sensing of Aerosols

The retrieval of aerosol optical and microphysical properties from satellite measurements of reflected sunlight is a difficult task because of the relatively small influence of aerosols. Aerosol retrieval is further complicated by the variability of the underlying surfaces. In reference to Section 7.2.1, the basic aerosol parameters include

optical depth, size distribution, and the refractive index, which is wavelength dependent. The last parameter is related to the composition of the aerosol. Given the measured reflected intensities at some appropriate wavelengths that are sensitive to aerosol properties, we wish to determine the pertinent parameters. The simplest situation would be a black surface that makes no contribution to the scattered intensity. In this case, we can use Eq. (7.3.4b) so that the aerosol optical depth is determined by

$$\tau = \frac{\hat{R}(\mu, \phi; \mu_0, \phi_0)}{P(\mu, \phi; \mu_0, \phi_0)} \frac{4\mu\mu_0}{\tilde{\omega}}. \tag{7.3.10}$$

In addition to the measured bidirectional reflectance $\hat{R}$ and the sun–satellite geometry, we also need the information of phase function P and single-scattering albedo $\tilde{\omega}$. Because the aerosol size distribution and the refractive indices are generally unknown *a priori,* P and $\tilde{\omega}$ must be assumed or parameterized from other information. In this manner, a measured $\hat{R}$ will yield an optical depth for the atmosphere. Since the Rayleigh scattering of the atmosphere is known, aerosol optical depth can subsequently be determined. The oceans are close to black in the visible ($\sim$6% albedo on average) and near-infrared wavelengths. Thus, retrieval of aerosol optical depth from satellites has had some success over the oceans. The remote sensing of aerosols over land, however, despite its importance, is a subject still requiring research and development.

Since 1979, the Advanced Very High Resolution Radiometer (AVHRR) aboard NOAA satellites has been used to study aerosols. It consists of five nominal channels centered at 0.63, 0.86, 3.7, 10.9, and 12 μm, with a horizontal resolution of about 1 km $\times$ 1 km. The 0.63 μm channel has been extensively employed to map aerosol optical depth over the oceans. With the addition of the 0.86 μm channel, the size parameter of a Junge distribution can be estimated. The 0.86 μm channel data has also been used to provide an estimate of the combination of $\tilde{\omega}P$ occurring in Eq. (7.3.10).

A number of other instruments have also been designed to study aerosols and clouds from space. Under NASA's earth science programs, specifically the Earth Observing System (EOS) Program, a series of polar-orbiting and low-inclination satellites have been and continue to be in orbit for long-term global observations of the atmosphere, land surface, biosphere, solid earth, and oceans. Two of the EOS instruments are particularly pertinent to the study of aerosols. The Moderate–Resolution Imaging Spectrometer (MODIS) (King *et al.,* 1992) is designed to make 0.25–1 km resolution observations in 36 visible and infrared bands. Many of the visible and near-infrared channels have been used for the mapping of aerosol optical depth and size. The Multi-Angle Imaging SpectroRadiometer (MISR) provides multiangle observations. MISR produces images at nine fixed angles in the along-track direction with one at the nadir, and four both fore and aft out to $\pm$70.5°. Four spectral bands centered at 0.443, 0.555, 0.670, and 0.805 μm are available with ground resolution between about 240 m and 2 km (Diner *et al.,* 1998). This instrument appears to be useful for studying the scattering phase function of spherical and nonspherical aerosols.

7.3.4 Satellite Remote Sensing of Land Surfaces

The land surface of the earth is highly complex involving a combination of vegetations, soils, sand, rocks, water, and ice. A precise determination of the vegetation and surface properties is critical to the present and future management of earth's resources, as well as to the understanding of the role that land surfaces play in the climate system. The remote sensing of vegetation and surface properties by satellites is a subject that is of interest to numerous disciplines, including meteorology, hydrology, geography, geology, biology, ecology, and electrical engineering. Most of the research areas involve the analysis of satellite images and are beyond the scope of this text. However, we shall discuss the fundamentals associated with the determination of surface albedo and present an important application of the AVHRR /NOAA data for the inference of vegetation.

The surface reflectivity or albedo determines the solar flux available at the surface and is the essential parameter in the discussion of climate over land. The surface albedo is dependent on the type of surface. For water surfaces, the albedo ranges from about 6 to 9%, except for cases involving the low solar angle that is associated with the high latitudes of the winter hemisphere. The albedo can range from 10 to 40% for various land surfaces. For example, deserts and sand dunes have albedos of about 30–40%, whereas those for meadows and forests are about 10%. The albedos of snow and ice are greater than 40%. Moreover, the albedos of some vegetation surfaces vary greatly with solar wavelength as noted below.

In reference to Eq. (7.3.5), if we select a wavelength in the visible spectrum (0.4–0.7 μm) such that the product of the surface albedo r_s and the atmospheric BRDF (generally less than 0.1) is much smaller than 1, then we can express the surface albedo in the form

$$r_s \cong a\hat{R} - b, \tag{7.3.11}$$

where $a = 1/\tilde{T}_a\tilde{T}_a^*$ and $b = R_a/\tilde{T}_a\tilde{T}_a^*$. The coefficients a and b are the so-called atmospheric correction terms involving the scattering contributions of aerosols and molecules, which can be empirically determined for specific applications. Thus, a measurement of BRDF $\hat{R}$ at TOA determined by the sun–satellite geometry will provide a surface albedo value. A surface albedo so determined is averaged over the pixels of the satellite instrument and is normally assumed to be independent of the incoming and outgoing directions. In reality, the surface reflection function can be extremely complex, especially over vegetation areas.

An important characteristic of the reflection by vegetation surfaces is the sharp transition in the reflection at a wavelength of about 0.7 μm. The presence of chlorophyll in vegetation leads to strong absorption at wavelengths shorter than 0.7 μm. Figure 7.7 shows the reflectance as a function of wavelength for dry and wet bare soil and vegetation cover (Li *et al.*, 2002). In view of these spectral properties, we may select two AVHRR wavelengths ($\lambda_1 = 0.63$ μm and $\lambda_2 = 0.86$ μm) and define a term called the normalized difference vegetation index (NDVI), in the form

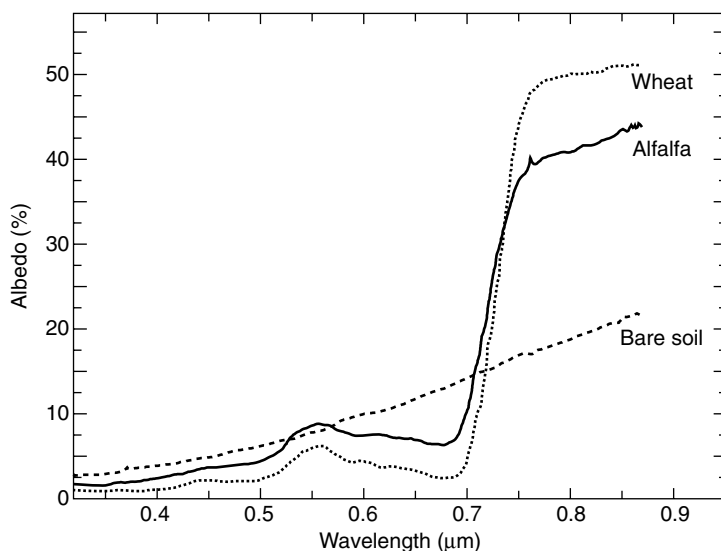$$\text{NDVI} = \frac{I(\lambda_2) - I(\lambda_1)}{I(\lambda_2) + I(\lambda_1)}. \tag{7.3.12}$$

Figure 7.7   Illustration of the step function transition in the surface spectral albedo of two types of vegetation at 0.7 μm, compared to the continuous spectral albedo for soil surfaces. These results were derived from measurements made in the Southern Great Plains of Oklahoma surrounding the Central Facility of the Department of Energy's Atmospheric Radiation Measurement site (data taken from Li *et al.,* 2002).

It is an index of biospheric activity indicating the amount of live vegetation in the field-of-view of the satellite sensor. The NDVI field has been routinely processed from the NOAA/AVHRR data for research and operational purposes.

7.3.5   Cloud Optical Depth and Particle Size

Clouds cover more than 50% of the planet earth and are the most important regulators of the radiation budget of the earth–atmosphere system. The transfer of radiation through cloud layers depends on particle concentration, size distribution and shape, and cloud thickness and geometry. Information about cloud composition and structure is of vital importance to the understanding of the radiation balance and energetics of the earth–atmosphere system.

Because of the number of variables involved and the associated problem of multiple scattering by particulates, determination of the highly varying cloud variables by remote sensing is a difficult task. With the availability of high-speed computers and efficient numerical methods for the solution of the radiative transfer equation, advanced techniques for the inference of cloud composition using the reflected intensity and polarization of sunlight have been developed. Analogous to the inference of total ozone concentration, the method involved is an ad hoc direct matching between the observed and computed intensity and/or polarization. In this section, we describe the information content of the reflected intensity and polarization of sunlight from water and ice clouds.

7.3.5.1 BIDIRECTIONAL REFLECTANCE

The remote sensing of clouds from space using reflected sunlight requires a fundamental understanding of the radiative properties of water and ice clouds. Determination of these properties must begin with knowledge of the complex refractive index of water and ice as a function of wavelength. The real refractive indices of water exhibit substantial deviations from those of ice at wavelengths greater than about 10 μm. The imaginary refractive index of ice is much more complex, with values ranging from about 10^{-6} at 0.9 μm to about 0.75 at 3 μm. Ice exhibits relatively strong absorption at about 1.6 μm, where water shows a minimum. The imaginary refractive indices for ice and water vary rapidly in the solar and IR spectra. There are significant variations in the absorption properties of ice and water in the near-IR solar spectrum.

In Section 3.2.3, we discussed the absorption bands in the solar spectrum. In the near-IR region, the absorption of solar radiation is primarily due to water vapor. Absorption by water vapor is strong in the band centers and falls off sharply away from these centers. Absorption by ice and water, on the other hand, is more constant across each band, being less intense than water vapor in the band centers and more intense away from the centers. Moreover, the maximum absorption due to ice and water does not coincide exactly with the water-vapor band centers. There are regions in the near-IR where water vapor absorption dominates, whereas in other regions, ice and water absorption is more important. The reflection of sunlight from clouds depends on the optical depth and some measure of the particle size within the cloud. Figure 7.8 illustrates the spectral bidirectional reflectance and absorptance for three mean effective ice crystal sizes [see Eq. (7.3.15a) for definition]. The calculation uses a solar zenith angle of $30°$, an emergent angle of $0°$, an ice water path (IWP) of 1 g m^{-2}, and a spectral interval of 50 cm^{-1} containing 30 cumulative probability functions (g's) covering the spectrum from 0.2 to 5 μm, based on the correlated k-distribution method for infrared radiative transfer introduced in Section 4.3. From the absorption spectrum, the H$_2$O absorption bands located at 3.2, 2.7, 1.87, 1.38, 1.1, 0.94, 0.82, and 0.72 μm are evident, as are the 4.3 μm CO$_2$ and O$_3$ UV bands. The bidirectional reflectances have maxima in between the H$_2$O absorption bands. Small ice crystals reflect more solar radiation. Sufficient ice crystal size information is clearly demonstrated in the near-IR spectrum. The spectral features are similar for clouds containing water droplets.

Variation of the reflectance in the near-IR region could provide a means for the inference of some of the physical properties of clouds. This possibility has been suggested by Hansen and Pollack (1970), who have interpreted spectral near-IR reflectances of clouds measured from aircraft. Suggestions of the inference of the optical depth and mean radius from spectral reflectance measurements have also been made by Twomey and Seton (1980). The preceding suggestions are based on the principle of radiative transfer that the reflection of clouds at a wavelength with little absorption (such as in the visible spectrum) is primarily a function of their optical depth, whereas in a near-IR wavelength at which the absorption of water vapor in the clouds is small, their reflection is largely dependent on particle size.
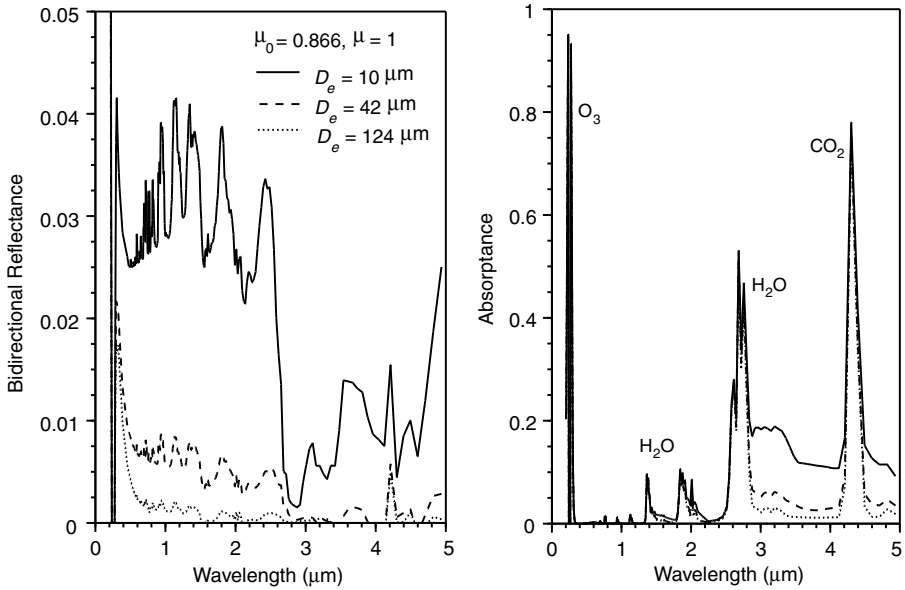
Figure 7.8   Spectral bidirectional reflectance and absorptance as functions of wavelength for cirrus clouds with mean effective ice crystal sizes of 10, 42, and 124 μm . Absorption bands due to ozone, water vapor, and carbon dioxide are identified. The spectral features are similar for water clouds.

Before we present some pertinent radiative transfer calculations and observed data, we must define the particle size that can be inferred from reflected sunlight. A brief review of the droplet size distribution in water clouds, including stratus, nimbostratus, altostratus, and various types of cumulus, has been presented by Liou (1992). A determination of the detailed droplet size spectrum from space, employing currently available instruments, has yet to be developed and verified. Nevertheless, we may define a mean effective size to represent the actual size distribution taking into account the scattering property of spherical droplets such that they scatter an amount of light proportional to their cross sectional area as follows:

$$a_e = \int a \cdot \pi a^2 n(a)\, da \Big/ \int \pi a^2 n(a)\, da. \qquad (7.3.13a)$$

The mean effective radius differs from the simple mean radius in that the droplet cross section is included as a weighting factor. As shown by many radiative transfer calculations, the reflected and transmitted sunlight is primarily dependent on this parameter regardless of the detailed distribution of droplet sizes (Hansen and Travis, 1974). In the following, we wish to relate this mean parameter to the amount of vertically integrated liquid water in the cloud, referred to as the liquid water path (LWP, g cm^{-2}), and optical depth.

From the definition of liquid water content (LWC, g cm^{-3}) for spherical droplets, we have

$$\mathrm{LWC} = \frac{4\pi}{3}\rho_l \int a^3 n(a)\, da, \qquad (7.3.13b)$$

where ρ_l is the density of water. Thus, LWP = LWC $\cdot$ Δz. The optical depth is defined by [see also Eq. (7.2.9b)]

$$\tau = \Delta z \cdot \int Q_e \pi a^2 n(a)\, da, \qquad (7.3.13c)$$

where Q_e is the efficiency factor for extinction, a function of the droplet radius, wavelength, and refractive index. For wavelengths in the visible, $Q_e \cong 2$ for cloud droplets. Thus, combining the preceding three equations, we obtain

$$a_e \cong \frac{3}{2\rho_l}\mathrm{LWP}/\tau, \qquad (7.3.13d)$$

which relates the optical depth, LWP, and droplet size. The relation is significant. Consider two clouds having the same LWP. The cloud that contains a smaller droplet would have a larger optical depth and therefore would reflect more sunlight. Anthropogenic pollution sources can affect droplet size, referred to as the *indirect aerosol effect* (see Exercise 7.5 and Section 8.4.4 for further discussion).

In conjunction with the retrieval of the optical depth and mean effective droplet radius of water clouds from the NASA EOS/Terra satellite using the MODIS instrument discussed in Section 7.3.3, King *et al.* (1997) performed radiative transfer calculations for a wide variety of solar zenith angles and observational zenith and azimuthal angles at a number of selected wavelengths in the visible and near-IR. Shown in Fig. 7.9 are bidirectional reflection function (BRDF or reflectance) correlations at 0.664/1.62 μm and 0.664/2.142 μm. These wavelengths were selected because they are outside the water vapor and oxygen absorption bands and, at the same time, have substantially different water droplet absorption properties. The minimum value of the reflectance at each wavelength corresponds to the underlying ocean reflectance in the absence of an atmosphere. The dashed curves represent the reflectances for specified values of cloud optical depth, whereas the solid lines denote those for specified values of droplet mean effective radius. As evidenced by these results at a nonabsorbing wavelength (0.664 μm), cloud optical depth is largely determined by reflectance with little dependence on droplet radius. The reflectance at 2.142/1.621 μm, in contrast, is largely sensitive to the mean effective radius, with the largest values occurring for small droplet sizes. The data points superimposed on the theoretical curves represent over 400 measurements obtained from the MODIS Airborne Simulator (MAS) instrument, which is a 50-band scanning spectrometer that was mounted in the NASA ER-2 aircraft during an experiment that was carried out over marine stratocumulus clouds in the vicinity of the Azores approximately 1000 km southwest of Lisbon on 22 June, 1992. Simultaneous determination of cloud optical depth and
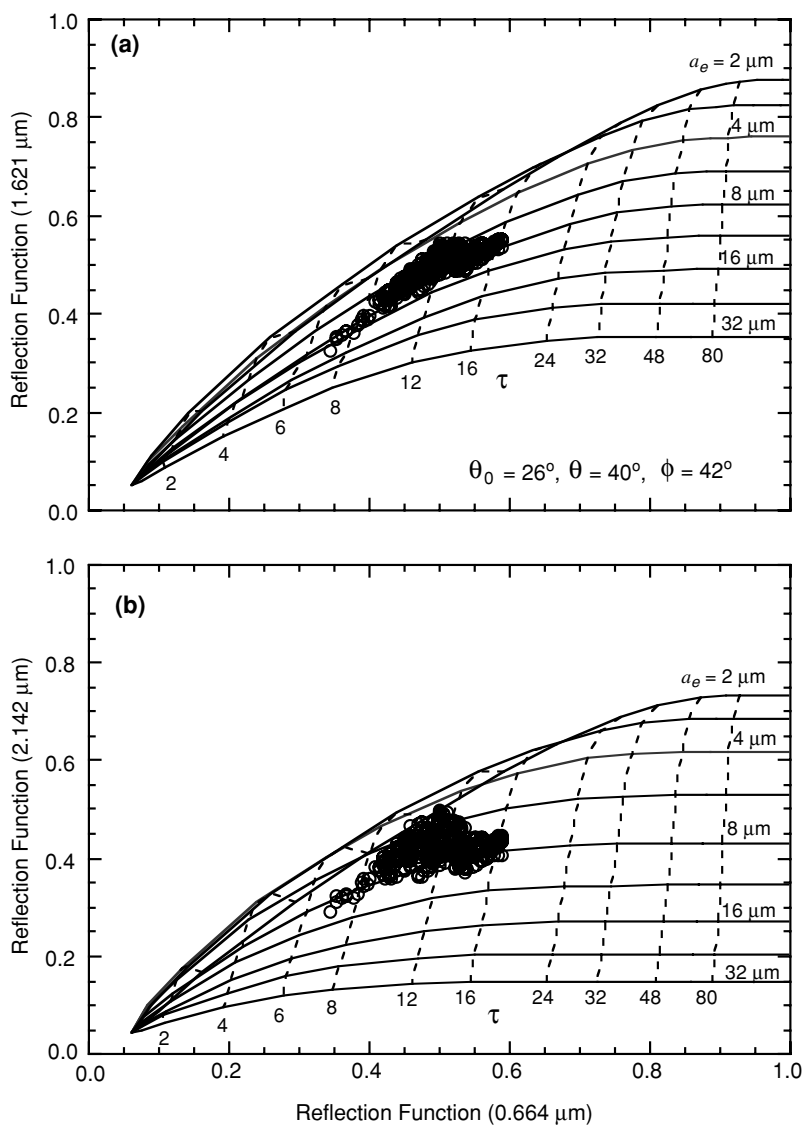
Figure 7.9   Theoretical relationship between the reflectance at 0.664 and (a) 1.621 μm and (b) 2.142 μm for various values of optical depth at 0.664 μm and effective droplet radius, for the specific geometry denoted in the diagram. Data from over 400 measurements obtained with the MAS that was aboard the NASA ER-2 aircraft are superimposed. These observations were obtained when the aircraft flew above marine stratocumulus clouds during a stratus cloud experiment on June 22,1992 (data taken from King *et al.,* 1997).

mean effective droplet radius can be performed by maximizing the probability that the measured reflectances $R_m(\mu_0, \mu, \Delta\phi)$ have the functional form $R_c(\tau, a_e; \mu_0, \mu, \Delta\phi)$, such that

$$\chi^2 = \sum_{i=1}^{3} \left[\ln R_m^i(\mu_0, \mu, \Delta\phi) - \ln R_c^i(\tau, a_e; \mu_0, \mu, \Delta\phi) \right]^2, \qquad (7.3.14)$$

where the summation extends over the three wavelengths. Validation of this retrieval algorithm is critical because of the nonuniqueness of the solutions determined from the statistical optimization method, and is a subject of continuing research.

Analogous to the retrieval of water cloud optical depth and effective radius, one can also apply the reflectance correlation technique to clouds containing ice crystals (Rolland and Liou, 1998; Ou *et al.,* 1999). Ice crystals are much more complicated than spherical water droplets with respect to their scattering and radiative properties, as presented in Sections 5.4 and 6.7.1. We have defined the mean effective ice crystal size in Eq. (5.1.1) to represent the ice crystal size distribution, and it is duplicated here for the continuity of the present discussion on remote sensing:

$$D_e = \int V n(L)\, dL \Big/ \int A\, n(L)\, dL, \qquad (7.3.15a)$$

where L is the maximum dimension of an ice crystal, V is the volume, A is the geometric projected area of an ice crystal on a surface perpendicular to the incident light beam, and $n(L)$ is the ice-crystal size distribution. In this manner, the shape of irregular ice crystals is accounted for. Further, the ice water content (IWC) for a given ice crystal size distribution is defined by

$$\text{IWC} = \int V \rho_i n(L)\, dL, \qquad (7.3.15b)$$

where ρ_i is the density of ice. The volume of a hexagonal ice crystal is given by $3\sqrt{3}LD^2/8$, with D the ice crystal width. Moreover, for randomly oriented ice crystals in the limits of geometric optics, the extinction cross section is $3D(\sqrt{3}D/4 + L)/2$ (Takano and Liou, 1989a). With these relationships and following the principle introduced for water droplets, we may also relate visible optical depth and mean effective ice crystal size as follows:

$$\tau \cong \text{IWP}(c + b/D_e), \qquad (7.3.15c)$$

where $\text{IWP} = \text{IWC} \cdot \Delta z$ denotes ice water path, and $c \cong -6.656 \times 10^{-3}$ and $b \cong 3.686$ for ice columns. Below we present the inference of the optical depth and ice crystal mean effective size based on reflected solar radiation.

Radiative transfer calculations using the MAS channels of 0.681, 1.617, and 2.139 μm were performed for the six ice-crystal size distributions with mean effective ice-crystal size ranging from 24 to 124 μm, and for two water-droplet size distributions with mean effective radii of 4 and 8 μm (Fig. 7.10). The results are displayed in two-dimensional reflectance diagrams in terms of 0.681–1.617 μm and

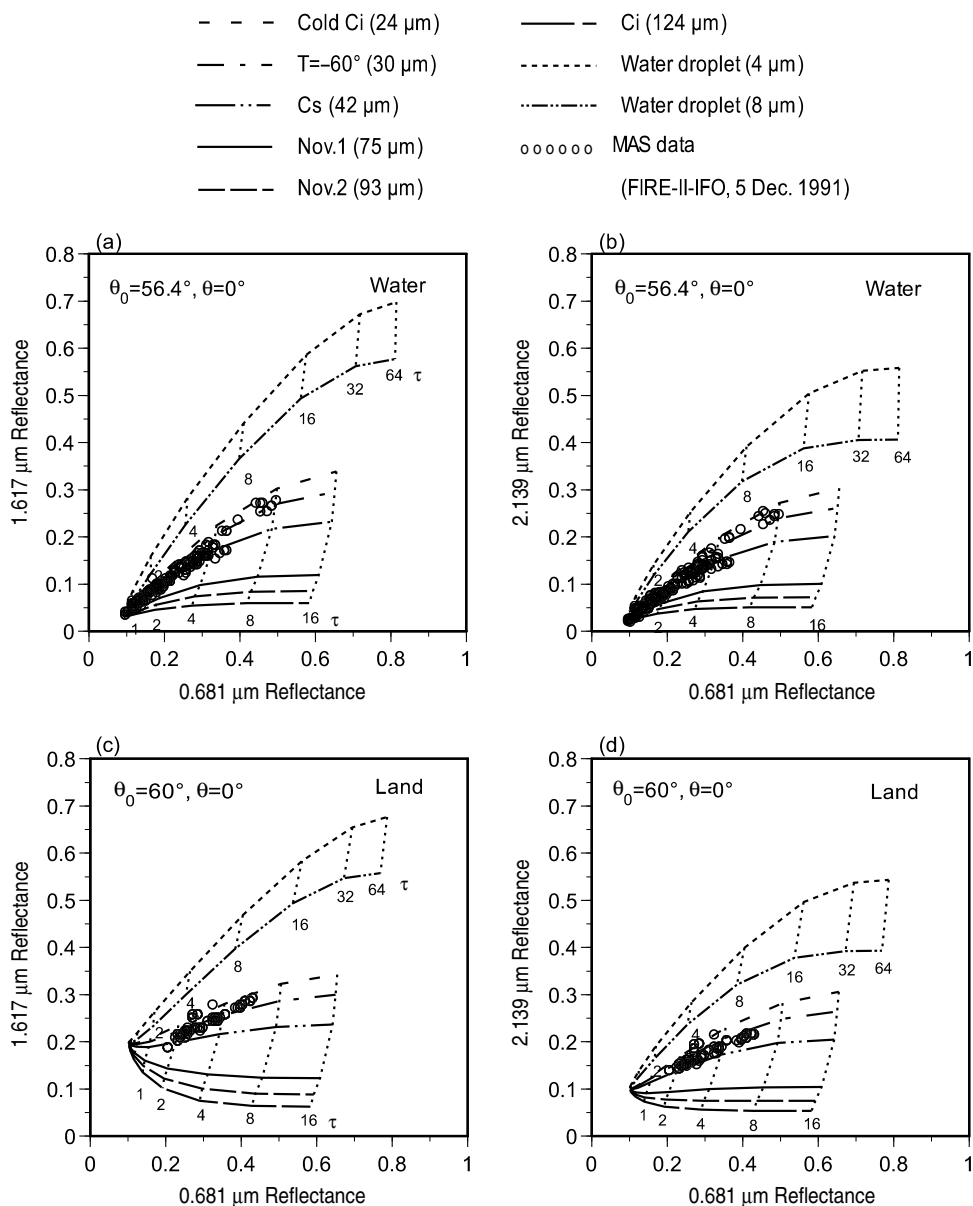|	
$-\ -\ -$ Cold Ci (24 μm)	$-----$ Ci (124 μm)
$-\ \cdot\ -$ T=–60° (30 μm)	$\cdots\cdots$ Water droplet (4 μm)
$-\cdot\cdot-$ Cs (42 μm)	$\cdot-\cdot-\cdot$ Water droplet (8 μm)
$———$ Nov.1 (75 μm)	o o o o o o MAS data
$-\ —\ -$ Nov.2 (93 μm)	(FIRE-II-IFO, 5 Dec. 1991)

Figure 7.10   Correlation between the reflectances at 0.681/1.617 μm and at 0.681/2.139 μm. Radiative transfer calculations were performed for the six ice-crystal size distributions with mean effective sizes ranging from 24 to 124 μm, and for two water clouds with mean effective radii of 4 and 8 μm. The optical depth ranges from 0.5 to 64. Overlapped with the curves are the MAS data obtained from FIRE-II-IFO on 5 December 1991, over the northern Gulf of Mexico and eastern Oklahoma. Frames (a) and (b) are cases over water, and frames (c) and (d) are cases over land.

0.681–2.139 μm for optical depths ranging from 0.5 to 64. For both cirrus and water clouds, the 0.681 μm reflectance mainly depends on the optical depth, whereas the 1.617 and 2.139 μm reflectances are primarily functions of the mean effective particle size. A clear distinction is seen between the correlations for water clouds (mean effective radius < 8 μm) and for cirrus clouds (mean effective size >20 μm). It is possible that the correlations for larger water-droplet mean effective radius and smaller ice-crystal mean effective size may overlap. However, based on the statistics of aircraft observations compiled by Liou (1992), the mean droplet radius for various water clouds is within the 3.5–5.0 μm range and the spectrum of ice-crystal size distribution is generally between 20 and 2000 μm. Thus, it is expected that the probability of occurrence of the correlation overlap for water and ice clouds is very small. Even if the water droplets and ice crystals are about the same size, they can be distinguished by inferring the cloud phase and cloud temperature from separate means.

Also shown in Fig. 7.10 are the MAS data obtained from FIRE-II-IFO on 5 December 1991. The top and bottom diagrams correspond to the cases over water and land surfaces, respectively. The case over water was taken at 1636 UTC, 5 December 1991, when the ER-2 aircraft was flying over the northern part of the Gulf of Mexico near the southern coastal region of Louisiana. The case over land was taken at 1923 UTC on the same date, when ER-2 was flying over eastern Oklahoma. In the calculations, the effective surface albedos used were determined from the MAS reflectances over clear pixels. The data points indicate that the detected cirrus clouds appear to contain small ice particles with optical depths less than about 6. Larger optical depths indicate the possibility of cirrus overlying low clouds. For each data point, an optical depth and a mean effective ice-crystal size can be determined based on Eq. (7.3.14).

7.3.5.2   POLARIZATION

In Sections 5.3 and 5.4, we presented the single-scattering characteristics of spherical droplets and various types of ice crystals. Polarization of the sunlight reflected from clouds appears to show a strong imprint of the cloud thermodynamic phase (spherical water droplets and nonspherical ice crystals) as well as ice crystal shape.

Perhaps the most intriguing results in connection with the use of polarization data for the determination of particle size and optical characteristics have been found in the study of the cloud deck of Venus. Although Venus is the nearest planet, it is the most mysterious as it is surrounded by a veil of clouds. Polarization observations of Venus have been made by the French astronomer Lyot (1929) using visible light. Hansen and Hovenier (1974) have performed an extensive investigation of the particle shape, size, and refractive index of the Venus cloud deck by comparing the observed linear polarization with comprehensive multiple scattering computations, including Lorenz–Mie particles and Rayleigh molecules. Shown in Fig. 7.11 are observations and theoretical computations of the linear polarization of visible sunlight reflected by Venus. After varying the size parameter and refractive index, the best fit to the observed data is given by the dashed-dot curve. The maximum at the phase angle
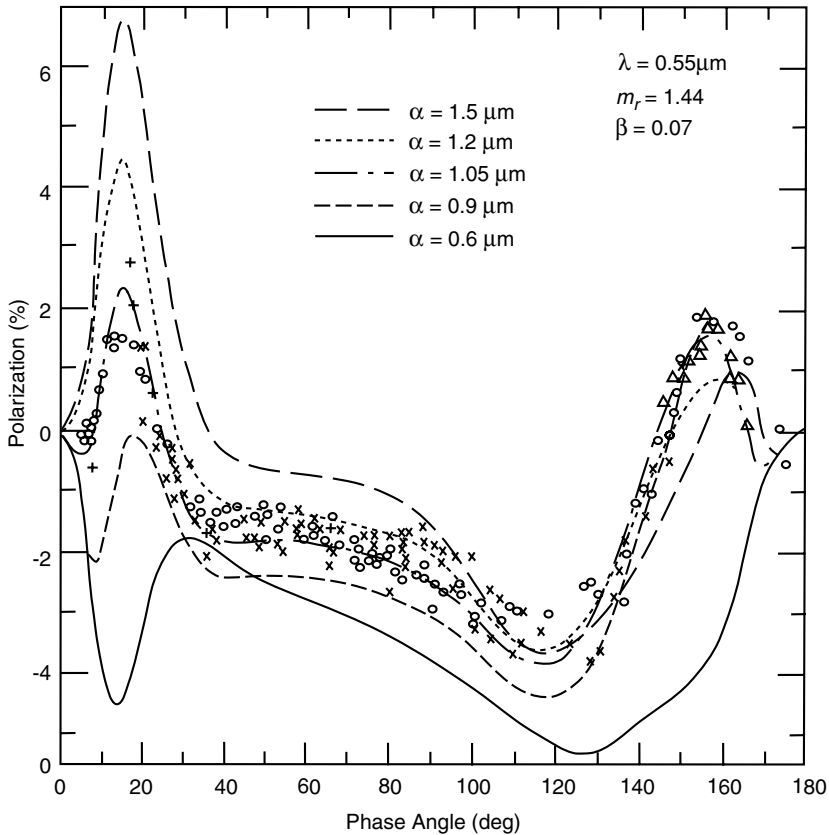
Figure 7.11   Observations ($\circ$, $\times$, $+$, Δ) of the polarization of sunlight reflected by Venus as a function of the phase angle ($180° - \Theta$) in the visual wavelength region and theoretical computations for $\lambda = 0.55\,\mu$m. α denotes the mean radius, β is an effective dispersion of the size distribution, and m_r is the refractive index (after Hansen and Hovenier, 1974).

of about $20°$ (scattering angle $160°$) is the primary rainbow, the product of light rays undergoing one internal reflection, which nonspherical particles do not show, as illustrated in Sections 5.3 and 5.4. Based on this study, it was concluded that the Venus cloud layer was composed of spherical particles having a mean radius of about $1.05\,\mu$m and an effective dispersion of 0.07. The refractive index of the particles is about 1.44 at a wavelength of $0.55\,\mu$m with a normal dispersion.

Photometric interpretations may also be carried out to understand the physical, optical, and chemical properties of clouds and/or hazes of other planets. Mariner spacecraft studies of Mars reveal that clouds of H_2O ice as well as possible CO_2 ice haze are present in the Martian atmosphere. Photometric and scattering techniques can provide significant data for understanding the physical and chemical composition of NH_3 clouds in the Jovian atmosphere and the nature of Saturn's rings. Particles that

occur in Mars, Jupiter, and Saturn are likely to be nonspherical. As a consequence of their nonsphericity and the associated orientation problems, reliable single-scattering information must be developed to allow multiple scattering calculations for the purposes of interpretation of observed data.

Further, Takano and Liou (1989b) and Liou and Takano (1994) have used the single-scattering results for hexagonal plates and columns, and later a combination of regular and irregular ice particles, as shown in the upper panel of Fig. 7.12, to interpret the measured linear polarization pattern of sunlight reflected from optically thick cirrus clouds presented by Coffeen (1979). More recently, polarization of sunlight reflected from cirrus clouds has been reported by Chepfer *et al.* (1998) during the European Cloud Radiation Experiment 1994 campaign based on airborne polarimeter measurements from the Polarization and Directionality of the Earth's Reflectances (POLDER) instrument. Two channels in this instrument at 0.443 and 0.864 μm were used for polarization measurements. The lower panel of Fig. 7.12 shows the observed polarization defined by $PO = (Q^2 + U^2 + V^2)^{1/2}$ for two cirrus cloud episodes. In the left and right diagrams, the scattering angle ranges are $75°$ to $165°$ and $90°$ to $180°$, respectively, with the respective solar zenith angles depicted in the diagrams. After extensive trial- and-error analyses, we find that the results employing an optical depth of about 3 match the observed data in the left diagram most closely. Radiative transfer calculations are subsequently performed using randomly oriented hollow columns, plates, and irregular ice particles. The plate case ($L/2a = 8/80 \mu$m) appears to fit the observations in all scattering angle ranges, as displayed in the left diagram, except in the backscattering range in which the irregular ice particle case fits better. The polarization data presented in the right lower panel illustrates a peak at about $104°$ (subsun feature) associated with the horizontal orientation of ice plates and columns. To provide adequate interpretation, all 16 phase matrix elements are needed in radiative transfer calculations. Following the approach presented in Section 6.7.1 for polarized radiative transfer in horizontally oriented ice particles, 0.1% of hollow Parry columns (horizontal random orientation in a fixed direction) was added to a combination of 60% rough-surface ice particles, 30% hollow columns, and 10% plates randomly oriented in three-dimensional space to provide the best interpretation of the observed data.

7.3.5.3   REFLECTED LINE SPECTRUM

The signature of high-level cirrus appears in the bidirectional reflectance associated with a number of water-vapor absorption bands, as shown in Fig. 7.8, particularly those containing small ice crystals. Among these, the 1.38 μm band appears to be most useful for the detection of thin cirrus, because of the combination of the moderate strength of this absorption band and the amount of solar energy residing within the band (Gao and Kaufman, 1995). The spectral lines of sunlight reflected from other planets have been observed and utilized to determine the composition of planetary atmospheres (Goody and Yung, 1989). Such observations have not been made from satellites for the earth, however. Based on the computational results from a line-by-line equivalent radiative transfer program, we study the information content of
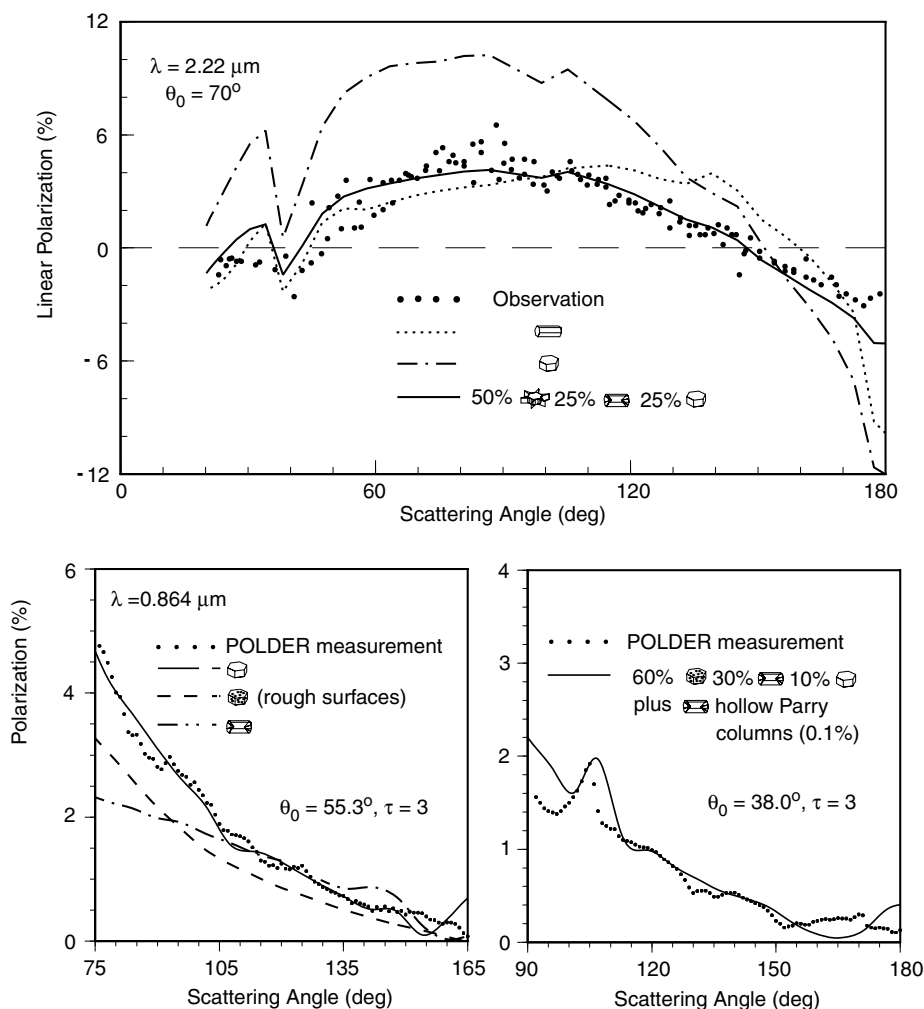
Figure 7.12   The upper panel shows linear polarization of sunlight reflected from cirrus clouds measured at 2.22 μm (Coffeen, 1979). The lower pannel displays full polarization observed from the polarimeter at 0.864 μm on board the POLDER in the scattering-angle domain (Chepfer *et al.*, 1998). The theoretical results are computed for hollow columns, plates, and ice particles with rough surfaces using the best fit optical depth of 3. The lower left panel illustrates comparisons between observed values with theoretical results using 3D randomly oriented plates, rough-surface ice particles, and hollow columns. The lower right panel shows a best interpretation of the observed data, particularly for subsun peak at about the 104° scattering angle, using a combination of 0.1% hollow Parry columns and other 3D randomly oriented ice crystals indicated in the diagram.

bidirectional reflectances in the 1.38 μm H_2O band covering 6600–7500 cm^{-1}. The calculations employ two ice-crystal size distributions having mean effective ice crystal sizes of 42 and 124 μm with a shape composition of 50% aggregates/bullet rosettes, 30% hollow columns, and 20% plates.

Figure 7.13 shows the results for clear and cirrus cloudy conditions in which the midlatitude summer atmosphere water vapor profile is used. The cirrus cloud base is placed at 8 km with an optical depth of 1. The line structure of water vapor absorption
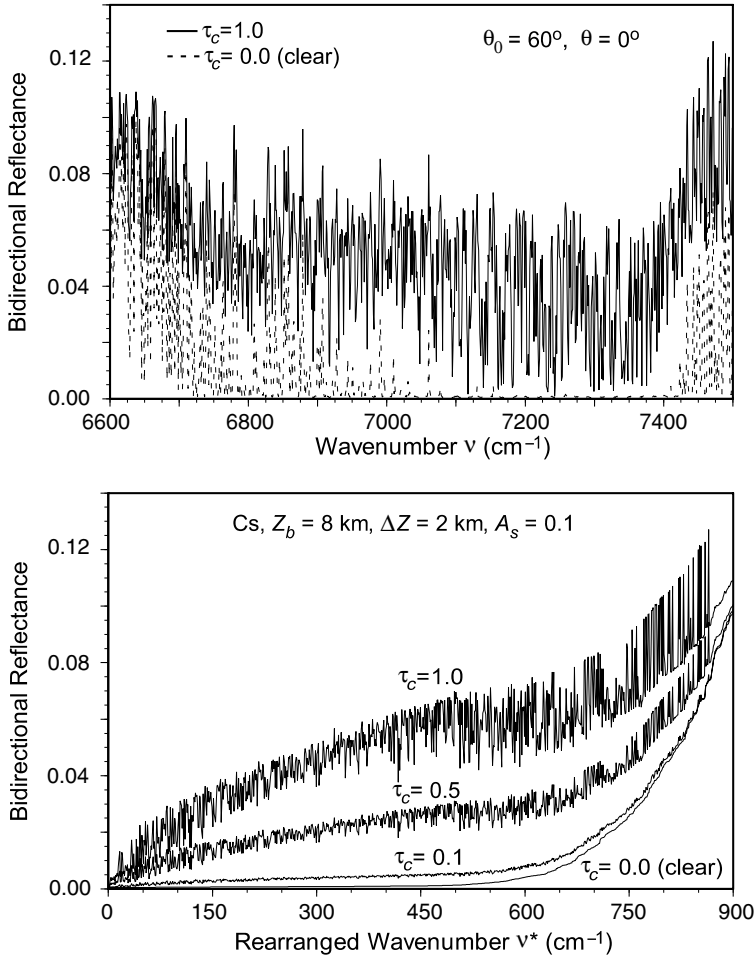

Figure 7.13 The upper diagram shows the bidirectional reflectance in the 1.38 μm water vapor band as a function of wavenumber from 6600 to 7500 cm^{-1} for clear and cirrus cloudy atmospheres. A cirrostratus located at 8 km with a thickness of 2 km in the midlatitude summer atmosphere is used in the calculation. The surface albedo and the solar and emergent angles used are 0.1 and 60° and 0°, respectively. The lower diagram presents the bidirectional reflectance in the rearranged wavenumber domain according to the order of the clear reflectance values, a monotonic increasing curve, for a number of optical depths.

exhibits significant fluctuations. At about 7100–$7400\ \mathrm{cm}^{-1}$, reflectances in clear conditions are extremely small because of strong water vapor absorption. Multiple scattering due to ice crystals contributes to the strength of reflectances in the line-wing regions. It is difficult to examine the full information content of cirrus clouds because of the complexity of the line structure. For this reason, we order the bidirectional line spectra for the clear condition according to their magnitudes in such a manner that a monotonic increasing function is displayed in the rearranged wavenumber domain. Subsequently, the bidirectional line spectra for cirrus cloudy conditions are also ordered in accord with this rearranged wavenumber domain. Low values represent reflectances associated with line centers, whereas high values correspond to line wings.

In the lower panel, the largest reflectance in the line wing corresponding to the surface albedo used is about 0.1 for the clear case. For the small optical depth of 0.1, reflectance increases in the center of the water vapor absorption lines produced by the scattering contribution of ice crystals. The pronounced scattering events that occur at an optical depth of 1 are due to the fact that the scattering and absorption coefficients for ice do not align with the absorption coefficients for water vapor. Sufficient information with respect to the cloud height and ice crystal size, in addition to the optical depth, appears to be present in the rearranged spectrum.

Because of the relative strength of water vapor lines in the 1.38 μm band, it appears that some aspect of the vertical profile of cirrus clouds may be inferred from the spectral bidirectional reflectance measurements. Consider a mixture of ice crystals and water vapor in a predivided layer, Δz. The single-scattering albedo for this layer may be expressed by

$$\tilde{\omega}(\nu) = \frac{\sigma_s}{\sigma_e + k(\nu)} \cong \frac{\tilde{\omega}_c}{1 + 2k(\nu)/\pi D_e^2}, \qquad (7.3.16a)$$

where σ_e and σ_s are the extinction and scattering cross sections for ice particles; $k(\nu)$ is the absorption coefficient in units of cross section; and $\tilde{\omega}_c = \sigma_s/\sigma_e$ is the single-scattering albedo for ice particles where the optical theorem is used to obtain $\sigma_e \cong 2 \cdot \pi (D_e/2)^2$. We may also employ the parameterization equation developed for optical depth denoted in Eq. (7.3.15c) in the form

$$\Delta\tau(\nu) \cong [\mathrm{IWC}(c + b/D_e) + \rho_w\, k(\nu)] \cdot \Delta z, \qquad (7.3.16b)$$

where ρ_w denotes the number density for water vapor. In these two equations all variables are dependent on the predivided layer.

Consider further an optically thin layer such that the reflectance (reflection function) and transmittance (transmission function) are given in Eqs. (6.4.8a) and (6.4.8b). The spectral reflectance can then be written as follows:

$$R(\nu) = \frac{1}{4\mu\mu_0} \frac{P\tilde{\omega}_c(D_e)}{1 + 2k(\nu)/\pi D_e^2} [\mathrm{IWC}(c + b/D_e) + \rho_w\, k(\nu)] \cdot \Delta z. \quad (7.3.17a)$$

A similar expression can also be written for the transmittance (direct + diffuse). For the retrieval of IWC and D_e from the reflectance measurements to be feasible, the term $P\tilde{\omega}_c$ must be expressed in terms of D_e. We may now consider a single two-layer

system such that the combined reflectance via Eq. (6.4.9a) is defined by

$$R_{12}(v) = R_1(v) + \frac{\widetilde{T}_1^*(v)R_2(v)\widetilde{T}_1(v)}{1 - R_1^*(v)R_2(v)}. \tag{7.3.17b}$$

For an optically thin layer, the reflectance and transmittance for radiation from above and below may be assumed to be the same, i.e., $\widetilde{T}_1^* = \widetilde{T}_1$ and $R_1^* = R_1$. Equation (7.3.17b) contains four unknowns: $D_e(1, 2)$ and IWC(1, 2). Thus, four or more spectral reflectance measurements may be selected to perform retrievals. Direct inversion is obviously not feasible, but a numerical solution could be developed. The adding method for reflectance may be extended to a number of layers such that a vertical profile for D_e and IWC may be inferred from a set of carefully selected spectral measurements. The preceding analysis suffices to point out the rich information inherent in the water vapor line spectra reflected from cloudy atmospheres, a subject that has not been explored for the remote sensing of cloud vertical structure.

In Section 3.2.3, we discussed the characteristics of the oxygen absorption bands. The oxygen A-band is produced by the transitions of ground electronic states accompanied by vibrational–rotational transitions and is centered at 13,121 cm^{-1} (red band). The optical depths of the A-band are determined by molecular oxygen (or air) density and therefore are known quantities. The absorption of solar irradiance by the oxygen A-band is similar to but not exactly the same as the 1.38 μm water vapor bands. The A-band radiometer sees the earth's atmosphere principally in the upper troposphere and low stratosphere and, can therefore, be used to infer the position of high-level cirrus clouds, a research area of considerable interest.

7.4   Remote Sensing Using Emitted Infrared Radiation

7.4.1   Theoretical Foundation

We shall first present the theoretical foundation of infrared remote sensing in the context of satellite applications. In a nonscattering atmosphere that is in local thermodynamic equilibrium, the basic equation that governs the transfer of emitted thermal infrared (IR) radiance at a given wavenumber, v, can be described by

$$\mu \frac{dI_v(\tau, \mu)}{d\tau} = I_v(\tau, \mu) - B_v(\tau), \tag{7.4.1}$$

where $\mu = \cos\theta$, θ is the emergent angle, B_v is the Planck function, and the optical depth is defined by

$$\tau = \int_z^{z_\infty} k_v(z')\rho_a(z')\,dz', \tag{7.4.2}$$

with ρ_a the density of the absorbing gases and k_v the absorption coefficient. In thermal IR radiative transfer, radiance in the wavenumber domain is used instead of intensity for reflected and transmitted sunlight in the wavelength domain.

From the basic equation, the solution for upward radiance is given by the following integral equation:

$$I_\nu(\tau, \mu) = I_\nu(\tau_*)e^{-(\tau_*-\tau)/\mu} + \int_\tau^{\tau_*} B_\nu(\tau')e^{-(\tau'-\tau)/\mu}\frac{d\tau'}{\mu}, \qquad (7.4.3)$$

where τ_* is the optical depth at the surface and $I_\nu(\tau_*)$ denotes the emitted surface radiance generally assumed to be isotropic. The first term on the right-hand side represents the surface emission contribution attenuated to the level τ, while the second term denotes the emission contribution of the atmosphere between τ and τ_*.

For application to satellite remote sensing, it suffices to assume that the satellite instrument observes in a narrow cone in the local vertical so that everywhere within the cone the cosine of the emergent angle $\mu \cong 1$, referred to as the upwelling direction. The emitted radiance at the surface $I_\nu(\tau_*) = \varepsilon_\nu B_\nu(T_s)$, where ε_ν is the surface emissivity and T_s is the surface temperature. The emissivities of most of the earth's surfaces in the thermal IR region are close to 1. Thus, for all practical purposes, we may use the Planck function for the emitted radiance at the surface.

Moreover, in remote sensing the exponential terms are generally expressed in terms of the transmittance and weighting function defined in the following. The monochromatic transmittance is defined by

$$T_\nu(\tau) = e^{-\tau}, \qquad (7.4.4)$$

and the weighting function by

$$\frac{\partial T_\nu(\tau)}{\partial \tau} = -e^{-\tau}. \qquad (7.4.5)$$

It follows that at the top of the atmosphere (TOA), we have

$$I_\nu(0) = B_\nu(T_s)T_\nu(\tau_*) + \int_{\tau_*}^0 B_\nu(\tau)\frac{\partial T_\nu(\tau)}{\partial \tau}\, d\tau. \qquad (7.4.6)$$

For application to atmospheric remote sensing, the height or pressure coordinate is usually employed. Height and pressure are related via the hydrostatic equation, $dp = -\rho g dz$, where ρ is the air density and g is the gravitational acceleration. The mixing ratio for a specific gas with density ρ_a is defined as $q = \rho_a/\rho$. Thus, we can rewrite Eq. (7.4.6) in the pressure coordinates as follows:

$$I_\nu(0) = B_\nu(T_s)T_\nu(p_s) + \int_{p_s}^0 B_\nu[T(p)]\frac{\partial T_\nu(p)}{\partial p}\, dp, \qquad (7.4.7)$$

where p_s denotes the surface pressure.

An instrument can distinguish only a finite band width $\Psi(\bar\nu, \nu)$, where Ψ denotes the instrumental response (or slit) function and $\bar\nu$ is the mean wavenumber. The measured radiance from a spectrometer over a wavenumber interval (ν_1, ν_2) in the normalization form is given by

$$I_{\bar\nu} = \int_{\nu_1}^{\nu_2} I_\nu \Psi(\bar\nu, \nu)\, d\nu \Big/ \int_{\nu_1}^{\nu_2} \Psi(\bar\nu, \nu)\, d\nu. \qquad (7.4.8)$$

The effective spectral interval for the response function is usually small enough that the variation of the Planck function is insignificant. We can then replace its value by $B_{\bar{\nu}}(T)$ without introducing noticeable errors. It follows that by carrying out the wavenumber integration over Eq. (7.4.7), we obtain

$$I_{\bar{\nu}}(0) = B_{\bar{\nu}}(T_s)T_{\bar{\nu}}(p_s) + \int_{p_s}^{0} B_{\bar{\nu}}[T(p)]\frac{\partial T_{\bar{\nu}}(p)}{\partial p}\, dp, \qquad (7.4.9)$$

where, when the instrumental response function is accounted for, the spectral transmittance is defined by

$$T_{\bar{\nu}}(p) = \int_{\nu_1}^{\nu_2} \Psi(\bar{\nu}, \nu)\exp\left[-\frac{1}{g}\int_{0}^{p} k_{\nu}(p')q(p')\, dp' \right] d\nu \left/ \int_{\nu_1}^{\nu_2} \Psi(\bar{\nu}, \nu)\, d\nu. \right.$$
$$\qquad (7.4.10)$$

Equation (7.4.9) is fundamental to remote sensing of the atmosphere and the surface from orbiting meteorological satellites. The upwelling radiance is a result of the product of the Planck function, the spectral transmittance, and the weighting function. The temperature information is included in the Planck function, while the density profiles of relevant absorbing gases are involved in the transmittance. Observed radiances will thus be directly or indirectly associated with the temperature and gaseous profiles. Extracting the relevant information about the atmospheric state and composition from observed IR radiances is the essence of remote sensing from space.

We shall now review the potential information content in the thermal IR spectrum (Fig. 4.3). There are four regions over which water vapor, ozone, and carbon dioxide exhibit a significant absorption spectrum. Carbon dioxide absorbs IR radiation in the 15 μm band from about 600 to 800 cm^{-1}. In addition, carbon dioxide also absorbs radiation in the 4.3 μm region that overlaps with solar radiation. Absorption due to ozone is primarily confined to the 9.6 μm band. Water vapor exhibits absorption lines over the entire infrared spectrum. The most pronounced absorption occurs in the 6.3 μm vibrational–rotational band and in the pure rotational band with wavenumbers less than about 500 cm^{-1}. From about 800 to 1200 cm^{-1}, referred to as the atmospheric window, absorption due to atmospheric gases shows a minimum, except in the 9.6 μm ozone band. There are also absorption bands for various greenhouse gases that can be used for their determination by remote sensing: the CH$_4$ 7.6 μm band, the N$_2$O 7.9 μm band, and some CFC lines in the window.

7.4.2   Surface Temperature Determination

If observations are taken in the window region where the effect of the atmosphere is at a minimum, the upwelling radiance at TOA must be closely associated with emission from the surface. Replacing $\bar{\nu}$ by i for convenience of discussion, we may define a mean temperature for the atmosphere, T_a, and simplify Eq. (7.4.9) in the

form

$$I_i \cong B_i(T_s)T_i + B_i(T_a)(1 - T_i), \tag{7.4.11}$$

where we let $T_i = T_i(p_s)$.

We now introduce the split-window technique for the determination of surface temperature that uses observations at two channels to eliminate the term involving T_a and solve for T_s. The value of T_a generally varies by less than 1 K in the window region from about 10.5 to 12.5 μm, in which variability of the surface emissivity is insignificant. The atmospheric transmittance in the window region is primarily produced by the continuous absorption of water vapor and to a good approximation is given by

$$T_i \cong e^{-k_i u} = 1 - k_i u, \tag{7.4.12}$$

where k_i is the absorption coefficient of water vapor for a spectral band in the window and u is the water vapor path length.

Applying the window equation to two channels, we have

$$I_1 = B_1(T_{b1}) = B_1(T_s)T_1 + B_1(T_a)(1 - T_1), \tag{7.4.13}$$

$$I_2 = B_2(T_{b2}) = B_2(T_s)T_2 + B_2(T_a)(1 - T_2), \tag{7.4.14}$$

where we have also expressed the observed radiances I_1 and I_2 in terms of the brightness temperatures T_{b1} and T_{b2}. The objective of the split-window technique is to eliminate T_a, and to do so, we may expand the Planck function of temperature T by means of the Taylor series with respect to T_a in the form

$$B_i(T) = B_i(T_a) + \frac{\partial B_i}{\partial T}(T - T_a). \tag{7.4.15}$$

Applying Eq. (7.4.15) to the two channels with $i = 1, 2$ and eliminating $(T - T_a)$ yields

$$B_2(T) = B_2(T_a) + \frac{\partial B_2}{\partial T} \bigg/ \frac{\partial B_1}{\partial T}[B_1(T) - B_1(T_a)]. \tag{7.4.16}$$

Further, by replacing T by T_{b2} and T_s in Eq. (7.4.16) and utilizing Eq. (7.4.14), after some analysis we obtain the following:

$$B_1(T_{b2}) = B_1(T_s)T_2 + B_1(T_a)(1 - T_2). \tag{7.4.17}$$

By eliminating $B_1(T_a)$ from Eqs. (7.4.17) and (7.4.13), we obtain the split-window equation in the form

$$B_1(T_s) = B_1(T_{b1}) + \eta[B_1(T_{b1}) - B_1(T_{b2})], \tag{7.4.18}$$

where

$$\eta = \frac{1 - T_1}{T_1 - T_2} \cong \frac{k_1}{k_2 - k_1}. \tag{7.4.19}$$

In practice, the Planck function is replaced by the brightness temperature. Since a local linear relation can be established between the two, particularly in a small spectral interval in the window region, we may write

$$T_s \cong T_{b1} + \eta(T_{b1} - T_{b2}). \tag{7.4.20}$$

Sea surface temperatures (SSTs) have been routinely inferred from the operational NOAA satellites using one of the instruments aboard, the AVHRR discussed in Section 7.3.3. The 10.9 and 12.0 μm channels have been used to determine surface temperature, particularly over oceans. At night, the 3.7 μm channel has also been added to increase the accuracy of retrieval. Based on the split-window technique, surface temperature may be expressed by a general form of regression as follows:

$$\text{SST} = aT_{b1} + b(T_{b1} - T_{b2}) - c, \tag{7.4.21}$$

where a, b, and c are empirical coefficents derived from *in situ* observations obtained from drifting buoys (McClain *et al.,* 1985), and T_{b1} and T_{b2} are the brightness temperatures involving a combination of AVHRR 10.9, 12.0, and 3.7 μm channels. The satellite-derived temperatures correspond to the temperature of a surface (skin temperature), whereas the buoy measurements are associated with a layer of water some meters deep. The regression approach of the multichannel technique is used partly to adjust (or tune) the satellite skin temperatures to the *in situ* bulk temperatures and partly to account for the water vapor absorption in the window, particularly in the moist tropical region. Since 1970, global SSTs have been operationally produced and archived. An important part of SST retrieval is the detection and elimination of clouds. Several threshold methods are employed for these purposes based on the bidirectional reflectance of the solar channel in daytime and the emission characteristics of IR channels with respect to the sea surface uniformity in nighttime. The split-window technique has also been used for the determination of surface temperature over land in conjunction with land–atmosphere interaction studies. (Brutsaert *et al.,* 1993).

7.4.3   Remote Sensing of Temperature Profiles

Inference of atmospheric temperature profiles from satellite observations of thermal infrared emission was first suggested by King (1956). In his pioneering paper, King pointed out that the angular radiance (intensity) distribution is the Laplace transform of the Planck intensity distribution as a function of optical depth, and illustrated the feasibility of deriving the temperature profile from satellite intensity scan measurements.

Kaplan (1959) advanced the sounding concept by demonstrating that vertical resolution of the temperature field can be inferred from the spectral distribution of atmospheric emission. Kaplan pointed out that observations in the wings of a spectral band sense deeper into the atmosphere, whereas observations in the band center see only the very top layer of the atmosphere since the radiation mean free path is small. Thus, by properly selecting a set of different sounding wavenumbers, the observed

radiances can be used to make an interpretation leading to the vertical temperature distribution in the atmosphere. This principle is demonstrated in the following.

From Eq. (7.4.9), it is clear that the temperature of the underlying surface must be determined if surface emission represents a significant contribution to the observed radiance. For the following discussion, we may drop the surface term, i.e., assume $T_{\bar{v}}(p_s) = 0$, and write the forward radiative transfer equation in the form

$$I_{\bar{v}} = \int_{p_s}^{0} B_{\bar{v}}[T(p)] \frac{\partial T_{\bar{v}}(p)}{\partial p} \, dp. \tag{7.4.22}$$

The fundamental problem in temperature profile retrieval is how to solve for the function $B_{\bar{v}}[T(p)]$, given a set of observed radiances corresponding to different wavenumbers and the known weighting functions. Since the Planck function is a function of wavenumber, we must first eliminate this dependence in the retrieval. The Planck function is smooth and in a small spectral interval it can be approximated in a linear form as follows:

$$B_{\bar{v}}(T) = c_{\bar{v}} B_{\bar{v}_r}(T) + d_{\bar{v}}, \tag{7.4.23}$$

where $\bar{v}_r$ denotes a fixed reference wavenumber and $c_{\bar{v}}$ and $d_{\bar{v}}$ are fitting coefficients. It follows that Eq. (7.4.22) can be expressed by

$$g_{\bar{v}} = \int_{p_s}^{0} f(p) K_{\bar{v}}(p) \, dp, \tag{7.4.24a}$$

where we let

$$g_{\bar{v}} = (I_{\bar{v}} - d_{\bar{v}})/c_{\bar{v}}, \quad f(p) = B_{\bar{v}_r}[T(p)], \quad K_{\bar{v}}(p) = \partial T_{\bar{v}}(p)/\partial p. \tag{7.4.24b}$$

Equation (7.4.24a), similar to Eq. (7.2.10), is the well-known Fredholm equation of the first kind; $K_{\bar{v}}(p)$ is the weighting function; and $f(p)$ is the function to be recovered from a set of $g_{\bar{v}}$.

To determine atmospheric temperatures from measurements of thermal emission, the source of emission must be a relatively abundant gas of known and uniform distribution. Otherwise, its uncertainty will make the determination of temperature from the measurements ambiguous. There are two gases in the earth–atmosphere system that occur in uniform abundance at altitudes below about 100 km, and which also show emission bands in the spectral regions that are convenient for measurement. As discussed in Section 4.2, carbon dioxide, a minor constituent with a relative volume abundance of about 365 ppm at the present time, exhibits vibrational–rotational lines. In addition, oxygen, a major constituent with a relative volume abundance of 0.21, also satisfies the requirement of a uniform mixing ratio and has a microwave spin-rotational band. The microwave spectrum will be discussed in the next section.

Shown in Fig. 7.14 is a spectrum of outgoing radiance in terms of blackbody temperature in the vicinity of the 15 μm band observed by the Infrared Interfero-meter Spectrometer (IRIS) on board the Nimbus 4 satellite. The equivalent blackbody temperature generally decreases when approaching the band center. This decrease is associated with the decrease of tropospheric temperature as altitude increases. Near
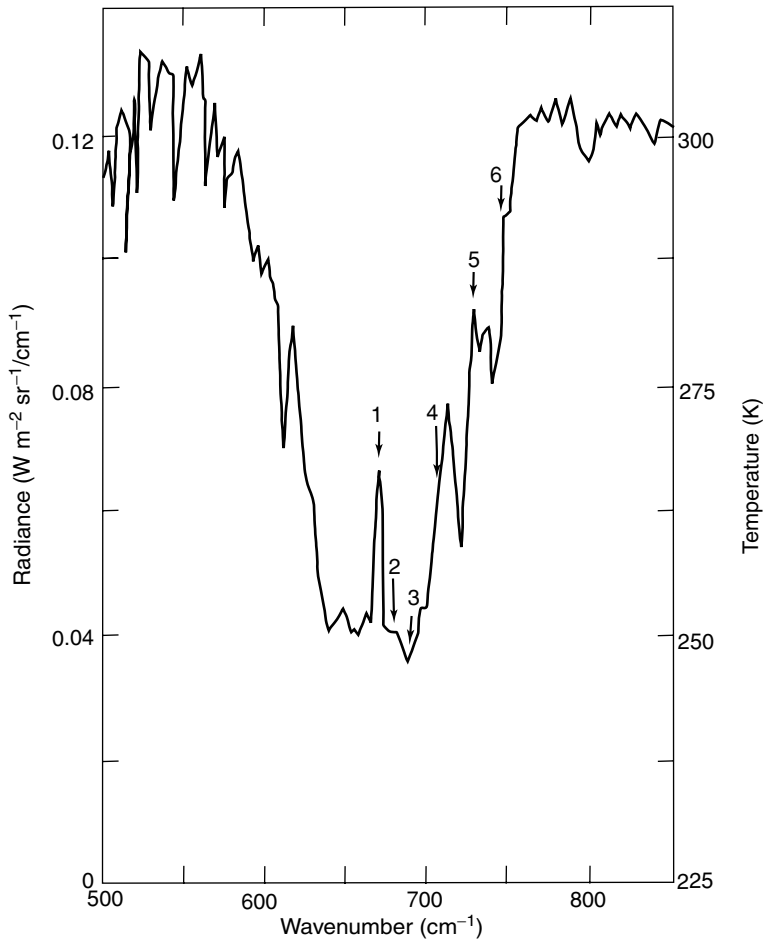
Figure 7.14 Outgoing radiance in terms of blackbody temperature in the vicinity of 15 μm CO_2 band observed by the IRIS on Nimbus 4. The arrows denote the spectral regions sampled by the VTPR instrument (see also Fig. 4.1).

about 690 cm^{-1}, the temperature shows a minimum, which is related to the colder tropopause. Decreasing the wavenumber beyond 690 cm^{-1}, however, increases the temperature. This is due to the increase in temperature in the stratosphere, since the observations near the band center see only the very top layers of the atmosphere. On the basis of the sounding principle discussed above, we can select a set of sounding wavenumbers such that temperature profiles in the troposphere and lower stratosphere can be largely covered. The arrows in Fig. 7.14 indicate an example of such a selection.

The selection of appropriate sounding wavenumbers for temperature retrieval requires an understanding of the behavior of weighting functions. In practice, an ideal weighting function would be a delta function. Weighting functions can be constructed

using known line-by-line absorption data and a program for transmittance calculations via Eq. (7.4.10). As discussed in Section 1.3, the absorption coefficient in the troposphere is slightly dependent on temperature, which can introduce complications in the retrieval of temperature profiles. However, the temperature dependence of transmittances can be accounted for in the retrieval process by building a set of values corresponding to a number of standard atmospheric profiles from which a search can be carried out to obtain the best estimated transmittances for a given temperature profile.

The computation of spectral transmittances through an inhomogeneous atmosphere for satellite remote sensing applications first requires a line-by-line integration effort, prior to the development of simplified or parameterized programs to speed up the computational requirement. In Section 4.2.3, we outlined the procedure for line-by-line calculations in which line shape, strength, and position, along with pressure and temperature dependence, are properly taken into account.

Sounding of the atmospheric temperature for meteorological purposes utilizes the 15 μm and 4.3 μm CO_2 bands. The latter is used at nighttime to enhance temperature retrieval. As discussed in Section 4.2, the 15 μm CO_2 band consists of a number of bands produced by vibrational transitions including the ν_2 fundamentals, combination bands, hot bands, and bands associated with isotopes, with strong Q-branch rotational lines located at the center of the band and P- and R-branch lines almost equally spaced on each side of the band center.

An example of the weighting function and transmittance profiles is shown in Fig. 7.15 for a set of Vertical Temperature Profile Radiometers (VTPR) on the
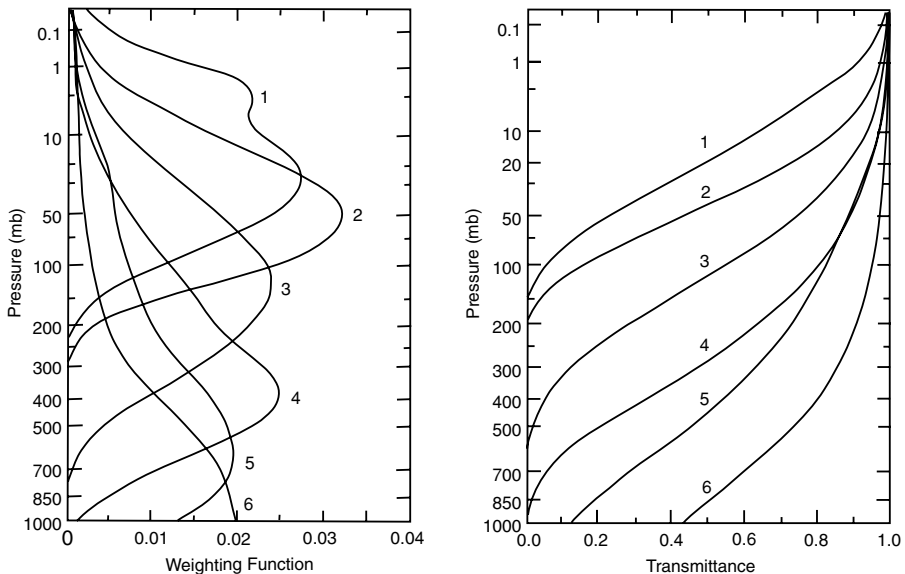

Figure 7.15   The weighting function and transmittance for the NOAA 2 Vertical Temperature Profile Radiometer (VTPR).

NOAA 2 satellite, the first satellite experiment to measure atmospheric temperatures for operational meteorological use. The VTPR consists of 6 channels in the 15 μm CO_2 band, with the nominal center wavenumbers of 668.5, 677.5, 695.0, 708.8, 725.0, and 745.0 cm^{-1} for channels 1–6, respectively. The weighting function curves represent the part of the atmosphere where the upwelling radiance arises. Each peak denotes the maximum contribution to the upwelling radiance. Clearly, radiance is contributed mostly from progressively lower levels as the wavenumber moves from the center to the wing of the band. It is also apparent that the weighting functions overlap somewhat, allowing finite radiance data to define the temperature profile adequately. Operational and practical temperature profile retrievals do not follow the direct inversion methods discussed in Section 7.2.1, but rather employ the nonlinear iteration and physical–statistical methods outlined in the following.

7.4.3.1 NONLINEAR ITERATION METHOD

The difficulty in reconstructing a temperature profile from radiance observations is due to the fact that the Fredholm equation with fixed limits may not always have a solution for an arbitrary function. Because the radiances are derived from measurements that are only approximate, the reduction of the inversion problem to a linear system is mathematically improper and a nonlinear approach to the forward radiative transfer equation appears necessary. Recalling Eq. (7.4.9), we write

$$I_i = B_i(T_s)T_i(p_s) + \int_{p_s}^{0} B_i[T(p)]\frac{\partial T_i(p)}{\partial \ln p}\,d\ln p, \qquad (7.4.25a)$$

where i denotes the number of spectral channels and the weighting function is expressed in logarithmic scale of the pressure. The Planck function in the wavenumber domain may be rewritten in the form

$$B_i(T) = a\nu_i^3 / (e^{b\nu_i/T} - 1), \qquad (7.4.25b)$$

with $a = 2hc^2$ and $b = hc/K$. In reference to the weighting function illustrated in Fig. 7.15, we note that for a given wavenumber, the integrand reaches a maximum at different pressure levels. From the mean value theorem, the observed radiance can be approximated by

$$\hat{I}_i - B_i(T_s)T_i(p_s) \cong B_i[T(p_i)]\left[\frac{\partial T_i(p)}{\partial \ln p}\right]_{p_i}\Delta_i \ln p, \qquad (7.4.26)$$

where p_i denotes the pressure level at which the maximum weighting function is located, and $\Delta_i \ln p$ is the pressure difference at the ith level and is defined as the effective width of the weighting function. Let the guessed temperature at the p_i level be $T^*(p_i)$. Then, the expected radiance is given by

$$I_i^* - B_i(T_s)T_i^*(p_s) = B_i[T^s(p_i)]\left[\frac{\partial T_i^*(p)}{\partial \ln p}\right]_{p_i}\Delta_i \ln p. \qquad (7.4.27)$$

On dividing Eq. (7.4.26) by Eq. (7.4.27) and noting that the dependence of the Planck function is much larger than that of the weighting function, we obtain

$$\frac{\hat{I}_i - B_i(T_s)T_i(p_s)}{I_i^* - B_i(T_s)T_i^*(p_s)} \cong \frac{B_i[T(p_i)]}{B_i[T^*(p_i)]}. \tag{7.4.28}$$

When the surface contribution to the upwelling radiance is small or dominant, Eq. (7.4.28) may be approximated by

$$\frac{\hat{I}_i}{I_i^*} \cong \frac{B_i[T(p_i)]}{B_i[T^*(p_i)]}. \tag{7.4.29}$$

This is referred to as the relaxation equation (Chahine, 1970; Smith, 1970). We may now devise iterative procedures to retrieve the temperature profile $T^{(n)}(p_i)$ at level p_i where n is the order of iterations as follows:

(a) Make an initial guess for $T^{(n)}(p_i)$, $n = 0$.
(b) Substitute $T^{(n)}(p_i)$ into Eq. (7.4.25a) and use an accurate quadrature formula to compute the expected upwelling radiance $I_i^{(n)}$ for each sounding channel.
(c) Compare the computed radiance values $I_i^{(n)}$ with the measured data $\hat{I}_i$. If the residuals $R_i^{(n)} = |\hat{I}_i - I_i^n|/\hat{I}_i$ are less than a preset small value (e.g., 10^{-4}) for each sounding channel, then $T^{(n)}(p_i)$ is a solution. If not, continue the iteration.
(d) Apply the relaxation equation (7.4.29) M times to generate a new guess for the temperature values $T^{(n+1)}(p_i)$ at the selected i pressure level, i.e., force the temperature profile to match the observed radiances. From Eqs. (7.4.29) and (7.4.25b), we have

$$T^{(n+1)}(p_i) = bv_i/\ln\big\{1 - [1 - \exp(bv_i/T^{(n)}(p_i))]I_i^{(n)}/\hat{I}_i\big\}, \quad i = 1, 2, \ldots, M.$$

(e) Carry out the interpolation between the temperature value at each given level p_i to obtain the desired profile (it suffices to use linear interpolation in the retrieval).
(f) Finally, go back to step (b) and repeat until the residuals are less than a preset criterion.

The relaxation method could, in principle, fail to converge or converge to the wrong solution. The former will be obvious and the solution can be rejected. The latter requires numerical experiments to demonstrate whether the method has converged to a correct solution. Exercise 7.6 is an example of using the relaxation method to derive a temperature profile.

7.4.3.2 MINIMUM VARIANCE METHOD: HYBRID RETRIEVAL

In many remote sensing problems, the errors encountered are statistical. Hence, it is desirable to take into account the statistical nature of the measurement errors and available information when considering the inversion problem. In the statistical approach, it is customary to assume that the deviation of predicted (or estimated) parameters (in the present case the temperature) from the climatological mean can be expressed as a linear combination of the deviation of measured data (in this case the

radiance). Under this assumption, we have

$$\hat{T}_j - \bar{T}_j = \sum_{i=j}^{M} D_{ji}(\hat{I}_i - \bar{I}_i), \qquad j = 1, 2, \ldots, N, \tag{7.4.30}$$

where j denotes the atmospheric level, $\hat{T}_j$ is the predicted value of T_j, which represents the "true" temperature, $\hat{I}_i$ is the observed radiance, $\|D_{ji}\|$ represents a certain predictor matrix, and the climatological means of T_j and I_i (the "true" radiance) are defined by a statistical ensemble, denoted by x, of available temperature profiles and radiances in the forms

$$\bar{T}_j = \frac{1}{X} \sum_{x=1}^{X} T_{jx}, \quad \bar{I}_i = \frac{1}{X} \sum_{x=1}^{X} I_{ix}. \tag{7.4.31}$$

In matrix from, Eq. (7.4.30) can be written

$$\hat{\mathbf{T}} - \bar{\mathbf{T}} = \mathbf{D}(\hat{\mathbf{I}} - \bar{\mathbf{I}}). \tag{7.4.32}$$

Thus, once $\mathbf{D}$ is known the predicted temperature vector can be determined from the observed radiance vector.

We wish to find a linear predictor which will give the minimum square deviation of the predictor profile from the true profile defined by

$$\sum_{x=1}^{X}(T_{jx} - \hat{T}_{jx})^2 = \sum_{x=1}^{X}\left[(T_{jx} - \bar{T}_j) - (\hat{T}_{jx} - \bar{T}_j)\right]^2, \qquad j = 1, 2, \ldots, N. \tag{7.4.33}$$

Using Eq. (7.4.30) and searching the minimum with respect to the linear predictor yield

$$\frac{\partial}{\partial D_{jk}}\left\{ \sum_{x=1}^{X}\left[(T_{jx} - \bar{T}_j) - \sum_{i=j}^{M} D_{ji}(\hat{I}_{ix} - \bar{I}_i)\right]^2 \right\} = 0,$$
$$j = 1, 2, \ldots, N, \qquad k = 1, 2, \ldots, M. \tag{7.4.34}$$

It follows that

$$\sum_{x=1}^{X}(T_{jx} - \bar{T}_j)(\hat{I}_{kx} - \bar{I}_k) - \sum_{i=1}^{M} D_{ji} \sum_{x=1}^{X}(\hat{I}_{ix} - \bar{I}_i)(\hat{I}_{kx} - \bar{I}_k) = 0. \tag{7.4.35a}$$

In matrix form, we write

$$\sum_{x=1}^{X}(\mathbf{T}_x - \bar{\mathbf{T}})(\hat{\mathbf{I}}_x - \bar{\mathbf{I}})^{\mathrm{T}} - \mathbf{D}\sum_{x=1}^{X}(\hat{\mathbf{I}}_x - \bar{\mathbf{I}})(\hat{\mathbf{I}}_x - \bar{\mathbf{I}})^{\mathrm{T}} = 0, \tag{7.4.35b}$$

where $\mathbf{T}$ is an $N \times 1$ matrix, $\mathbf{I}$ is an $M \times 1$ matrix, and $\mathbf{D}$ is an $N \times M$ matrix. Further, let the experimental random error vector due to system noise of a radiometer be ε. Thus, the observed radiance vector is then

$$\hat{\mathbf{I}} = \mathbf{I} + \varepsilon, \tag{7.4.36}$$

where $\mathbf{I}$ is the "true" radiance vector mentioned earlier. Substituting Eq. (7.4.36) into Eq. (7.4.35b) and noting that the measurement error vector is uncorrelated with the temperature and radiance vectors, we have

$$\sum_{x=1}^{X}(\mathbf{T}_x - \mathbf{T})(\mathbf{I}_x - \mathbf{I})^{\mathrm{T}} - \mathbf{D}\sum_{x=1}^{X}\left[(\mathbf{I}_x - \mathbf{I})(\mathbf{I}_x - \mathbf{I})^{\mathrm{T}} + \varepsilon\varepsilon^{\mathrm{T}}\right] = 0. \quad (7.4.37)$$

Define the covariance matrix for any two variables as follows:

$$\mathbf{C}(\mathbf{T}_x, \mathbf{I}_x) = \frac{1}{X}\sum_{x=1}^{X}\mathbf{T}_x\mathbf{I}_x^{\mathrm{T}}. \quad (7.4.38)$$

Thus, the predictor matrix can be expressed in terms of the covariance matrix in the form

$$\mathbf{D} = \mathbf{C}(\Delta\mathbf{T}_x, \Delta\mathbf{I}_x)[\mathbf{C}(\Delta\mathbf{I}_x, \Delta\mathbf{I}_x) + \mathbf{C}(\varepsilon_x, \varepsilon_x)]^{-1}, \quad (7.4.39)$$

where $\mathbf{C}(\varepsilon_x, \varepsilon_x)$ represents the noise covariance matrix, and

$$\Delta\mathbf{T}_x = \mathbf{T}_x - \bar{\mathbf{T}}, \quad \Delta\mathbf{I}_x = \mathbf{I}_x - \bar{\mathbf{I}}. \quad (7.4.40)$$

The covariance matrix can be constructed empirically by collecting coincidences of radiances derived from satellites and temperatures obtained from radiosondes or rocket soundings. Normally, the $\mathbf{D}$ matrix is built to give a dimension $N \times M$ such that $N > M$. In this manner, more temperature values can be inferred from a limited set of radiance observations. The $\mathbf{D}$ matrix is thus determined entirely from available data sets and information concerning the weighting function is not required. Although the statistical method does not require a good first-guess profile, acquiring a representative data set is crucial to its success. This data set must be large enough to ensure that the retrieval matrix is stable, must be collected for each satellite, and must be updated frequently to cover different seasons and latitudinal zones. The most advantageous aspect of the statistical method is the computational efficiency afforded by Eq. (7.4.32), which is important for operational purposes.

The minimum variance method utilizes the same approach as the statistical method but does not require a large data set and uses weighting functions similar to physical retrievals. Consider the basic forward radiative transfer equation denoted in Eq. (7.4.22) and write it in the form

$$I_i = \int_{p_s}^{0} B_i[T(p)]K_i(p)\,dp, \qquad i = 1, 2, \ldots, M. \quad (7.4.41)$$

Let the climatological (or standard) temperature profile be $\bar{T}(p)$ and let the radiance corresponding to this profile be $\bar{I}$. Expanding the Planck function linearly with respect to this temperature, we have

$$I_i - \bar{I}_i = \int_{p_s}^{0} \frac{\partial B_i[T(p)]}{\partial p}K_i(p)\,dp[T(p) - \bar{T}(p)]. \quad (7.4.42)$$

Using the quadrature summation for the integration and employing the notation defined in Eq. (7.4.40), we have

$$\Delta I_i = A_{ij} \Delta T_j, \qquad (7.4.43a)$$

where

$$A_{ij} = \sum_{j=1}^{N} \left\{ \frac{\partial B_i[T(p)]}{\partial p} K_i(p) \right\}_{p_j} \Delta p_j. \qquad (7.4.43b)$$

In matrix form, we have

$$\mathbf{\Delta I} = \mathbf{A} \, \mathbf{\Delta T}. \qquad (7.4.44)$$

Substituting Eq. (7.4.44), which correlates the temperature deviation with the radiance deviation via a matrix **A,** into the predictor matrix derived in Eq. (7.4.39), we have

$$\mathbf{D} = \mathbf{C_T A^T} \left(\mathbf{A C_T \, A^T} + \mathbf{C}_\varepsilon \right)^{-1}, \qquad (7.4.45a)$$

$$\mathbf{C_T} = \frac{1}{X} \sum_{x=1}^{X} \Delta\mathbf{T}_x \Delta\mathbf{T}_x^T, \qquad (7.4.45b)$$

$$\mathbf{C}_\varepsilon = \frac{1}{X} \sum_{x=1}^{X} \varepsilon_x \varepsilon_x^T. \qquad (7.4.45c)$$

Equations (7.4.32) and (7.4.45a)–(7.4.45c) constitute the so-called *minimum variance method*. The components in the predictor matrix can be determined separately; **A** can be calculated from the transmittances; **C_T** can be determined from a sample of radiosonde soundings; and **C**$_\varepsilon$ can be obtained from instrument calibration in the laboratory. In this manner, a large data set of collocated radiosonde and satellite soundings is no longer required.

Although operational retrievals of temperature profiles have been routinely performed over the past 25-plus years, the techniques and procedures used have undergone constant refinement and improvement. This is a result of the complicated nature of the problem, in which consistent and accurate performance is difficult to achieve. It is particularly so when clouds are involved. Radiances from operational satellites, NOAA and GOES, are converted into temperature soundings through an involved algorithm in which retrieval, such as use of the minimum variance method, is only a small part of the process. The NOAA satellites have three sounders: the High Resolution Infrared Radiation Sounder 2 (HIRS/2), the Microwave Sounding Unit (MSU), and the Stratospheric Sounding Unit (SSU). Together they are referred to as the TIROS N Operational Vertical Sounder (TOVS). The TOVS data have been routinely processed to obtain temperature and humidity soundings in connection with numerical weather prediction.
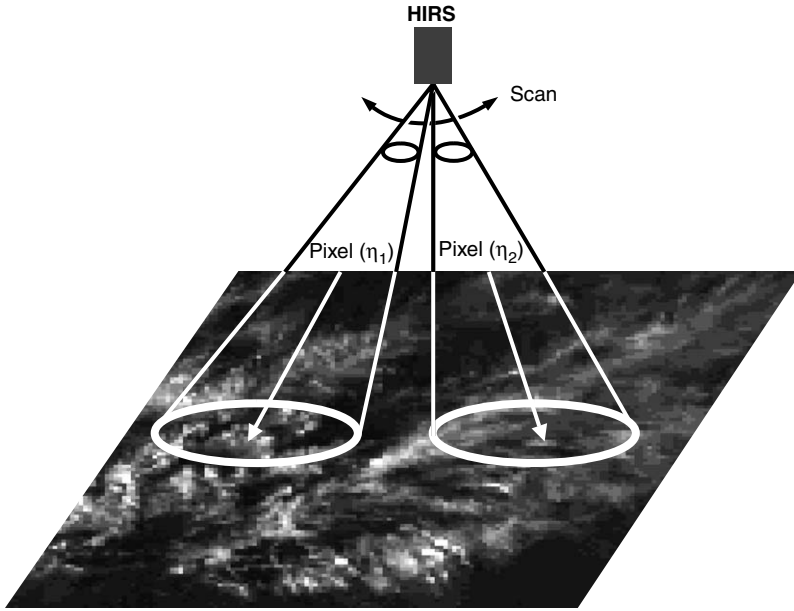
Figure 7.16   Configuration for the adjacent pixels ($\sim$20 km) in a partly cloudy condition for the removal of cloud contribution in the temperature retrieval algorithm using HIRS channels. η_1 and η_2 denote cloud covers in the two pixels. The picture displays AVHRR visible images ($\sim$1 km).

7.4.3.3   CLOUD REMOVAL

In many temperature retrieval cases, the major problem is due to the presence of clouds in the field of view (FOV) of the sounding radiometers. It is, therefore, critically important to remove the cloud effect prior the temperature retrieval. Consider a pair of adjacent pixels (scan spots), as shown in Fig. 7.16, and let the radiances for the ith channel over clear and cloudy areas be I_i^{clr} and I_i^{cld}, respectively. Then, the radiances for pixels 1 and 2 are given by

$$\hat{I}_{i1} = (1 - \eta_1)I_{i1}^{\text{clr}} + \eta_1\,I_{i1}^{\text{cld}},$$
$$\hat{I}_{i2} = (1 - \eta_2)I_{i2}^{\text{clr}} + \eta_2\,I_{i2}^{\text{cld}}, \qquad (7.4.46)$$

where η_1 and η_2 are the effective cloud covers, the product of cloud cover and emissivity, for the respective pixels. If the optical properties of the clouds in the adjacent pixels are the same for the sounding channels, and the temperature fields in the adjacent pixels are also the same, then $I_{i1}^{\text{clr}} = I_{i2}^{\text{clr}} = I_i^{\text{clr}}$, and $I_{i1}^{\text{cld}} = I_{i2}^{\text{cld}} = I_i^{\text{cld}}$. Thus, we obtain

$$N^* = \frac{\eta_1}{\eta_2} = \frac{I_i^{\text{clr}} - \hat{I}_{i1}}{I_i^{\text{clr}} - \hat{I}_{i2}}. \qquad (7.4.47)$$

If we know in advance the N^*, which is independent of channels, we can then determine the clear column radiance from the following equation:

$$I_i^{\text{clr}} = \frac{\hat{I}_{i1} - \hat{I}_{i2}N^*}{1 - N^*}. \qquad (7.4.48)$$

The preceding outlines the essence of the N^* method for the removal of cloud contribution in the FOV of the radiometer. It is subject to the following restrictions: (a) the assumption that adjacent clouds are of the same height, temperature, and optical properties; (b) the effective cloud covers η_1 and η_2 must be different; otherwise, $N^* = 1$, and the solution for I_i^{clr} is singularity; and (c) additional information is required to determine I_i^{clr} from the value of N^*.

The conventional approach is to use an independent channel, say M, in the microwave to determine N^* such that

$$N^* = \frac{I_M^{\text{clr}} - \hat{I}_{M1}}{I_M^{\text{clr}} - \hat{I}_{M2}}. \qquad (7.4.49)$$

However, microwave measurements are usually subject to errors caused by poor resolution, contamination by precipitating clouds, and uncertainty in the estimated surface emissivity. As shown in McMillan and Dean (1982), many empirical procedures and threshold tests are required for the processing of TOVS soundings from NOAA satellites to detect and correct for clouds in connection with temperature retrieval.

Figure 7.17 shows an example of the temperature retrieval accuracy from TOVS data with respect to radiosonde soundings during the entire global weather experiment year in 1979 in terms of root-mean-square differences (Smith, 1991). The collocation and time differences between the two data sources are within about 200 km and ±3 hours. The error differences were due primarily to the poor vertical resolution of the TOVS compared to that of the radiosondes. In clear and partly cloudy conditions, error differences are 2–3 K and they increase in overcast cloud conditions. The reduced accuracy of overcast retrievals is due to the limited number of tropospheric microwave sounding channels and their poor vertical resolution, which result in ineffective cloud removal (see Section 7.5.3 for microwave temperature retrievals).

Many analyses appear to indicate that poor vertical resolution can be the primary source of error that limits the use of current satellite soundings for weather analysis/forecast operations. More advanced sounding instruments that have been developed are the Advanced Infrared Radiation Sounder (AIRS) (Chahine *et al.,* 1984), which will be on board the NASA EOS/Aqua satellite, and the High spectral resolution Interferometer Sounder (HIS), cited in Section 4.2, which is being planned for both the geostationary and polar platforms. The former is a grating spectrometer; the latter is a Michelson interferometer covering a spectral region from about 3.5 to about 19 μm with high spectral resolution ($\lambda/\Delta\lambda > 2000$) (Smith *et al.,* 1995). The goal of future atmospheric infrared sounder observations is to provide an overall accuracy of about 1 K with a vertical resolution of 1 km in temperature retrieval. Clearly, the
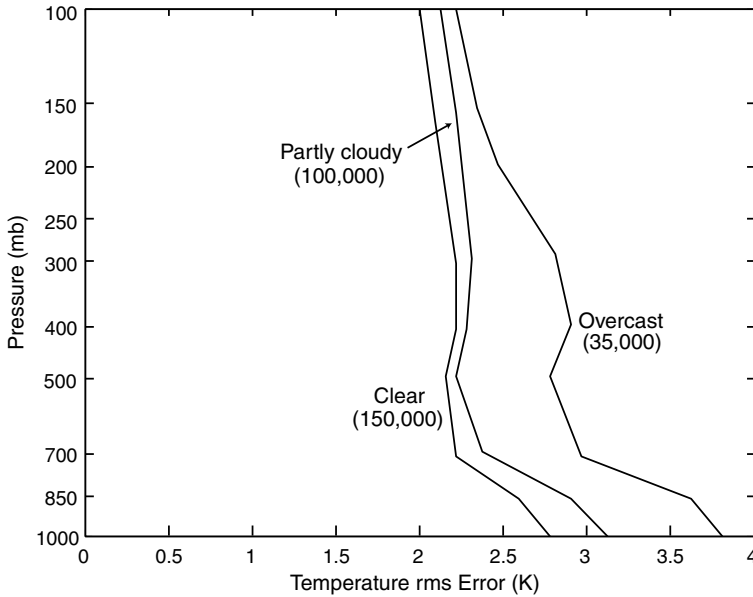
Figure 7.17   Root-mean-square differences between TOVS and radiosonde soundings during the entire global weather experiment year in 1979. The collocation and time differences for the two data sets are generally within 200 km and 3 hours. The number of cases employed in the retrieval for clear, partly cloudy, and overcast conditions are indicated in the diagram (data taken from Smith, 1991).

search for efficient and physically based retrieval programs employing a finite number of spectral channels to achieve this goal is still a subject of ongoing research and development.

7.4.4   Remote Sensing of Water Vapor and Trace Gas Profiles

7.4.4.1   WATER VAPOR FROM THE 6.3 μm VIBRATIONAL–ROTATIONAL BAND
Recalling Eq. (7.4.9) and performing integration by parts on the integral term, we find

$$I_{\bar{\nu}} = B_{\bar{\nu}}[T(0)] - \int_{p_s}^{0} T_{\bar{\nu}}(p) \frac{\partial B_{\bar{\nu}}(p)}{\partial p}\, dp, \qquad (7.4.50)$$

where $T(0)$ denotes the temperature at the top of the atmosphere and the spectral transmittance

$$T_{\bar{\nu}}(p) = \int_{\Delta\nu} \exp\left[-\int_{0}^{p} k_{\nu}(p)\, du(p) \right] \frac{d\nu}{\Delta\nu}. \qquad (7.4.51)$$

We have used the path length $u(g\ cm^{-2})$ to denote the integration in the transmittance.

If the temperature profile has been retrieved from the 15 and 4.3 μm CO_2 bands, then the remaining unknown is the transmittance. Further, if we select wavenumbers

in the 6.3 μm vibrational–rotational band of water vapor at which the absorption lines are given, then the only unknown is the path-length profile. The basic radiative transfer equation for the inference of gaseous profiles is more complicated than that for temperature retrieval. There is no clear-cut mathematical analysis that can be followed to invert the gaseous density profile. Nevertheless, one may devise numerical procedures for the determination of water vapor path-length profiles (Smith, 1991). The determination of water vapor parameters from satellite remote sensing, which would provide the required data for an understanding of the global hydrological cycle of the earth's atmosphere, is a critical task. Yet the accuracy of retrieval from passive sounders has been limited, partly because of the highly varying humidity field and the small amounts of water substance in the upper troposphere.

In principle, the concentration of greenhouse gases, O_3, N_2O, CH_4, and CFCs, can be inferred from nadir-looking spectrometers. Ozone exhibits vibrational–rotational lines in the 9.6 μm band. However, because of the structure of the O_3 concentration, having its maximum located in the stratosphere, the nadir-looking radiometers based on thermal emission have not been designed for retrieval purposes. Instead, reflected sunlight has been used for monitoring the total ozone concentration. N_2O and CH_4 have line structures in the 7.9 and 7.6 μm regions, as do other minor gases, and because of the relatively small mixing ratios, remote sensing of their concentrations utilizes the limb scanning technique.

7.4.4.2 LIMB SCANNING TECHNIQUE

A collimated radiometer or spectrometer, viewing horizontally, recovers radiation from the atmosphere over a layer that is relatively narrow in height, referred to as limb radiation. The general approach for obtaining profiles of trace constituents from limb measurements is known as limb sounding. A series of satellite experiments have used this method to retrieve the trace constituent profiles in the middle atmosphere, specifically the stratosphere.

The geometry of limb viewing is illustrated in Fig. 7.18. A radiometer that receives radiation emitted by the atmosphere along a ray path is identified by the tangent height closest to the surface. The atmosphere can be scanned by sweeping the view direction vertically or horizontally. There are a number of advantageous features of limb scanning for atmospheric probes: (a) Emission originates in the few kilometers immediately above the tangent point because of the rapid decrease of atmospheric density and pressure. Thus, a high inherent vertical resolution may be obtained. (b) All radiation received comes solely from the atmosphere. Variation of a changing underlying surface, which occurs when a nadir-viewing instrument is utilized, is not present. (c) A large degree of opacity is involved along a horizontal path. Hence, the limb technique is particularly useful for the determination of minor gases in the middle atmosphere. (d) The viewing direction from the satellite can be oriented in any azimuthal direction relative to the satellite motion and covers a large area. One disadvantage of this method is the interference of high clouds along the ray path, which act as bodies of infinite opacity and can produce considerable uncertainty in the emitted radiation. In addition, the sharp vertical weighting function, related to a
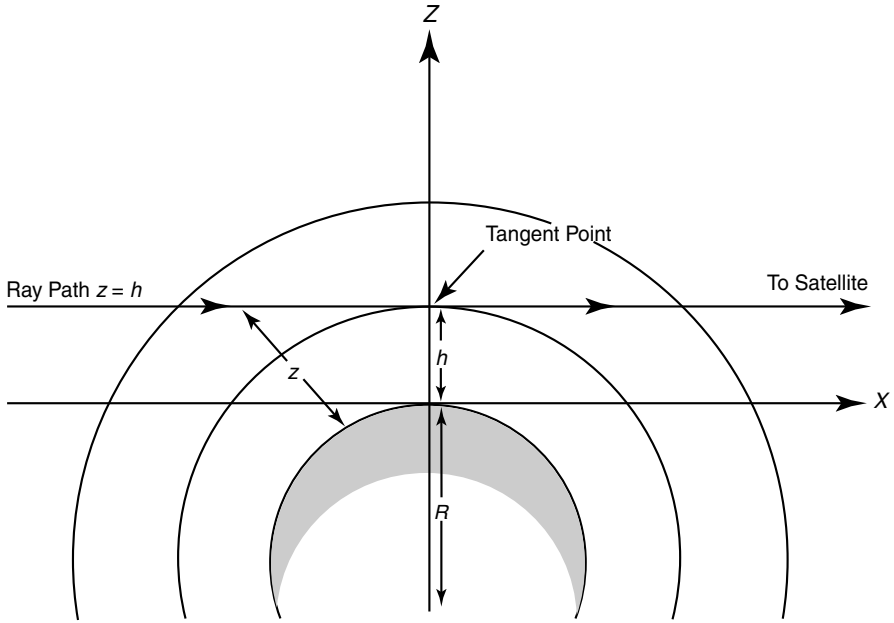
Figure 7.18 The geometry of limb viewing (see also Fig. 7.4). The long-path emission and absorption without the interference from the underlying surface are particularly useful for the inference of minor gases in the middle atmosphere.

horizontal region stretching 200 km or more along the ray path, leads to problems of interpretation of large changes in the atmospheric state over this distance. For these reasons, the limb scanning technique has been shown to be most useful for the inference of composition and structure of the stratosphere and mesosphere.

In reference to the limb viewing geometry shown in Fig. 7.18, the solution of the fundamental radiative transfer equation for a nonscattering atmosphere in local thermodynamic equilibrium can be expressed by

$$I_{\bar{\nu}}(h) = \int_{-\infty}^{\infty} B_{\bar{\nu}}[T(x)] \frac{\partial T_{\bar{\nu}}(h, x)}{\partial x} \, dx, \tag{7.4.52}$$

where x is the distance coordinate along the ray path with the origin at the tangent point. The principle of the temperature and gaseous profile inversion problems is similar to that discussed in the previous sections. However, because of the spherical geometry involved, it is necessary to change from variable x to z in order to obtain the temperature and gaseous profiles as functions of height in the atmosphere. Thus, the limb viewing radiance may be written in the form

$$I_{\bar{\nu}}(h) = \int_{0}^{\infty} B_{\bar{\nu}}[T(z)] K_{\bar{\nu}}(h, z) \, dz, \tag{7.4.53}$$
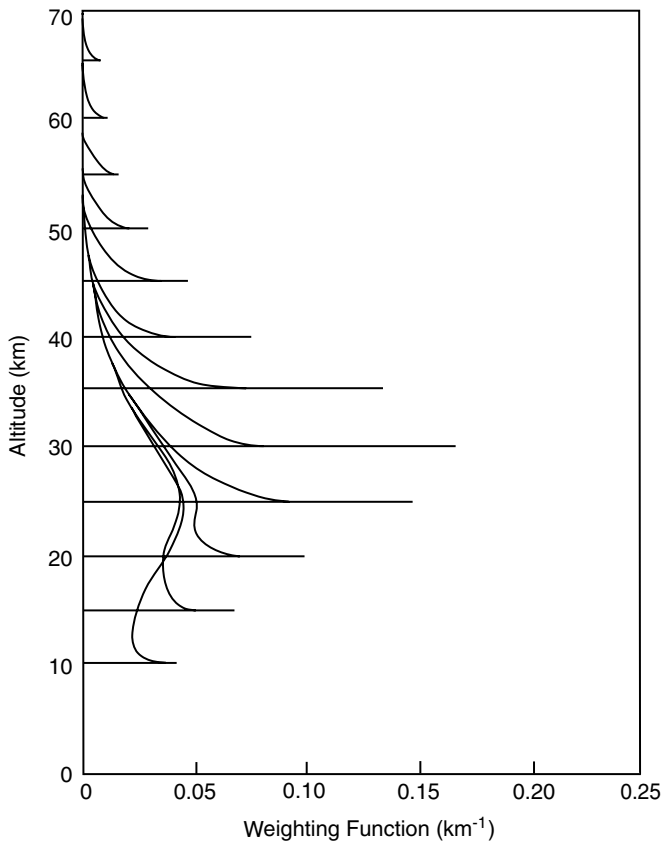
Figure 7.19   Limb viewing weighting function for the ideal case of an instrument with an infinitesimal vertical field of view for the spectral band 585–705 cm^{-1} covering most of the 15 μm band of CO_2 (after Gille and House, 1971).

where $K_{\bar{\nu}}$ represents the weighting function, which is a function of the geometrical factors and the spectral band model used with respect to height z. Figure 7.19 shows the limb viewing weighting function for a hypothetical instrument with an infinitesimal vertical field-of-view for a wide spectral band 585–705 cm^{-1} covering most of the 15 μm CO_2 band. For tangent heights above 25 km, the major part of the contribution comes from within about 3 km of the tangent height. Below 25 km, the weighting function takes on the broader shape of the nadir-viewing weighting functions, although a spike still remains at that tangent point. In principle, inversion of limb radiance measurements may be carried out utilizing the same techniques as in nadir-looking radiance observations.

The most significant application of the limb scanning radiometer has been in the determination of the temperature structure and minor gaseous concentrations of the

middle atmosphere, where nadir-looking radiometers have considerable difficulty deriving sufficient information for their recovery. Pioneering work on the retrieval of temperatures from limb measurements has been carried out by Gille and House (1971). Three infrared limb sounders have flown on the Nimbus satellites, beginning on Nimbus 6, for temperature, water vapor, and other trace gas studies. More recently, the NASA Upper Atmosphere Research Satellite (UARS) was launched in September, 1991, which included the Cryogenic Limb Array Etalon Spectrometer for atmospheric infrared emission measurements. In addition to measurements of the radiation emitted by the Q branch of CO_2 as a function of relative altitude for temperature retrievals, this spectrometer also measured the emission lines of O_3, CH_4, N_2O, and other trace gases associated with ozone destruction (Gille *et al.,* 1996).

   In the stratosphere, the geostrophic approximation, in which the geostrophic wind is related to the horizontal gradient of the thickness, may be applicable to a good approximation. The horizontal equation of motion is given by

$$\left(\frac{d\mathbf{v}}{dt}\right)_H = g\nabla_H p - f\mathbf{k} \times \mathbf{v}, \tag{7.4.54a}$$

where $\nabla_H p = \nabla_p z$ is the pressure gradient force, $\mathbf{k}$ is the unit vector in the vertical direction, and f is the Coriolis parameter. The balance between the pressure gradient force and the Coriolis force gives the geostrophic wind velocity:

$$\mathbf{v}_g = -(g/f)\nabla_p z \times \mathbf{k}. \tag{7.4.54b}$$

Let $\mathbf{v}_{g1}$ and $\mathbf{v}_{g2}$ correspond to heights z_1 and z_2, respectively, such that $z_2 > z_1$. Then, the variation of the geostrophic wind velocity is

$$\Delta\mathbf{v}_g = \mathbf{v}_{g2} - \mathbf{v}_{g1} = -(g/f)\nabla_p(\Delta z) \times \mathbf{k}. \tag{7.4.54c}$$

From the hydrostatic equation $dp = -\rho g\, dz$, where ρ is the air density, and the equation of state $p = \rho RT$, we obtain

$$\Delta z = \int_{z_1}^{z_2} dz = z_2 - z_1 = -\frac{R}{g}\int_{p_1}^{p_2} T(p)\frac{dp}{p}, \tag{7.4.54d}$$

where R is the gas constant. Consequently, if temperatures are known between p_1 and p_2, then from Eqs. (7.4.54c) and (7.4.54d), the vertical change in the geostrophic wind between two pressure surfaces can be estimated. If the geostrophic wind at pressure level p_1 is known, an estimate of the geostrophic wind at pressure p_2 can then be derived.

   The limb scanning radiometer is capable of determining the vertical temperature from about 10 to 1 mb. The temperature data from satellites can then provide the required wind data essential to the understanding of stratospheric dynamics.

7.4.5   Infrared Remote Sensing of Clouds

7.4.5.1   CARBON DIOXIDE SLICING TECHNIQUE FOR CLOUD TOP PRESSURE AND EMISSIVITY

Consider a FOV consisting of a cloud layer located at a pressure level p_c with a temperature T_c. Let the fraction of cloud cover be η and the cloud emissivity be ε_ν. For purposes of illustration, we shall consider monochromatic radiative transfer such that the transmittance multiplication follows exponential operations. The radiance observed at the satellite can be written in the form

$$\hat{I}_\nu = (1 - \eta\varepsilon_\nu)\left[B_\nu(T_s)T_\nu(p_s, p_c) + \int_{p_s}^{p_c} B_\nu(p)\frac{\partial T_\nu(p, p_c)}{\partial p} dp \right]T_\nu(p_c, 0)$$

$$+ \eta\varepsilon_\nu B_\nu(T_c)T_\nu(p_c, 0) + \int_{p_c}^{0} B_\nu(p)\frac{\partial T_\nu(p, 0)}{\partial p} dp, \tag{7.4.55}$$

where we have sliced the atmosphere above and below the cloud and defined the monochromatic transmittance in the form

$$T_\nu(p_1, p_2) = \exp\left(-\frac{1}{g} \int_{p_1}^{p_2} k_\nu(p)q(p) dp \right). \tag{7.4.56a}$$

The four terms in Eq. (7.4.55) are the radiation emitted from the surface, the contribution from the atmosphere below the cloud, the cloud contribution, and the contribution from the atmosphere above the cloud; all at TOA. Based on the definition of monochromatic transmittance, we have

$$T_\nu(p_s, p_c) \times T_\nu(p_c, 0) = T_\nu(p_s, 0), \quad T_\nu(p, p_c) \times T_\nu(p_c, 0) = T_\nu(p, 0), \tag{7.4.56b}$$

and so on.

For a clear FOV, $\eta\varepsilon_\nu = 0$ and the satellite measured radiance is

$$I_\nu^{\text{clr}} = B_\nu(T_s)T_\nu(p_s, 0) + \int_{p_s}^{0} B_\nu(p)\frac{\partial T_\nu(p, 0)}{\partial p} dp. \tag{7.4.57}$$

Subtracting the clear FOV radiance from the cloudy FOV radiance leads to the following result:

$$\hat{I}_\nu - I_\nu^{\text{clr}} = -\eta\varepsilon_\nu B_\nu(T_s)T_\nu(p_s, p_c)$$

$$-\eta\varepsilon_\nu \int_{p_s}^{p_c} B_\nu(p)\frac{\partial T_\nu(p, 0)}{\partial p} dp + \eta\varepsilon_\nu B_\nu(T_c)T_\nu(p_c, 0). \tag{7.4.58a}$$

This is the cloud signal in the satellite measured radiances for wavenumber ν; it is the radiance difference of the cloudy FOV from the neighboring clear FOVs. After performing integration by parts, we obtain

$$\hat{I}_\nu - I_\nu^{\text{clr}} = \eta\varepsilon_\nu \int_{p_s}^{p_c} T_\nu(p, 0)\frac{\partial B_\nu(p)}{\partial p} dp. \tag{7.4.58b}$$

Strictly speaking, this equation is valid only under the assumption of monochromatic radiation in which the transmittance multiplication follows the exponential rule. We may now apply this equation to two spectral bands in the 15 μm CO_2 band, denoted by 1 and 2. It follows that

$$\frac{\hat{I}_1 - I_1^{\text{clr}}}{\hat{I}_2 - I_2^{\text{clr}}} = \frac{\int_{p_s}^{p_c} T_1(p,0)\frac{\partial B_1(p)}{\partial p}\,dp}{\int_{p_s}^{p_c} T_2(p,0)\frac{\partial B_2(p)}{\partial p}\,dp}, \tag{7.4.59}$$

where we have set $\varepsilon_1 \cong \varepsilon_2$, a good approximation for wavenumbers close enough together in the 15 μm CO_2 band. The idea of employing the ratio of the cloud signal for two CO_2 channels viewing the same FOV to determine the cloud top pressure appears to have been developed by Smith and Platt (1978).

The left side of Eq. (7.4.59) is determined from the satellite-observed radiances in a given FOV, as well as from the clear-air radiances that can be inferred from analyses of satellite clear radiance observations. The temperature profile is supposed to be retrieved from the channels in the 4.3 and 15 μm CO_2 bands. It follows that the cloud-top pressure p_c, or height, can be inferred numerically. This is the essence of the CO_2 slicing method. Once the cloud-top pressure has been determined, an effective emissivity $\eta\varepsilon$ can be evaluated from the infrared window channel. In the window (let the wavenumber index be 3), we can write

$$\hat{I}_3 = \eta\varepsilon_3 B_3(T_c) + (1 - \eta\varepsilon_3)I_3^{\text{clr}}, \tag{7.4.60a}$$

where $B_3(T_c)$ is the blackbody cloud radiance in the window, which can be determined once the cloud height is given. Thus, the effective emissivity is

$$\eta\varepsilon_3 = \frac{\hat{I}_3 - I_3^{\text{clr}}}{B_3(T_c) - I_3^{\text{clr}}}. \tag{7.4.60b}$$

The CO_2 slicing method is most applicable to high-level cirrus clouds because of the nature of the weighting functions in the 15 μm CO_2 band. Wylie *et al.* (1994) used this method to determine cirrus cloud statistics from NOAA's polar-orbiting High-Resolution Infrared Radiation Sounder (HIRS) multispectral data in terms of cloud cover, height, and effective emissivity. Many processing procedures are required to produce a global map of cloud parameters. Displayed in Fig. 7.20 is the geographical distribution of cirrus clouds in the Northern Hemisphere summer (June, July, August) and winter (December, January, February) (referred to as boreal summer and winter) seasons during a 4-year period, June 1989 through May 1993. The intertropical convergence zone (ITCZ) is a region of more frequent cirrus, shown in the darker bands in the tropics, as are the midlatitude storm belts. The ITCZ moves north in the summer season. The subtropical high-pressure systems are evident in the region of less frequent cirrus cover. Over the Indonesian region, the ITCZ expands in coverage from winter to summer, whereas in the central Pacific Ocean, it shows extension in

(a) December - February
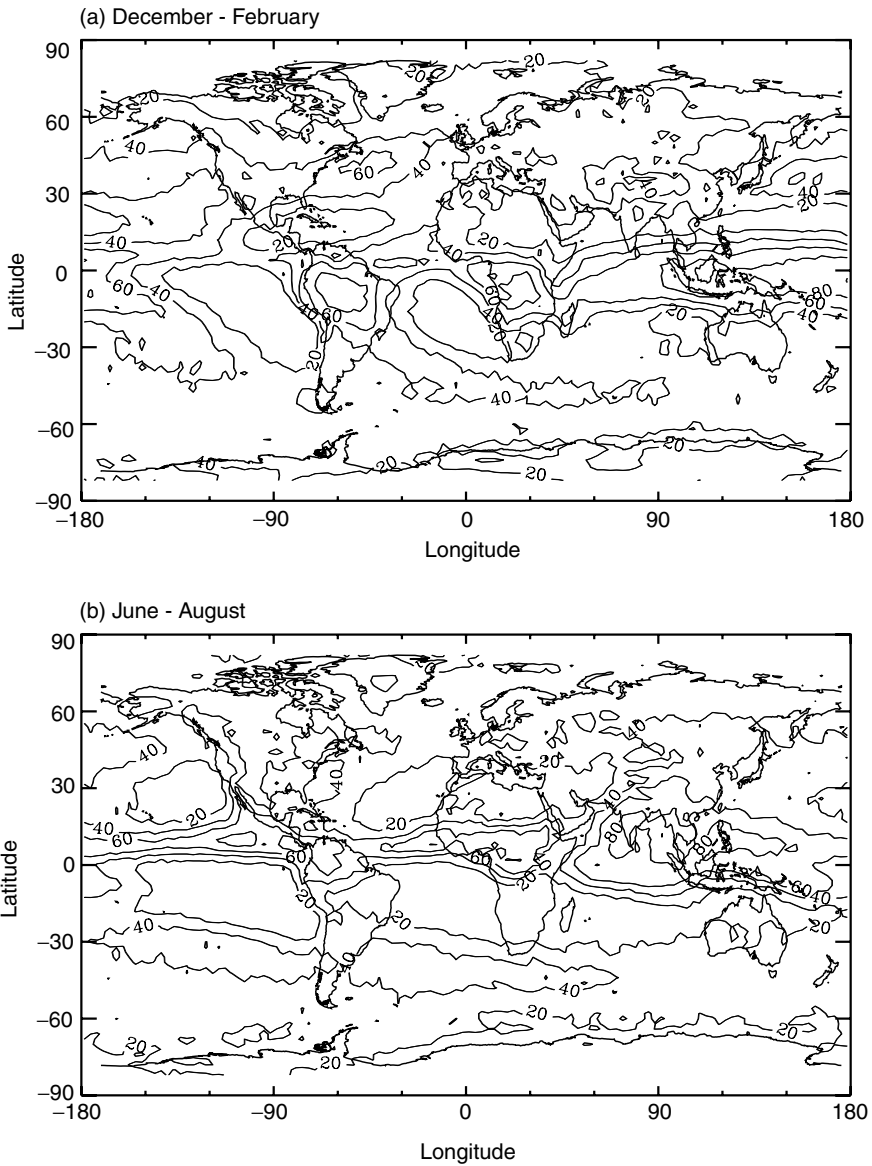

(b) June - August

Figure 7.20   The frequency of clouds (%) above 6 km determined from the HIRS data using the CO_2 slicing technique. The 4-year average results are presented for (a) winter months and (b) summer months (data taken from Wylie *et al.*,1994).

both hemispheres during the winter months (of the Northern Hemisphere). In the Southern Hemisphere, the eastern Pacific Ocean off South America and the eastern Atlantic Ocean off Africa remain relatively free of cirrus clouds throughout the year. Finally, the North American cirrus cloud cover shows little seasonal change. Perhaps the most significant results of the cirrus cloud study based on the CO_2 slicing method are the ubiquitous cirrus occurrence in the tropics (more than 70%), and a noticeable increase in cirrus cover during the 4-year period.

7.4.5.2   EMITTED RADIANCE FOR CLOUD COVER

Many attempts have been made to classify the global distribution of clouds based on the emitted IR radiation in the 10 μm window (plus the reflected visible radiation during daytime). In general, the cloud tops are colder than the surfaces and so the emitted cloud radiances are smaller than the emitted clear radiances. Thus, it is practical to set various types of thresholds to distinguish between clear and cloudy conditions and to obtain cloud cover information. The classification of cloudy pixels by measured radiances is a complex decision-making process based on computer codes. The best example is the International Satellite Cloud Climatology Program (ISCCP), which is a project of the World Meteorological Organization developed in the 1980s (Schiffer and Rossow, 1983; Rossow and Schiffer, 1999). Its goal is to collect global visible and 11-μm data from polar and geostationary satellites and to process them into a cloud climatology.

An accurate global cloud climatology is essential to the development of physically based climate models; it can serve both as a source of input data for models that prescribe cloudiness and as a means of validating models that predict cloud formation. The ISCCP cloud products have also been used by researchers to understand the relationship of large-scale cloud patterns and dynamic processes in the atmosphere and the oceans. Zonally averaged cloud cover for January, July, and annual conditions derived from ISCCP are illustrated in Fig. 7.21. The equatorial maximum associated with the ITCZ lies between 0 and 10°N in July and 0 and 10°S in January. The minima, associated with subtropical anticyclones and desert areas, occur in both hemispheres at about 15° in the winter and at about 25° in the summer. The cloud amount tends to decrease poleward of 60°S in both January and July, but increases in January poleward of 60°N. The most cloudy latitude band is 60–70°S and in July, the area of cloudiness at 80–90°N is largely associated with Arctic stratus.

7.4.5.3   RETRIEVAL OF CIRRUS CLOUD OPTICAL DEPTH AND TEMPERATURE

As shown in Subsection 7.4.5.1 and presented in Section 5.1, cirrus clouds are globally distributed and have a high percentage of coverage. They are primarily present in the upper troposphere and lower stratosphere and are exclusively composed of nonspherical ice crystals. These clouds are normally transparent in the thermal IR wavelengths, particularly in the 3.7 and 10 μm windows, and consequently cannot be treated as blackbodies in radiative transfer in conjunction with remote sensing applications. In Section 7.3.5, we discussed the principles for the detection and determination of cirrus cloud optical depth and mean effective ice crystal size from
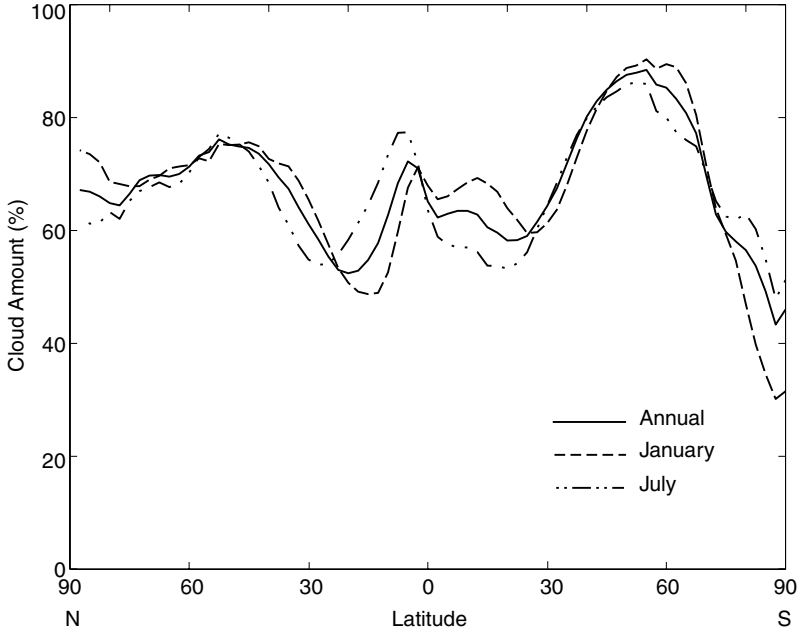
Figure 7.21 Meridional profiles of zonally averaged cloud amount for January, July, and annual conditions based on results derived from the International Satellite Cloud Climatology Program (ISCCP) data over a period from 1983 to 1994 (data available from William Rossow of the ISCCP office).

reflected sunlight. In the following, we introduce the principle of the retrieval of cirrus cloud parameters utilizing IR techniques.

Consider the upwelling radiance I at TOA in cirrus cloudy atmospheres. It is contributed by the radiance emitted from the cloud and the radiance transmitted through the cloud from the atmosphere and surface below. By selecting two appropriate window wavelengths, we have

$$I_i = (1 - \varepsilon_i)I_{ai} + \varepsilon_i B_i(T_c), \qquad i = 1, 2, \tag{7.4.61}$$

where I_{ai} are the upwelling radiances reaching the cloud base for the two wavelengths; ε_i are the cloud IR emissivities; T_c is the mean effective cloud temperature; and B_i are the Planck radiances. The objective of retrieval is to infer ε and T_c from two radiance measurements. However, there are a number of unknown variables involved in this basic equation that require parameterization.

From radiative transfer calculations of IR wavelengths, it is appropriate to approximate cloud emissivity in terms of visible optical depth τ in the form

$$\varepsilon_i \cong 1 - e^{-k_i \tau}, \tag{7.4.62}$$

where k_i represents the effective extinction coefficient. Thus, ε_1 and ε_2 can be correlated by introducing the ratio k_2/k_1, which is a function of the ice-crystal size distribution that needs to be prescribed prior to the retrieval exercise. The Planck

functions of two wavelengths can also be correlated by polynomials as follows:

$$B_1(T_c) = \sum_{n=0}^{3} a_n [B_2(T_c)]^n, \qquad (7.4.63)$$

where a_n are fitting coefficients. Furthermore, values of the upwelling radiances reaching the cloud base must also be known. This can be accomplished by searching the clear pixels close to the cloud. With all the preceding considerations, radiance measurements in two wavelengths can be used to determine two variables: cloud visible optical depth and temperature, which may be related to ice crystal size.

The two channel IR technique requires that the optical properties of cirrus vary substantially between the two wavelengths. Huang and Liou (1984) developed a method to infer cirrus cloud optical depth and temperature based on AVHRR 3.7 and 10.9 μm channels. Inoue (1985) used the AVHRR radiance difference between 11 and 12 μm to determine the IR emissivity of cirrus clouds by assuming an implicit mean particle size. Liou *et al.* (1990b) used 6.5 and 11 μm radiometers to infer the temperature and optical depth of tropical cirrus. Cloud microphysics observations have shown that ice-crystal size distribution is correlated with cloud temperature. It is feasible, therefore, to estimate the mean effective ice crystal size once the cloud temperature is determined from satellite data (Ou *et al.,* 1995). Application of the 3.7 μm channel to daytime data requires the removal of the solar reflection component. A combination of the emitted 10 μm radiance and the reflected visible intensity has also been used to infer cirrus optical depth and temperature by means of a correlation between the IR emissivity and visible optical depth (Minnis *et al.,* 1993).

Independent validation of any remote-sensing algorithm for a variety of atmospheric conditions is essential to ensure its success. In the case of clouds, validation of retrieved ice-crystal size, which is an integrated value in the vertical, requires *in situ* aircraft measurements that must be collocated and coincident with the radiometric pixel observations. In recent years, airborne optical probes and replicator systems have been well developed for the collection of ice particles. Since aircraft observations are generally limited in time and space, especially in the vertical direction, validation of satellite-retrieved cloud particle sizing is a subject requiring considerable research and development. Cloud optical depth is a product of cloud thickness and the extinction coefficient. Cloud thickness can be inferred precisely from lidar backscattering for single cirrus and/or from radiosondes. The extinction coefficient requires light-scattering calculations involving ice-crystal size distributions. A consistent and reliable validation program for the remote sensing of clouds is evidently an involved and challenging task.

7.4.5.4　Information Content in Infrared Line Spectrum

In the analysis of the satellite Infrared Radiation Interferometer Spectrometer (IRIS) data, Prabhakara *et al.* (1993) have illustrated that thin cirrus in the tropics can be identified in the 8–12 μm window region. The IRIS instrument was on

board Nimbus 3 (Conrath *et al.,* 1970) and 4 (Kunde *et al.,* 1974) and for the first time provided the infrared emission of the atmosphere from about 400 to 1600 cm^{-1} with a 5 cm^{-1} spectral resolution (see also Section 4.1). Although the interferometer spectrometer experiment was not followed in the United States satellite program, three Fourier spectrometers in the spectral range 400–1600 cm^{-1} were included in the European METEOR satellites in the late 1970s. In the analysis of the emission spectra measured in clear and cirrus cloudy atmospheres, Spänkuch and Döhler (1985) have found that the presence of cirrus clouds significantly reduces the upwelling radiances in the entire spectral region, except in the center of the CO_2 15 μm band.

Smith *et al.* (1995) have developed a high spectral resolution infrared spectrometer, referred to as HIS, intended for satellite applications. This instrument was cited in Section 7.4.3 in the discussion of temperature retrievals. Sufficient information about cirrus clouds appears in the HIS spectrum. More recently, Smith *et al.* (1998) have displayed an interesting spectrum for a case involving a cold cirrus that was particularly evident in the 800–1000 cm^{-1} window region, which was presented in Fig. 4.12. As discussed in Section 4.6.1, clouds composed of water droplets such as low clouds or thin clouds containing large ice crystals behave as blackbodies or near blackbodies with little variation in the 10 μm window. However, thin cirrus, which are frequently subvisual, contain small ice crystals with maximum dimensions ranging from about 5 to 20 μm. These clouds have features in the 10 μm window associated with the absorption coefficients of ice crystals that can be used for their identification, as revealed in the extinction and single-scattering albedo spectra illustrated in Fig. 5.24. The development of verifiable schemes for the retrieval of the composition and structure of thin cirrus based on the IR line spectrum would be a subject of practical importance for climate studies.

7.4.6   Remote Sensing of Infrared Cooling Rate and Surface Flux

Infrared flux exchanges in the atmosphere and the atmospheric cooling produced by these exchanges are significant energy sources in the dynamic and thermodynamic processes of the atmosphere. In the troposphere under clear conditions, IR cooling is associated with absorption and emission of water vapor molecules. In particular, this cooling is primarily produced by the H_2O rotational band and H_2O continuum (near the surface). In the middle atmosphere, cooling is largely produced by the CO_2 15 μm band and, to a lesser degree, by the O_3 9.6 μm band, as explained in Section 4.5. The input data for IR calculations in clear atmospheres are basically temperature and water vapor profiles. For middle-atmosphere applications, other absorbing gaseous profiles are also needed. If these profiles can be reliably determined from the radiance data derived from satellite measurements, IR fluxes and cooling rates can be computed using radiative transfer methodology. Radiation algorithms for cooling rate calculations usually require very large amounts of computer time, and substantial discrepancies occur between different algorithms,

even with the same input data. Direct measurement of IR fluxes and cooling rates from space could have, therefore, important advantages. In the following, we present the general principles for the determination of cooling-rate profiles and surface IR fluxes.

Consider the IR cooling rate defined in Eq. (4.7.1) and rewrite this equation in the form

$$\frac{dF(z)}{dz} = -\rho C_p \dot{T}(z),	(7.4.64)$$

where $\dot{T} = (\partial T / \partial t)_{ir}$, denoting the cooling rate for a spectral band Δv, ρ is the air density, and C_p is the specific heat at constant pressure. There is no obvious relationship between atmospheric cooling rates and radiances at TOA. However, a direct link between the two must exist in view of the fact that both are related to temperature and specific gaseous profiles. As demonstrated in Section 7.4.3, the retrieval of the profile of any physical parameter requires a set of weighting functions that adequately cover the atmosphere. Thus, we may consider the following weighting function in the z-coordinate:

$$K_j(z) = \rho C_p T_j[\xi(z)/\mu],	(7.4.65)$$

where the transmittance for a spectral subband (or channel) Δv_j corresponding to an absorber path length $\xi(z)$ is defined by

$$T_j(\xi/\mu) = \int_{\Delta v_j} e^{-k_v \xi/\mu} \frac{dv}{\Delta v_j} = \int_0^1 e^{-k(g)\xi/\mu} dg.	(7.4.66)$$

The correlated k-distribution method (Section 4.3) can be used to determine the absorption coefficients. It should be noted that the spectral band is related to the spectral subband by $\Delta v = \sum_j \Delta v_j$.

A convolution of the cooling-rate profile and weighting function defined in Eq. (7.4.65) leads to

$$\int_0^{z_\infty} \dot{T}(z) K_j(z) \, dz = -\int_0^{z_\infty} T_j[\xi(z)/\mu] \frac{dF(z)}{dz} \, dz.	(7.4.67)$$

In reference to Eqs. (4.2.10a,b), the spectral upward and downward fluxes in the optical-depth (or height) domain may be written in the path-length domain in the forms

$$F^\uparrow(\xi) = \pi B(\xi_*) T^f(\xi_* - \xi) - \int_\xi^{\xi_*} \pi B(\xi') \frac{d}{d\xi'} T^f(\xi' - \xi) \, d\xi',	(7.4.68a)$$

$$F^\downarrow(\xi) = \int_0^\xi \pi B(\xi') \frac{d}{d\xi'} T^f(\xi - \xi') \, d\xi',	(7.4.68b)$$

where ξ is the absorber path length in which $\xi = 0$ at TOA and $\xi = \xi_*$ at the surface, and the spectral interval subscript is omitted for simplicity of presentation.

The spectral diffuse transmittance is defined in Eq. (4.2.9) and can be written in the form

$$T^f(\xi) = 2 \int_0^1 T(\xi/\mu)\mu \, d\mu, \tag{7.4.68c}$$

where $T(\xi/\mu)$ is the spectral transmittance. The net flux divergence is then given by

$$\frac{dF(\xi)}{d\xi} = \frac{d}{d\xi}[F^\uparrow(\xi) - F^\downarrow(\xi)]$$

$$= 2\pi B(\xi_*) \int_0^1 \frac{\partial}{\partial\xi} T[(\xi_* - \xi)/\mu]\mu \, d\mu$$

$$-2\pi \int_0^1 \mu d\mu \left\{ \int_\xi^{\xi_*} B(\xi') \frac{\partial}{\partial\xi} \left(\frac{d}{d\xi'} T[(\xi' - \xi)/\mu] \right) d\xi' \right.$$

$$\left. -B(\xi)\frac{d}{d\xi'} T[(\xi' - \xi)/\mu] \Big|_{\xi'=\xi} \right\}$$

$$-2\pi \int_0^1 \mu d\mu \left\{ \int_0^\xi B(\xi') \frac{\partial}{\partial\xi} \left(\frac{d}{d\xi'} T[(\xi - \xi')/\mu] \right) d\xi' \right.$$

$$\left. +B(\xi)\frac{d}{d\xi'} T[(\xi - \xi')/\mu] \Big|_{\xi'=\xi} \right\}. \tag{7.4.69a}$$

The spectral transmittance defined in the g-domain as shown in Eq. (7.4.66) is a linear operator involving the exponential function. For the purpose of this analysis, it suffices to let $T(\xi/\mu) = \exp(-k\xi/\mu)$. Thus, using this expression the net flux divergence after differential operations can then be expressed by

$$\frac{dF(\xi)}{d\xi} = 2\pi k B(\xi_*) \int_0^1 e^{-k(\xi_*-\xi)/\mu} \, d\mu + 2\pi k^2 \int_\xi^{\xi_*} B(\xi') \int_0^1 e^{-k(\xi'-\xi)/\mu} \frac{d\mu}{\mu} d\xi'$$

$$+ 2\pi k^2 \int_0^\xi B(\xi') \int_0^1 e^{-k(\xi-\xi')/\mu} \frac{d\mu}{\mu} d\xi' - 4\pi k B(\xi). \tag{7.4.69b}$$

The spectral subband (channel) transmittance associated with the kernel function may also be written in a simple exponential function, $T_j(\xi/\mu) = \exp(-k_j\xi/\mu)$. It follows that

$$\int_0^{\xi_*} T_j(\xi/\mu) \frac{dF(\xi)}{d\xi} \, d\xi = \int_0^{\xi_*} e^{-k_j\xi/\mu} \frac{dF(\xi)}{d\xi} \, d\xi. \tag{7.4.70}$$

On substituting Eq. (7.4.69b) into Eq. (7.4.70), we first find that the first term on the right-hand side of Eq. (7.4.69b) approaches zero, when we set $\xi_* \to \infty$. Second,

the fourth term

$$\vartheta_4 = -4\pi k \int_0^{\xi_*} B(\xi)e^{-k_j\xi/\mu}\,d\xi = -4\pi \chi_j I_j(\mu), \qquad (7.4.71a)$$

based on the definition of the emergent channel radiance, where the coefficient $\chi_j = (k/k_j)\mu$. Here, we have omitted the surface term in this remote sounding application, although it could be included in the analysis. The solutions for the second and third terms require intricate mathematical analyses involving the interchange of the order of integrations and the use of the mean value theorem (Liou and Xue, 1988). The final results are, respectively,

$$\vartheta_2 = 2\pi \chi_j \ln(1 - 1/\chi_j)[\bar{\mu}I(\bar{\mu}) - \chi_j I_j(\mu)], \qquad (7.4.71b)$$

$$\vartheta_3 = 2\pi \chi_j^2 \ln(1 + 1/\chi_j)I_j(\mu), \qquad (7.4.71c)$$

where the beam-flux parameter determined from the mean value theorem using the isothermal atmosphere approximation is given by

$$\bar{\mu} = [1 + \chi_j \ln(1 - 1/\chi_j)]/\ln(1 - 1/\chi_j). \qquad (7.4.71d)$$

In practice, the spectral and channel transmittances in the g-space may be written in summation form as follows:

$$T(\xi/\mu) = \sum_m e^{-k_m\xi/\mu}\Delta g_m, \qquad (7.4.72a)$$

$$T_j(\xi/\mu) = \sum_n e^{-k_n\xi/\mu}\Delta g_n. \qquad (7.4.72b)$$

Since the summation operators are linear, we may carry out the preceding analyses employing Eqs. (7.4.72a,b) with the final results involving two double summations for all the terms in Eq. (7.4.70). Consequently, we may write

$$\int_0^{\xi_*} T_j(\xi/\mu) \frac{dF(\xi)}{d\xi}\,d\xi = I(\bar{\mu})\alpha + I_j(\mu)\beta, \qquad (7.4.73a)$$

where $I(\bar{\mu})$ is the radiance for the spectral band at a mean angle $\cos^{-1}\bar{\mu}$, $I_j(\mu)$ is the channel radiance at an emergent angle, $\cos^{-1}\mu$, and α and β are coefficients associated with the absorption coefficients that can be determined exactly from numerical means. The value of $\bar{\mu}$ varies from about 0.5 to 0.6. In this manner, the net flux divergence is transformed into spectral and channel radiances via a convolution with the channel transmittance.

Combining Eqs. (7.4.67) and (7.4.73a), we obtain the basic Fredholm equation of the first kind for the remote sounding of cooling rate profiles from space:

$$I(\bar{\mu})\alpha + I_j(\mu)\beta = -\int_0^{z_\infty} \dot{T}(z)K_j(z)\,dz. \qquad (7.4.73b)$$

Two sets of measurements are needed to drive the spectral cooling rate profiles: spectral radiance $I(\bar{\mu})$ and channel radiance $I_j(\mu)$, which can both be measured at
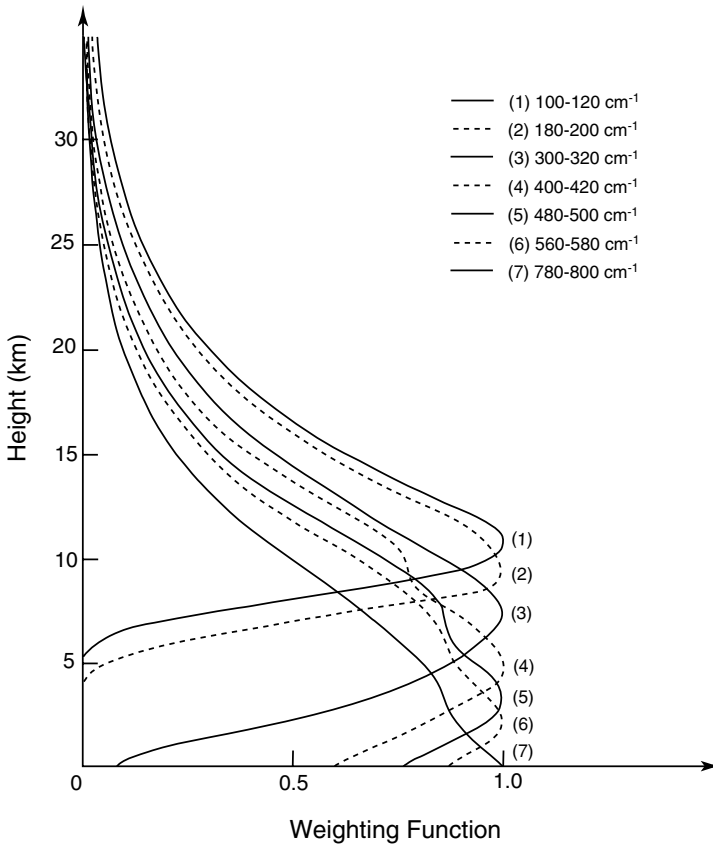
Figure 7.22 Normalized weighting functions for atmospheric cooling rate retrieval in the H_2O rotational band (20–800 cm^{-1}). The weighting functions presented here are products of air density and channel transmittances for a 20 cm^{-1} interval using standard atmospheric temperature and water vapor profiles (data taken from Liou, 1992).

an emergent angle, $\cos^{-1} \bar{\mu}$. We must now examine the required weighting functions. A number of weighting functions based on Eq. (7.4.65) have been calculated in the H_2O rotational band for a 20 cm^{-1} interval using a line-by-line program. Illustrated in Fig. 7.22 are seven weighting functions whose peaks are spaced within $\sim$2 km in height. The four uppermost and three lowermost channels could be used to retrieve cooling rates for spectral intervals of 20–500 cm^{-1} and 500–800 cm^{-1}, respectively. The preceding theory would be ideal for the retrieval of the cooling rate produced by CO_2 in the middle atmosphere, since clouds would have little effect on the upwelling radiances at TOA. However, appropriate weighing functions must be determined in the stratosphere and lower mesosphere for practical applications.

The determination of surface radiative fluxes from available satellite radiance data has been a subject of considerable interest in recent years in view of the important role that surface–atmosphere interactions play in climate (Section 8.2.5). A direct

observational study of surface IR fluxes could be conducted using the following approach. Based on the definition of cooling rate in Eq. (7.4.64), we may perform an integration of this equation from the surface to TOA to obtain

$$F(0) = F(z_\infty) + \int_0^{z_\infty} \rho C_p \dot{T}(z)\, dz. \qquad (7.4.74)$$

The broadband IR flux at TOA, $F(z_\infty)$, has been routinely derived from satellite measurements (Section 8.2.2). Thus, if the cooling rate profile $\dot{T}(z)$ is retrievable from radiance observations, we may estimate the surface radiative flux $F(0)$ based solely on measurements from space. Furthermore, we note that if the contributions due to O_3, CO_2, and H_2O–CO_2 overlap are omitted, the total cooling would be accurate within $\sim$4 % depending on the temperature profile. Thus, to a good approximation, total atmospheric cooling may be obtained by measuring the cooling profile produced by water vapor.

The history of infrared sounding from space, as discussed in this section, has been characterized by the slow evolution of retrieval methodologies and of the selection of sounding channels. To be successful in cooling-rate retrieval, many additional aspects of practical issues such as cloud problems and infrared technology will need to be examined. The HIS data presented in Subsection 7.4.5.4 could be useful for the exploration of IR cooling rate retrieval, particularly if the spectrum coverage is extended to the rotational band of water vapor. The HIS instrument is capable of scanning from space and could provide the needed spectral radiances for conversion to fluxes.

7.5   Remote Sensing Using Emitted Microwave Radiation

7.5.1   Microwave Spectrum and Microwave Radiative Transfer

In the microwave region, only water vapor and molecular oxygen exhibit significant absorption lines. It is customary to use the frequency unit GHz in the discussion of microwave radiative transfer. Note that 1 GHz = 10^9 cycles/sec, and 1 cm = 30 GHz. Below 40 GHz only the weakly absorbing pressure-broadened 22.235 GHz water vapor line is dominant. This resonance absorption line arises from transitions between nuclear spin rotational states. At about 31.4 GHz, air is relatively transparent, which is the window between the resonance water vapor line. The oxygen molecule has a magnetic dipole moment arising from the combined spins of two impaired electrons in its electronic ground state. Changes in the orientation of the electronic spin relative to the orientation of the molecular rotation produce a strong band of magnetic dipole transitions near 60 GHz and a single transition at 118.75 GHz. For frequencies greater than 120 GHz, water vapor absorption again becomes dominant because of the strongly absorbing line at 183 GHz. Figure 7.23 illustrates vertical atmospheric transmittance as a function of frequency and wavelength for a standard atmosphere, clearly identifying the aforementioned absorption lines.
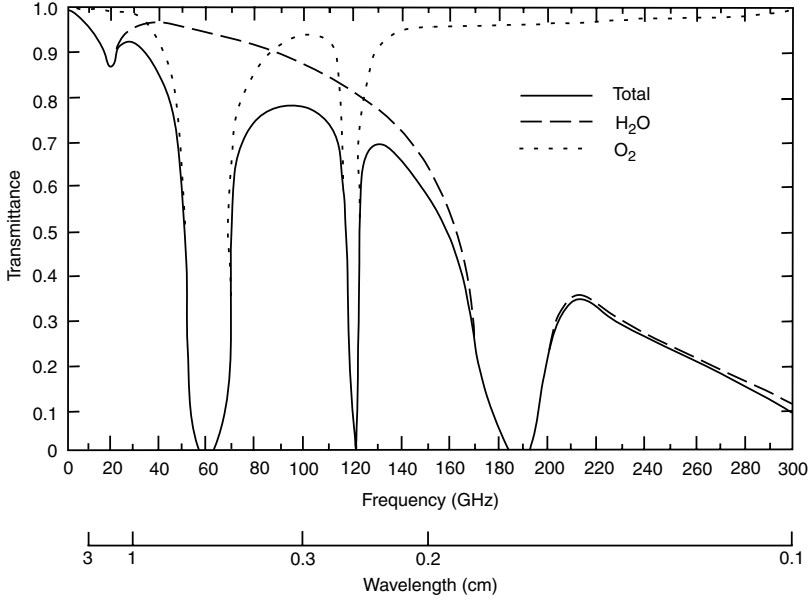
Figure 7.23 Demonstrative atmospheric transmittances (total, H_2O, and O_2) as a function of frequency and wavelength in the microwave region.

In view of the size of water droplets ($\sim 10~\mu$m) and ice crystals ($\sim 100~\mu$m) in the atmosphere, their effects on the scattering of microwaves (~ 1 cm) are generally small. Thus, we may, as a good approximation, neglect the scattering contribution in the discussion of microwave radiative transfer. In reference to Section 7.4.1, the solution of the radiative transfer equation for a nonscattering atmosphere in local thermodynamic equilibrium is given by

$$I_{\tilde{v}}(0) = I_{\tilde{v}}(p_s)T_{\tilde{v}}(p_s, 0) + \int_{p_s}^{0} B_{\tilde{v}}[T(p)] \frac{\partial T_{\tilde{v}}(p, 0)}{\partial p}\, dp, \qquad (7.5.1)$$

where $\tilde{v}$ denotes the frequency, $I_{\tilde{v}}(p_s)$ represents the radiance contribution from the surface, and the transmittance, $T_{\tilde{v}}(p, 0)$, is expressed with respect to TOA. Emissivity in the microwave region is normally less than unity, so there is a significant reflection contribution from the surface. The radiance emitted from the surface is given by

$$I_{\tilde{v}}(p_s) = \varepsilon_{\tilde{v}} B_{\tilde{v}}(T_s) + (1 - \varepsilon_{\tilde{v}}) \int_{0}^{p_s} B_{\tilde{v}}[T(p)] \frac{\partial T_{\tilde{v}}(p_s, p)}{\partial p}\, dp, \qquad (7.5.2)$$

where the first term on the right-hand side denotes the surface emission contribution and the second term represents the emission contribution from the entire atmosphere to the surface that is reflected back to the atmosphere at the same frequency. The transmittance, $T_{\tilde{v}}(p_s, p)$, is now expressed with respect to the surface.

Inserting the lower boundary condition defined in Eq. (7.5.2), the upwelling radiance can now be expressed as

$$I_{\tilde{\nu}} = \varepsilon_{\tilde{\nu}} B_{\tilde{\nu}}(T_s) T_{\tilde{\nu}}(p_s, 0) + (1 - \varepsilon_{\tilde{\nu}}) T_{\tilde{\nu}}(p_s, 0) \int_0^{p_s} B_{\tilde{\nu}}[T(p)] \frac{\partial T_{\tilde{\nu}}(p_s, p)}{\partial p} \, dp$$

$$+ \int_{p_s}^0 B_{\tilde{\nu}}[T(p)] \frac{\partial T_{\tilde{\nu}}(p, 0)}{\partial p} \, dp. \tag{7.5.3}$$

The Planck function in the frequency domain is given by

$$B_{\tilde{\nu}}(T) = 2h\tilde{\nu}^3 / \left[c^2 \left(e^{h\tilde{\nu}/KT} - 1 \right) \right]. \tag{7.5.4a}$$

In the microwave region, $h\tilde{\nu}/KT \ll 1$, the Planck function can be approximated by

$$B_{\tilde{\nu}}(T) \cong (2K\tilde{\nu}^2/c^2)T. \tag{7.5.4b}$$

Thus, Planck radiance is linearly proportional to temperature, referred to as the *Rayleigh–Jeans law* discussed in Section 1.2. Analogous to the above approximation, we can define an equivalent brightness temperature T_B such that

$$I_{\tilde{\nu}} = (2K\tilde{\nu}^2/c^2)T_B(\tilde{\nu}). \tag{7.5.5}$$

Substituting Eqs. (7.5.4b) and (7.5.5) into Eq. (7.5.3), the solution of microwave radiative transfer may now be written in terms of temperature as follows:

$$T_B(\tilde{\nu}) = \varepsilon_{\tilde{\nu}} T_s T_{\tilde{\nu}}(p_s, 0) + (1 - \varepsilon_{\tilde{\nu}}) T_{\tilde{\nu}}(p_s, 0) \int_0^{p_s} T(p) \frac{\partial T_{\tilde{\nu}}(p_s, p)}{\partial p} \, dp$$

$$+ \int_{p_s}^0 T(p) \frac{\partial T_{\tilde{\nu}}(p, 0)}{\partial p} \, dp. \tag{7.5.6}$$

The contribution of each term to the brightness temperature at TOA is illustrated in Fig. 7.24. The first, second, and third terms represent the surface emission contribution, the reflection contribution from the surface into the atmosphere, and the atmospheric emission contribution, respectively.

The transmittance used for satellite remote sensing is generally expressed with respect to TOA; i.e., $T_{\tilde{\nu}}(p) = T_{\tilde{\nu}}(p, 0)$. Thus, for computational purposes, it is desirable to express $T_{\tilde{\nu}}(p_s, p)$ in terms of $T_{\tilde{\nu}}(p, 0)$. For monochromatic frequencies, transmittance is an exponential function of optical depth [see Eq. (7.4.4)]. Hence, we can write

$$T_{\tilde{\nu}}(p_s, p) = \exp\left[-\frac{1}{g} \int_p^{p_s} k_{\tilde{\nu}}(p')q(p') \, dp' \right]$$

$$= \exp\left[-\frac{1}{g} \int_0^{p_s} k_{\tilde{\nu}}(p')q(p') \, dp' + \frac{1}{g} \int_0^p k_{\tilde{\nu}}(p')q(p') \, dp' \right]$$

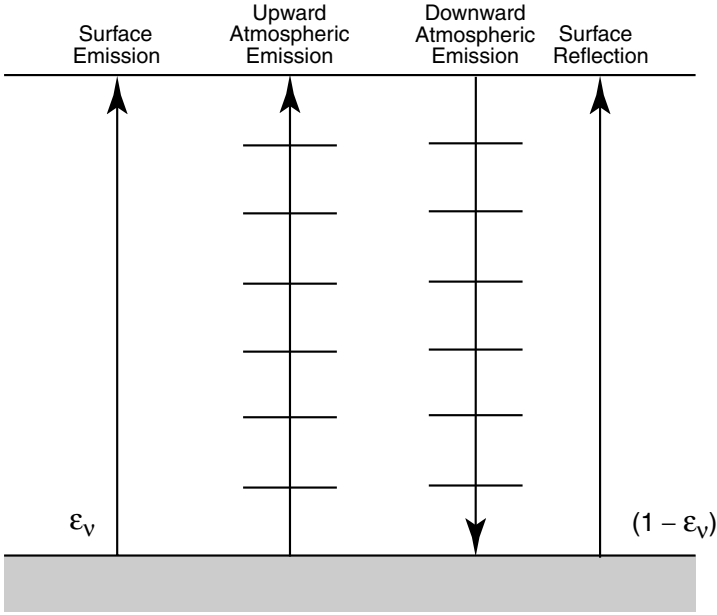$$= T_{\tilde{\nu}}(p_s, 0)/T_{\tilde{\nu}}(p, 0), \tag{7.5.7}$$

Figure 7.24   Contributions of brightness temperature at the top of a clear atmosphere, represented by the terms in Eq. (7.5.6), including surface emission and reflection, and atmospheric contributions.

where $T_{\tilde{\nu}}(p_s, 0)$, the transmittance of the entire atmosphere, is a constant value. Thus,

$$\frac{\partial T_{\tilde{\nu}}(p_s, p)}{\partial p} = -\frac{T_{\tilde{\nu}}(p_s, 0)}{[T_{\tilde{\nu}}(p, 0)]^2} \frac{\partial T_{\tilde{\nu}}(p, 0)}{\partial p}. \tag{7.5.8}$$

Inserting Eq. (7.5.8) into Eq. (7.5.6), rearranging terms, and letting $T_{\tilde{\nu}}(p, 0) = T_{\tilde{\nu}}(p)$, we have

$$T_B(\tilde{\nu}) = \varepsilon_{\tilde{\nu}} T_s T_{\tilde{\nu}}(p_s) + \int_{p_s}^{0} J_{\tilde{\nu}}(p) \frac{\partial T_{\tilde{\nu}}(p)}{\partial p} \, dp, \tag{7.5.9}$$

where the atmospheric source term is given by

$$J_{\tilde{\nu}}(p) = \left\{ 1 + (1 - \varepsilon_{\tilde{\nu}})[T_{\tilde{\nu}}(p_s)/T_{\tilde{\nu}}(p)]^2 \right\} T(p). \tag{7.5.10}$$

In microwave sounding, transmittances are computed by including the antenna gain characteristics.

The use of microwaves for atmospheric sounding from a satellite platform differs from that of IR techniques in the consideration of surface emissivity. The surface emissivity appearing in the first term of Eq. (7.5.6) has a substantial effect on the brightness temperature value. In the microwave spectrum, emissivity values of the earth's surface vary over a considerable range, from about 0.4 to 1.0. Over land, emissivity depends on the moisture content of the soil. The wetting of a soil surface results in a rapid decrease in emissivity. The emissivity of dry soil is on the order
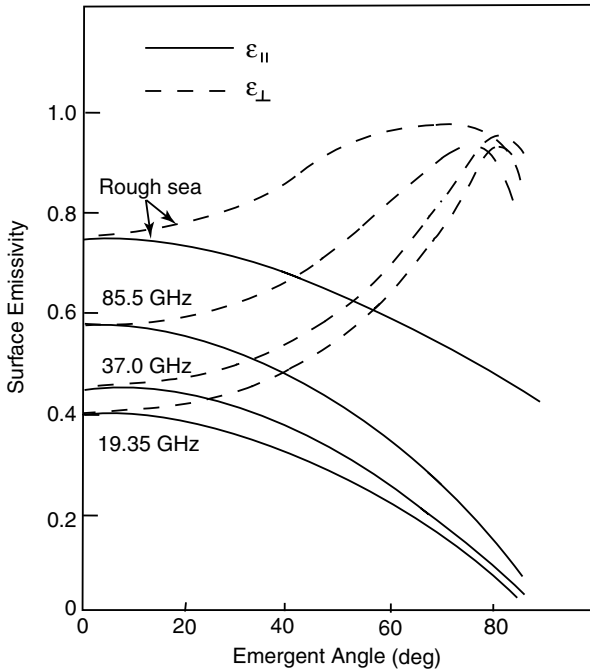
Figure 7.25 Emissivities of calm and rough ocean surfaces for a number of microwave frequencies. The solid and dashed curves represent the horizontal $\varepsilon_{\parallel}$ and vertical $\varepsilon_{\perp}$ polarization components, respectively (data taken from Huang and Liou, 1983).

of 0.95 to 0.97, whereas for wet bare soil it is about 0.80 to 0.90, depending on the frequency. The emissivity of the sea surface typically ranges between 0.4 and 0.6, depending upon such variables as salinity, sea ice, surface roughness, and sea foam. In addition, there is a frequency dependence with higher frequencies displaying higher emissivity values.

Emission from the oceans is polarized. For a calm ocean surface, we can apply the Fresnel reflection formula (Section 5.3.2) to compute the vertical and horizontal emissivity components using the real and imaginary refractive indices for pure water. Shown in Fig. 7.25 are the vertically ($\varepsilon_{\perp}$) and horizontally ($\varepsilon_{\parallel}$) polarized emissivities of calm ocean surfaces for 19.35, 37, and 85.5 GHz. These emissivities increase with increasing frequency. The results for rough sea were derived from empirical fitting to a limited set of observations and are applicable to 37 and 85.5 GHz. Substantial differences between the two components are shown for large emergent angles.

Equation (7.5.1) does not include the scattering and polarization properties of precipitating particles. We may approach the fundamental microwave radiative transfer by incorporating the multiple scattering and emission terms, as presented in Chapter 6. Emission from a homogeneous earth surface is either isotropic (unpolarized land), or zenith-angle dependent (polarized ocean). Further, under the plane-parallel and horizontally homogeneous assumption, the transfer of microwave radiation can be treated as azimuthally independent. In this case, the analysis of the vertically and

horizontally polarized brightness temperatures is independent of the circular polarization and requires only the P_{11}, P_{12}, P_{21}, and P_{22} elements in the scattering phase matrix (see Section 6.6 for definition). Microwave radiative transfer involving finite and inhomogeneous clouds and precipitation can be solved following the methodology presented in Section 6.7.

7.5.2   Rainfall Rate and Water Vapor Determination from Microwave Emission

One of the important applications of microwave radiative transfer has been the determination of atmospheric liquid water and water vapor amounts, since microwaves see through heavy clouds and precipitation, which are largely opaque in the infrared wavelengths.

Based on Lorenz–Mie scattering calculations for spheres, the radiative properties of clouds and precipitation in the microwave spectrum have the following features: (a) ice particles essentially do not absorb microwave radiation but only scatter it; (b) water and rain droplets absorb and scatter with absorption dominating; (c) scattering and absorption of ice and water both increase with frequency. With respect to the scattering and absorption properties of ice and water, the microwave spectrum can be divided into three regions. Below about 22 GHz, absorption is the main process for microwave radiative transfer. Although scattering also occurs, it is of secondary significance. Around 60 GHz, scattering is more important than absorption. Between 20 and 60 GHz, both scattering and absorption processes are important. The scattering and absorption of ice and water particles depend on their sizes relative to the microwave frequency. For frequencies in the 22 and 31 GHz regions (longer wavelengths), the scattering of ice crystals is negligible so that ice clouds are transparent to these microwave frequencies, making them ideal for the detection of rainfall rates.

In order to derive the liquid water and water vapor amounts, it is necessary to develop parameterization equations in which the liquid water content and water vapor amount are explicitly defined. In reference to Eq. (7.5.6), we perform integration by parts on the two integral terms to obtain

$$T_B(\tilde{\nu}) = \left[T(0) - \int_{p_s}^0 T_{\tilde{\nu}}(p) \frac{\partial T(p)}{\partial p} \, dp \right] - (1 - \varepsilon_{\tilde{\nu}}) T_{\tilde{\nu}}^2(p_s)$$
$$\times \left[T(0) + \frac{1}{T_{\tilde{\nu}}(p_s)} \int_0^{p_s} T_{\tilde{\nu}}(p_s) \frac{\partial T(p)}{\partial p} \, dp \right], \qquad (7.5.11a)$$

where, for simplicity, we use one pressure variable in the argument of the transmittance. Moreover, we define

$$x_{\tilde{\nu}} = \frac{T(0)}{T_s} - \frac{1}{T_s} \int_{p_s}^0 T_{\tilde{\nu}}(p) \frac{\partial T(p)}{\partial p} \, dp$$
$$= 1 + \frac{1}{T_s} \int_{p_s}^0 [1 - T_{\tilde{\nu}}(p)] \frac{\partial T(p)}{\partial p} \, dp, \qquad (7.5.11b)$$

$$y_{\tilde{v}} = \frac{T(0)}{T_s} + 1 - \frac{1}{T_{\tilde{v}}(p_s)T_s} \int_0^{p_s} T_{\tilde{v}}(p) \frac{\partial T(p)}{\partial p} \, dp$$

$$= \frac{1}{T_{\tilde{v}}(p_s)} + \frac{T(0)}{T_s}\left[1 - \frac{1}{T_{\tilde{v}}(p_s)}\right] - \frac{1}{T_{\tilde{v}}(p_s)T_s} \int_0^{p_s} [1 - T_{\tilde{v}}(p)] \frac{\partial T(p)}{\partial p} \, dp.$$

$$(7.5.11c)$$

Hence, Eq. (7.5.11a) can be rewritten as follows:

$$T_B(\tilde{v}) = T_s\left[x_{\tilde{v}} - y_{\tilde{v}} T_{\tilde{v}}^2(p_s)(1 - \varepsilon_{\tilde{v}})\right]. \tag{7.5.12}$$

Upon inspection of the microwave spectrum, we find that below about 40 GHz, the transmittance $T_{\tilde{v}}(p_s) \approx 1$, so that $x_{\tilde{v}} \approx y_{\tilde{v}} \approx 1$. As a result of this simplification, the brightness temperature can be approximated by

$$T_B(\tilde{v}) \cong T_s\left[1 - T_{\tilde{v}}^2(p_s)(1 - \varepsilon_{\tilde{v}})\right]. \tag{7.5.13a}$$

The transmittance for frequencies lower than 40 GHz is mainly due to the absorption of water vapor and liquid water. It may be expressed by

$$T_{\tilde{v}}(p_s) = T_{\tilde{v}}(\text{vapor}) \, T_{\tilde{v}}(\text{liquid}). \tag{7.5.13b}$$

For frequencies lower than about 40 GHz, the transmittance of liquid water can be approximated by

$$T_{\tilde{v}}(\text{liquid}) \cong \exp(-Q/Q_0) \approx 1 - Q/Q_0(\tilde{v}), \tag{7.5.13c}$$

where Q is the liquid water path (g cm^{-2}) and $Q_0(\tilde{v})$ is a constant that depends on the frequency and cloud temperature. In a similar manner, if we select a frequency at about 22 GHz, the water vapor transmittance can be approximated by

$$T_{\tilde{v}}(\text{vapor}) \approx 1 - W/W_0(\tilde{v}), \tag{7.5.13d}$$

where W is the total water vapor path length (g cm^{-2}) and, again, $W_0(\tilde{v})$ is a constant. Inserting these two expressions in Eq. (7.5.13a), and neglecting second-order terms involving Q and W, we obtain

$$T_B(\tilde{v}) \cong \varepsilon_{\tilde{v}} T_s + 2(1 - \varepsilon_{\tilde{v}})T_s(Q/Q_0 + W/W_0). \tag{7.5.14}$$

Assuming that the surface temperature T_s and the surface emissivity $\varepsilon_{\tilde{v}}$ are known parameters, two brightness temperature observations at about 40 and 22 GHz can be used to determine Q and W as follows:

$$Q = q_0 + q_1 T_B(\tilde{v}_1) + q_2 T_B(\tilde{v}_2),$$
$$W = w_0 + w_1 T_B(\tilde{v}_1) + w_2 T_B(\tilde{v}_2), \tag{7.5.15}$$

where w_i and q_i are coefficients related to the frequencies chosen, the surface temperature, the emissivity, and the empirical parameters Q_0 and W_0. They are normally determined statistically from a sample of known brightness temperatures and the liquid water and water vapor amounts in known atmospheric profiles.

The rainfall rate is related to raindrop size distribution, which can be measured at the surface. Based on measurements, Marshall and Palmer (1948) have suggested that droplet size distribution can be fitted by an appropriate negative exponential form given by

$$n(D) = n_0 e^{-\Lambda D}, \tag{7.5.16a}$$

where the raindrop diameter $D = 2a$, a is the radius, and $n(D)dD$ represents the number of droplets per unit volume with the diameter between D and $D + dD$ in units of cm. The slope factor Λ was found to depend only on the rainfall rate R, which is measured in terms of mm hr^{-1} and is given by

$$\Lambda = 41 R^{-0.21}. \tag{7.5.16b}$$

In Eq. (7.5.16a), the intercept parameter $n_0 = 0.08$ cm^{-4}. Thus, once the rainfall rate is given, a Marshall and Palmer size distribution is determined. The liquid water path (LWP, g cm^{-2}) is the product of LWC and cloud thickness, Δz, defined in Eq. (7.3.13b). Using the Marshall and Palmer size distribution, we can show that

$$\text{LWP} = k R^{-0.84}, \tag{7.5.16c}$$

with k a certain coefficient. Thus, LWP is directly related to the rainfall rate.

In the case of pure absorption and emission, the LWP (or Q) is directly connected to the brightness temperature via Eq. (7.5.15). Using the relationship between LWP and the rainfall rate, we have

$$T_B(\tilde{\nu}) \cong b + c R^{0.84}, \tag{7.5.17}$$

where b and c are empirical coefficients to be determined from known atmospheric and surface conditions. The preceding analysis did not account for the scattering contribution of cloud particles, which can be important if their sizes are comparable to or larger than the emission wavelength. In this case, a full radiative transfer solution including scattering contributions should be developed in conjunction with the retrieval of rainfall rates.

The inference of water content and total water vapor amount from Nimbus E Microwave Spectrometer (NEMS) data at 22.235 and 31.4 GHz channels on Nimbus 5 (1972) over the oceans was first reported by Staelin *et al.* (1976) and Grody (1976). The coefficients were obtained by a multidimensional regression analysis based upon computed brightness temperatures with known atmospheric temperature and water vapor profiles derived from radiosondes. Computations including the contribution of clouds and precipitation to the brightness temperature did not include the scattering contribution due to clouds and rain drops. These authors have demonstrated the feasibility of mapping the large-scale features of liquid water and total water vapor patterns from the water vapor (22.235 GHz) and window (31.4 GHz) channel data. Liou and Duff (1979) attempted to derive the liquid water content from Nimbus 6 (1975) Scanning Microwave Spectrometer (SCAMS) data
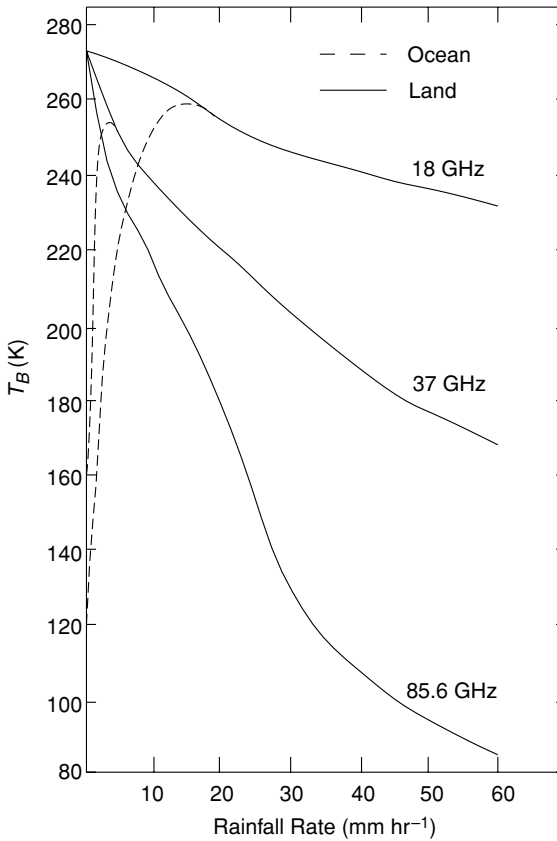
Figure 7.26   Brightness temperature as a function of rainfall rate over the ocean and land for three frequencies (data taken from Spencer *et al.,* 1989).

over land utilizing Eq. (7.5.15). Effects of the scattering and absorption properties of hydrometeors in an inhomogeneous absorbing gaseous atmosphere were included in the calculations along with an empirical means to determine the surface emissivity characteristics.

The mapping of rainfall rates over the oceans using microwave technology from satellites was first proposed by Wilheit and Chang (1977). Effects of the scattering and polarization of precipitation and clouds on the brightness temperatures of microwave window frequencies (19, 37, and 85 GHz) have been reported in Huang and Liou (1983), Mugnai and Smith (1988), and Gasiewski (1993). Shown in Fig. 7.26 is an example of the brightness temperature, T_B, as a function of rainfall rate for three frequencies, 18, 37, and 85.6 GHz, over land and the ocean (Spencer *et al.,* 1989). Over land, T_B decreases with the rainfall rate, an effect that is exacerbated at higher frequencies. Over the ocean, because of lower surface emissivity, T_B initially increases with the rainfall rate.

7.5.3 Temperature Retrieval from Microwave Sounders

The basic concept of inferring atmospheric temperatures from satellite observations of thermal microwave emission in the oxygen spectrum was first developed by Meeks and Lilley (1963), who presented microwave weighting functions for retrieval purposes. The prime advantage of microwave over infrared sounders is that the longer wavelength microwaves are much less influenced by clouds and precipitation. Consequently, microwave sounders can be more effectively utilized when clouds are present.

The first application of microwave techniques for temperature profile determination from an orbiting satellite was the Nimbus 5 Microwave Spectrometer experiment which was designed to evaluate passive microwave techniques for use on operational meteorological satellites. It consisted of three channels centered at frequencies 53.65, 54.90, and 58.80 GHz in the oxygen band (Water *et al.,* 1975). An operational version of the SCAMS, the Microwave Sounding Unit (MSU), was placed on the NOAA series beginning in 1978. It consists of four channels: 50.30, 53.74, 54.96, and 57.95 GHz. The high stability of the MSU instruments has been used to monitor global temperature trends. The approach to recovering temperature profiles using the microwave sounder has generally followed the statistical inversion principle discussed in Subsection 7.4.3.2. Basically, the predictor **D** matrix is derived from *a priori* atmospheric data provided by radiosonde observations.

A more advanced instrument, called the Special Sensor Microwave/Temperature (SSM/T) sounder, was developed as part of the Defense Meteorological Satellite Program (DMSP) aboard the Air Force Block 5D satellite system, first launched in June 1979, and subsequently in 1983, 1987, and 1991. This microwave sensor contains seven channels at 50.5, 53.2, 54.35, 54.9, 58.4, 58.825, and 59.4 GHz. Because of the surface reflectivity effect, the weighting function $K_{\tilde{v}}(p)$ is defined by

$$T_B(\tilde{v}) = \varepsilon_{\tilde{v}} T_s T_{\tilde{v}}(p_s) + \int_{p_s}^{0} T(p) K_{\tilde{v}}(p)\, dp. \qquad (7.5.18a)$$

From Eq. (7.5.6), we have

$$K_{\tilde{v}}(p) = 1 + (1 - \varepsilon_{\tilde{v}}) \left[\frac{T_{\tilde{v}}(p_s)}{T_{\tilde{v}}(p)} \right]^2 \frac{\partial T_{\tilde{v}}(p)}{\partial p}. \qquad (7.5.18b)$$

Displayed in Fig. 7.27a are the weighting functions of seven SSM/T channels for an incident (emergent) angle of $0°$. Absorption due to molecular oxygen and water vapor, along with antenna gain characteristics, were included in the transmittance calculations. Channel 1 is a window channel that responds strongly to the earth's surface characteristics, dense clouds, and rain. It is used to correct the other channels for these background effects. The weighting function peaks of channels 1 to 4 are below about 10 km, and therefore, dense clouds and precipitation would have some effect on the temperature retrieval.

As a result of the surface emissivity's effect on the brightness temperature, it is desirable to remove it in the statistical method of temperature retrieval so that
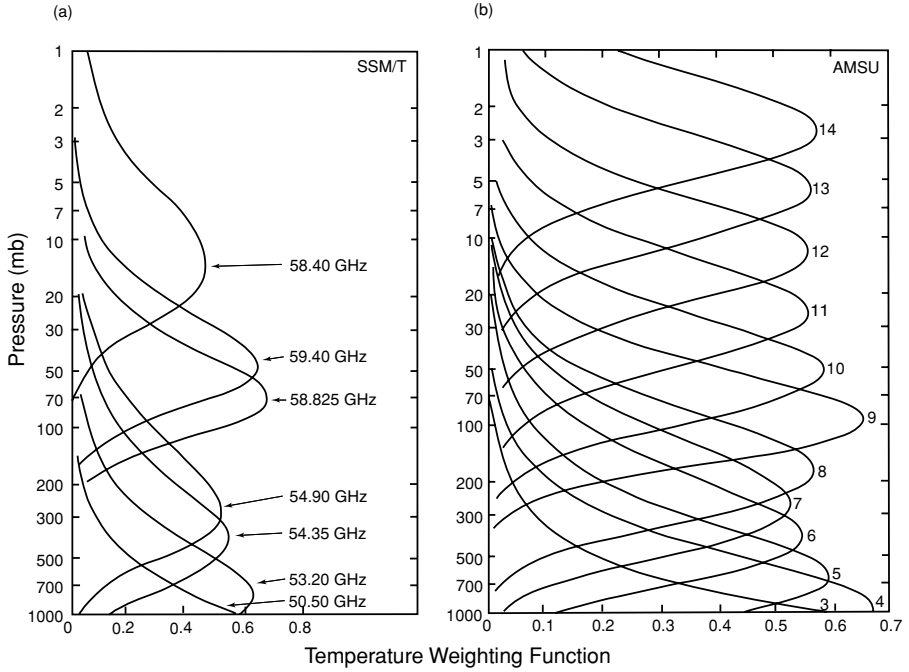
Figure 7.27   (a) Weighting functions at nadir position over land for seven SSM/T channels; (b) weighting functions at nadir viewing over land for 12 AMSU channels (data taken from Grody, 1993).

the predictor matrix **D** can be constructed over all surface conditions (Rigone and Stogryn, 1977). For simplicity of analysis, we define

$$T_d(\tilde{v}) = \int_0^{p_s} T(p)\frac{\partial T_{\tilde{v}}(p)}{\partial p}\, dp,$$

$$T_u(\tilde{v}) = \int_{p_s}^0 T(p)\frac{\partial T_{\tilde{v}}(p)}{\partial p}\, dp, \qquad (7.5.19a)$$

so that Eq. (7.5.6) can be written in the form

$$T_B(\tilde{v}) = \varepsilon_{\tilde{v}} T_s T_{\tilde{v}}(p_s)[1 - T_d(\tilde{v})/T_s] + T_a(\tilde{v}), \qquad (7.5.19b)$$

where

$$T_a(\tilde{v}) = T_u(\tilde{v}) + T_d(\tilde{v})T_{\tilde{v}}(p_s). \qquad (7.5.19c)$$

The second term on the right-hand side of Eq. (7.5.19b) denotes the contribution to the brightness temperature caused solely by the atmosphere while the surface effects are confined in the first term. The channel in the wing whose weighting function peaks at the surface is used to remove the surface contribution for other channels. Based on Eq. (7.5.19b), we may define the contribution to the brightness temperature caused primarily by the atmosphere for channels 2 to 7 in the

form

$$T_a(\tilde{v}_j) = T_B(\tilde{v}_j) - [T_B(\tilde{v}_1) - T_a(\tilde{v}_1)]a(\tilde{v}_j), \qquad j = 2, 3, \ldots, 7, \quad (7.5.20)$$

where

$$a(v_j) = \frac{\varepsilon_{\tilde{v}_j} T_s T_{\tilde{v}_j}(p_s)[1 - T_d(\tilde{v}_j)/T_s]}{\varepsilon_{\tilde{v}_1} T_s T_{\tilde{v}_1}(p_s)[1 - T_d(\tilde{v}_1)/T_s]}, \quad \text{and} \quad a(\tilde{v}_1) = 1.$$

The statistical method described in Subsection 7.4.3.2 assumes a correlation between the atmospheric temperature and measured data, T_a in the present case, defined by Eq. (7.5.20). It follows that

$$
\begin{aligned}
(\hat{T}_i - \bar{T}_i) &= \sum_j D_{ij}(\hat{T}_{aj} - \bar{T}_{aj}) \\
&= \sum_j D_{ij}[\hat{T}_{Bj} - (\hat{T}_{B1} - \hat{T}_{a1})a_j - \bar{T}_{aj}] \\
&= \sum_{j \neq 1} D_{ij}\hat{T}_{Bj} - \bar{T}_{B1}\sum_j D_{ij}a_j + \sum_j D_{ij}(\hat{T}_{a1}a_j - \bar{T}_{aj}). \quad (7.5.21)
\end{aligned}
$$

Note that T_{B1} is not defined in Eq. (7.5.20), and so the first term contains $j = 2, \ldots, 7$. In matrix notation, we have

$$\hat{\mathbf{T}} = \mathbf{D}'\hat{\mathbf{T}}_B + \mathbf{R}, \qquad (7.5.22)$$

where

$$\mathbf{R} = \bar{\mathbf{T}} + \hat{T}_{a1}\mathbf{Da} - \mathbf{D}\bar{\mathbf{T}}_a, \qquad (7.5.23)$$

and $\mathbf{D}'$ is a matrix whose first column is $-\mathbf{Da}$ and whose remaining columns are the columns of $\mathbf{D}$. The retrieval technique contains elements that are dependent mainly on the atmosphere. Thus, it should be valid over land, water, or mixed surface conditions. $\mathbf{D}$ and $\mathbf{R}$ can be determined from a large number of upper air soundings for a wide range of meteorological conditions that have been achieved over the years, while the brightness temperatures can be calculated for a given atmospheric condition.

Microwave temperature retrieval can be affected by the surface emissivity, as pointed out previously. At the frequencies around 50 GHz, the emissivity over land can vary between about 1 for dry or vegetated land to less than 0.8 for snow cover, bare wet land, rivers, and lakes. The emissivity for oceans varies because of wind-induced foam and surface roughness (see Fig. 7.25). Within the field of view of the microwave instrument, about 25–100 km resolution, the effect of emissivity is relatively small and can be taken into account by empirical approaches as shown above. The effects of nonprecipitating clouds on temperature retrieval are also small. Over the ocean, clouds can either increase or decrease the brightness temperature, depending on their position and LWC. Over high-emissivity land surfaces, clouds normally reduce the brightness temperature, with a maximum effect produced by high clouds having substantial liquid water. Effects due to precipitation are much more pronounced, as illustrated in Liou *et al.* (1981).
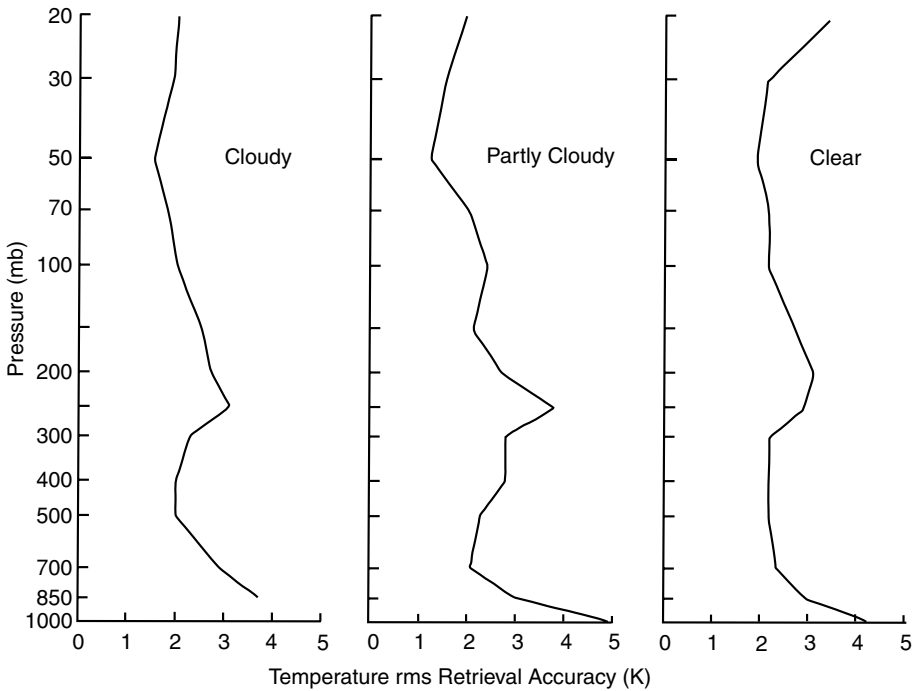
Figure 7.28   Differences between SSM/T retrieval results and the radiosondes stratified according to cloud conditions for November 14–17, 1983, in terms of temperature rms (data taken from Grody, 1993).

Figure 7.28 illustrates an example of the temperature retrieval accuracy based on the SSM/T sounder. The retrieved profiles in terms of the root-mean-square (rms) error are shown relative to radiosonde observations that were collected within a maximum time difference of 3 hours and a 1° latitude–longitude window between November 14 and 17, 1983, for midlatitudes (30–60°N) at pressure levels down to 20 mb (Grody, 1993). Results are shown separately for clear, partly cloudy, and completely cloudy conditions. The rms errors are generally within 2–3 K for pressure levels between 700 and 20 mb, independent of cloud cover. The largest temperature errors occur at pressure levels at which the weighting functions are inadequate and there is no strong correlation between level temperatures and the weighted temperatures sensed by the microwave instrument.

The latest generation of microwave sounders for research and development are the Advanced Microwave Sounding Unit (AMSU) with 12 oxygen channels, flown aboard the NOAA polar-orbiting satellites (1998), and the Air Force SSM/IS instrument. Figure 7.27b displays the weighting functions for the 12 oxygen channels at nadir over land. AMSU also contains channels near the 183 and 22 GHz H_2O lines for water vapor soundings and window channels at 31, 90, and 157 GHz for the inference of precipitation and surface parameters.

7.6   Remote Sensing Using Laser and Microwave Energy

During the 1960s, the advent of the laser as a source of energy opened up a number of possibilities for new remote sensing techniques of probing the atmosphere. Laser energy at optical frequencies is highly monochromatic and coherent. With the development of *Q*-switching techniques, very short pulses of high power could be generated. The recognition of the applicability of high power pulsed laser energy by a number of atmospheric scientists (Schotland, 1969; Collis, 1969) has prompted the development of backscattering lidar techniques for the detection of the composition and structure of clouds, aerosols, and minor gases in the atmosphere. The word *lidar*, which originally stood for *L*ight *D*etection *A*nd *R*anging, is an acronym analogous to radar that utilizes an energy source in the microwave region. In a sense, lidar can best be described as a laser radar. Since the development of laser radar, which employs the same backscattering principle as microwave radar, advanced techniques for atmospheric probes have proved fruitful. These include the use of multiple wavelength lidars for determining the composition of minor gases by means of differential absorption techniques, the use of Doppler techniques for determining the motion of particulates and molecules, the use of depolarization techniques for inferring the water and ice content in clouds, and the use of the Raman scattering technique, in which a weak scattering occurs at a shifted wavelength for water vapor measurements. In line with the discussions of the theory of light scattering and radiative transfer introduced in Chapters 5 and 6, we first present the basic lidar (or radar) equation that is fundamental to all backscattering techniques and then discuss two useful techniques involving the use of absorption and depolarization properties for atmospheric studies. That is followed by a discussion of the use of millimeter (mm)-wave radars for cloud study.

7.6.1   Backscattering Equation: Theoretical Foundation

From the light-scattering theory developed in Sections 3.3 and 5.2, the scattered intensity for a single particle or molecule can be expressed as [see Eqs. (5.2.84) and (5.2.111a,b), also Eq. (3.3.15)]

$$I_{\parallel,\perp}^{s} = I_{\parallel,\perp}^{i} \frac{\sigma_s}{r^2} \frac{P_{2,1}(\Theta)}{4\pi}, \qquad (7.6.1)$$

where the subscripts $\parallel$ (2) and $\perp$ (1) denote the light beam parallel and perpendicular to the scattering plane, respectively, r is the distance at which scattering takes place, σ_s is the scattering cross section, and $P(\Theta)$ is the phase function. For the convenience of the following discussion, we shall neglect the subscripts on the flux density and phase function. The backscattered ($\Theta = \pi$) flux density due to a single particle from Eq. (7.6.1) can be expressed by

$$F^{s}(\pi) = F^{i} \frac{\sigma_s P(\pi)}{r^2 \, 4\pi}. \qquad (7.6.2)$$

For backscattering applications, it is necessary to define the *backscattering cross section* σ_π as the area that, when multiplied by the incident flux density, gives the

total power radiated by an isotropic source such that it radiates the same power in the backward direction as the scatterer. Thus,

$$F^i \sigma_\pi = F^s(\pi)\, 4\pi r^2, \tag{7.6.3}$$

where $4\pi r^2$ represents the surface area of a sphere. It follows that the backscattering cross section is given by

$$\sigma_\pi = \sigma_s P(\pi). \tag{7.6.4}$$

Let P_t denote the transmitted power so that the incident flux density can be expressed by

$$F^i = P_t/A_t, \tag{7.6.5}$$

where A_t is the cross-sectional area at distance r. If A_r is the collecting aperture, then the backscattered power received is given by

$$P_{r0} = F^s(\pi)A_r = \frac{P_t}{A_t} \frac{\sigma_s P(\pi)}{4\pi r^2} A_r. \tag{7.6.6a}$$

In reference to the (volume) scattering coefficient given by Eq. (5.2.116), we may define an average scattering cross section as $\bar{\sigma}_s = \beta_s/N$, where N denotes the particle number density. Hence, after the particle-size distribution integration, the average backscattered power is given by

$$\bar{P}_{r0} = P_t \frac{A_r}{r^2} \frac{P(\pi)}{4\pi} \frac{\bar{\sigma}_s}{A_t}. \tag{7.6.6b}$$

Let the pulse length transmitted by a lidar (or radar) system be Δh, as shown in Fig. 7.29. For a given instant of time, the lidar receiver collects the scattered energy from half of the pulse length, so that the bottom pulse will undergo roundtrip backscattering and return simultaneously as the top pulse. The total number of particles within the effective scattering volume is, therefore, $N A_t \Delta h/2$. Upon utilizing the definition of the volume scattering coefficient, the backscattered power is now given by

$$\bar{P}_{r0} = P_t \frac{A_r\, P(\pi)}{r^2\, 4\pi} \beta_s \frac{\Delta h}{2}. \tag{7.6.6c}$$

During the backscattering event, the energy pulse also undergoes attenuation. On the basis of the Beer–Bouguer–Lambert law introduced in Section 1.4.2, the actual backscattered power at the point of the receiver is

$$\bar{P}_r = \bar{P}_{r0} \exp\left\{-2 \int_0^r \beta_e(r')\, dr'\right\}, \tag{7.6.7a}$$

where 2 represents the roundtrip attenuation effect, $r = 0$ is the position corresponding to $\bar{P}_{r0}$, and β_e is the (volume) extinction coefficient including both scattering and absorption effects. If we insert Eq. (7.6.6c) into Eq. (7.6.7a), the backscattered power observed by the receiver can now be written in the form

$$\bar{P}_r(r) = P_t \frac{A_r\, P(\pi)}{r^2\, 4\pi} \beta_s \frac{\Delta h}{2} \exp\left\{-2 \int_0^r \beta_e(r')\, dr'\right\}. \tag{7.6.7b}$$
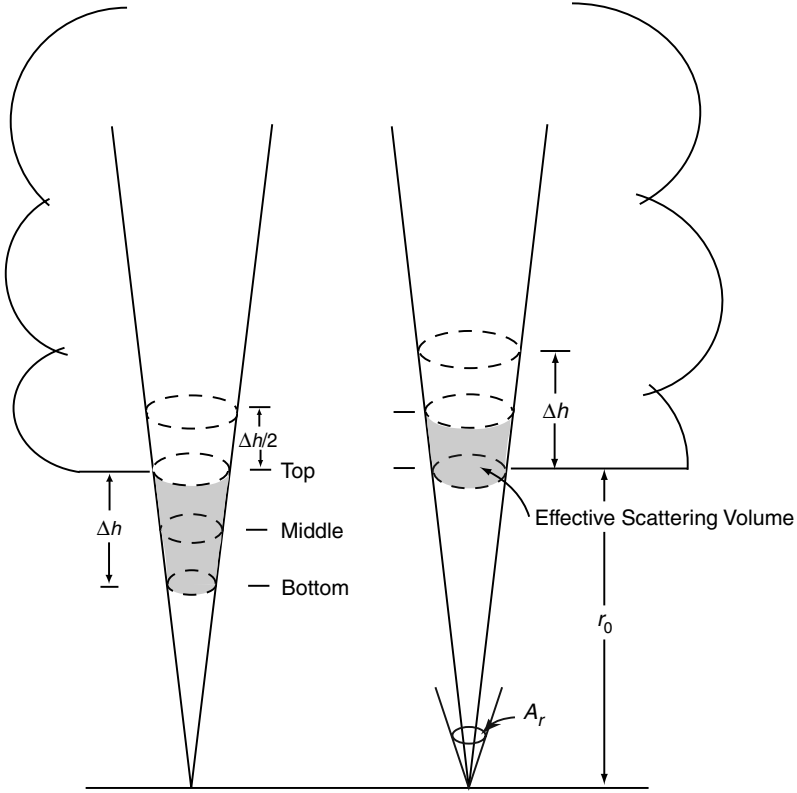
Figure 7.29 The backscattering geometry of a pulsed lidar system where r_0 denotes a reference range, Δh is the pulse length, and A_r is the receiver aperture. The effective length under which the pulsed laser light returns to the receiver is $\Delta h/2$.

In this development, we have neglected the energy gains corresponding to the transmitter and receiver. For lidar or radar applications, it is customary to use the volume backscattering coefficient similar to that given in Eq. (7.6.4), i.e., $\beta_\pi = P(\pi)\beta_s$. Thus, we rewrite Eq. (7.6.7b) to obtain

$$\bar{P}_r(r) = \frac{P_t C A_r \beta_\pi(r) \Delta h}{8\pi r^2} \exp\left\{ -2 \int_0^r \beta_e(r') \, dr' \right\}, \qquad (7.6.7c)$$

where we have added a known instrument factor C to the equation. This is the basic lidar (or radar) equation, where the collecting aperture A_r, the transmitted power P_t, and the pulse Δh are known parameters and the range r is a function of time t. However, there are two unknown parameters, β_π and β_e, which relate to the optical properties and concentration of particles and/or molecules. It is not possible to investigate the information content of the return power in absolute terms unless the volume backscattering coefficient, β_π, and the volume extinction coefficient, β_e, are uniquely correlated.

For Rayleigh scattering, the phase function for unpolarized light in the backscattering direction from Eq. (3.3.11) is $P^R(\pi) = 3(1 + \cos^2 \pi)/4 = 1.5$. Thus, $\beta_\pi^R = 1.5\beta_e^R$. It is clear that the ratio of backscattering to the extinction coefficient for Rayleigh molecules is a constant of 1.5 and is not subject to fluctuations. For a single Lorenz–Mie spherical particle, however, the phase function depends on the size parameter $2\pi a/\lambda$ and is characterized by strong forward scattering (see, e.g., Fig. 5.8). The backscattering phase function $P(\pi)$ as a function of the size parameter fluctuates greatly and is normally less than unity. For a sample of polydispersed spheres, the fluctuations tend to average out (see Figs. 5.13 and 5.15), and useful approximate values can be determined for the term. For water clouds, it has been found that for many cases $\beta_\pi \approx 0.625\beta_e$, a reasonable approximation also applicable to spherical aerosols. In general, it has been assumed that $\beta_\pi \cong a\beta_e^b$, where a and b are certain coefficients to be determined from light-scattering calculations.

The inversion of lidar backscattering data to obtain the volume extinction coefficient profile is the subject of continued research in the lidar field. It begins with the definition of the signal variable defined by

$$S(r) = \ln[r^2 \bar{P}_r(r)]. \tag{7.6.8a}$$

In differential form, we have

$$\frac{dS(r)}{dr} = \frac{1}{\beta_\pi} \frac{d\beta_\pi}{dr} - 2\beta_e(r). \tag{7.6.8b}$$

Having the relation between β_π and β_e established, techniques can be developed to infer $\beta_e(r)$ from $S(r)$, subject to the definition of a reference range *a priori*. The volume extinction coefficients can in turn be related to the sizes and concentrations of aerosols and cloud particles. In the following, we present two specific techniques for the detection of gaseous profiles and for cloud and aerosol studies.

7.6.2   Lidar Differential Absorption and Depolarization Techniques

7.6.2.1   DIFFERENTIAL ABSORPTION TECHNIQUE

The differential absorption lidar (DIAL) uses the gas absorption properties in two wavelengths and requires a tunable laser to produce the peak of an absorption line of the gas of interest and a second wavelength in a low-absorption region. In clear atmospheres, the extinction coefficient for a given wavelength is contributed by the extinction due to aerosols and the absorption caused by the pertinent gas. Thus, we can write

$$\beta_e(\lambda) = \beta_{e,A}(\lambda) + \rho_a k(\lambda), \tag{7.6.9}$$

where ρ_a is the gas density and $k(\lambda)$ is the absorption coefficient. We may select two wavelengths at which the optical properties of aerosols are about the same. Further, we can perform a logarithmic operation on Eq. (7.6.7c) to obtain the normalized backscattered power as follows:

$$\ln[\bar{P}_r(r)/P_t]_i = \ln\left[\frac{CA_r\beta_\pi(r)\Delta h}{8\pi r^2}\right]_i - 2\int_0^r \beta_e(\lambda_i)\, dr, \qquad i = 1, 2. \tag{7.6.10}$$

Since λ_1 is close to λ_2, the scattering and extinction properties of aerosols are about the same so that $\beta_\pi(\lambda_1) \cong \beta_\pi(\lambda_2)$ and $\beta_{e,A}(\lambda_1) \cong \beta_{e,A}(\lambda_2)$. We can then carry out the subtraction operation to obtain

$$\ln \hat{P}_{1,2} \cong -2 \int_0^r \rho_a(r)[k(\lambda_1) - k(\lambda_2)] \, dr, \qquad (7.6.11a)$$

where

$$\hat{P}_{1,2} = [\bar{P}_r(r)/P_t]_1/[\bar{P}_r(r)/P_t]_2. \qquad (7.6.11b)$$

Thus, once the absorption coefficients are known, the backscattered measurements at λ_1 and λ_2 can provide the gas density profile. Recent technology has produced lasers that can be accurately tuned to the absorption lines of various gases such as H_2O, NO_2, SO_2, and O_3. This has led to the development of DIAL systems for the measurement of their profiles in the atmosphere. The capability of the DIAL system has been presented in a summary paper by Browell (1994).

7.6.2.2   PRINCIPLE OF DEPOLARIZATION

In the preceding discussion, we neglected polarization information in the development of the lidar equation. In reference to Eq. (7.6.6a), the transmitted power P_t can be generated to be vertically ($P_{t,\perp}$) or horizontally ($P_{t,\|}$) polarized, while the detector can be devised so that both polarization components ($\bar{P}_{r,\|}, \bar{P}_{r,\perp}$) are measured. This provides additional information about particle characteristics and is referred to as the *depolarization technique*. The principle of depolarization associated with a laser beam that is backscattered by cloud particles can be described by the laws of geometric optics. These laws follow the physical principle that the size of a particle is much larger than the incident wavelength so that light beams can be localized as geometric rays. Each ray that hits the particle will undergo reflection and refraction and will pursue its own specific path along a straight line according to Snell's law at the particle surface (Sections 5.3 and 5.4).

We shall use the geometric optics principle and apply it to the scattering of spherical droplets and hexagonal ice crystals, as shown in Fig. 7.30. Backscattering from a symmetrical sphere can arise from a number of possibilities: the edge rays; a central ray that undergoes external reflection; and two refractions, with the first making the maximum contribution (see Section 5.3). Because no additional reference plane is formed for the 180° backscattered rays, the light beam would retain the polarization state of the incident energy. However, the backscattered energy from a nonspherical particle can be produced by internal reflections that rotate the initial vibration plane of the electric vector and produce depolarization. Shown in Fig. 7.30 are two types of ice crystals: solid column and plate. For these ice crystals to produce backscattering, light rays must undergo internal reflections more than twice, except for normal incidence. In the case of normal incidence, a laser beam transmitting through a plate will retain its polarization state because of symmetry. The incident skew rays that produce backscattering undergo internal reflections that transform the electric vectors from the original reference plane to the planes that contain the incident and refracted rays. Consider a vertically polarized incident laser beam. A cross-polarization component
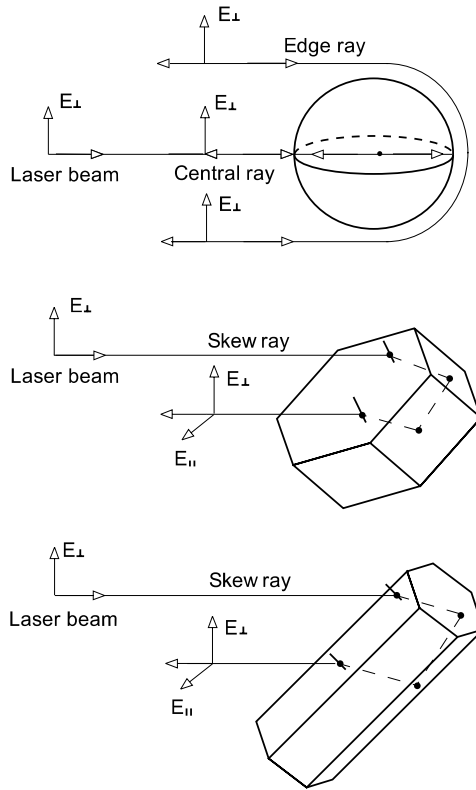
Figure 7.30   Principle of backscattering depolarization from a spherical water droplet, a hexagonal plate, and a solid column. The incident laser beam is vertically polarized. The backscattered beam from a sphere retains the polarization state because of its geometrical symmetry. The backscattered beams from nonspherical particles produce a cross-polarization component for light rays that are not perpendicular to the major axis of the ice particle.

can be produced after the internal reflections. The ratio of this component to the component that retains the same polarization as the incident light beam is referred to as the *backscattering depolarization ratio* defined by

$$\delta = \bar{P}_{r,\parallel}/\bar{P}_{r,\perp}. \tag{7.6.12}$$

The theoretical foundation of depolarization from nonspherical ice crystals was first discussed by Liou and Lahore (1974). Sassen (1976, 1991) presented the depolarization ratio for various types of ice crystals and water droplets derived from laboratory and field studies. For water droplets, this ratio is close to zero, as is predicted from the theory. For ice crystals, the depolarization ratio varies from 50 to 70%, depending on their shape and size. This provides a powerful means of distinguishing between water and ice clouds in the atmosphere. The backscattering depolarization technique can also be used to probe the orientation properties of ice particles. In the case of a vertically pointing lidar involving horizontally oriented plate crystals, the depolarization ratio would be zero because of the symmetry of the two parallel

crystal surfaces with respect to the laser beam. Lidar experiments have shown that the backscattering depolarization ratio in this case is close to zero, whereas it increases significantly as the lidar scans a few degrees off the vertical (Platt *et al.,* 1978).

An example of backscattering depolarization studies of cirrus clouds is illustrated in Fig. 7.31. Sassen and Hsueh (1998) and Freudenthaler *et al.* (1996) presented the depolarization ratios determined from high-resolution 0.532/1.06 μm polarization lidar for contrail cirrus. The former authors showed that the lidar depolarization ratio in persisting contrails ranged from about 0.3 to 0.7; the latter authors observed
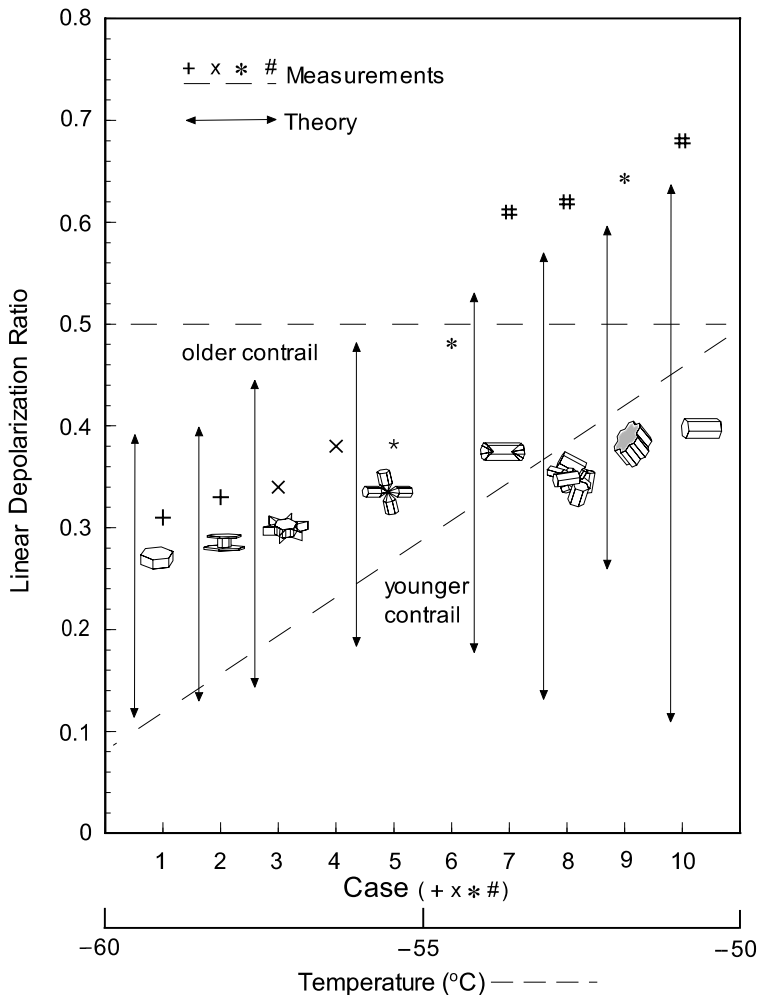
Figure 7.31   Depolarization ratios determined from high resolution polarization lidar for contrail cirrus (Sassen and Hsueh, 1998, case; Freudenthaler *et al.,*1996, temperature) and computed from a unified theory for light scattering by ice crystals (Section 5.4) with shapes ranging from single and double plates, solid and hollow columns, dendrites, bullet rosettes, aggregates, and irregular surface, the sizes of which span from a few micrometers to the geometric optics limit (after Liou *et al.,* 2000).

this ratio from 0.1 to 0.5 for contrails with temperatures ranging from -60 to $-50°C$, depending on the stage of their growth. For purposes of interpretation, displayed in this figure are backscattering depolarization ratios for various ice crystal sizes and shapes computed from the unified theory for light scattering by ice crystals described in Section 5.4. The vertical bars indicate the results for ice crystals of a few micrometers to the geometric optics region. The depolarization ratio generally becomes larger for larger ice particles and reaches a maximum of about 0.6 for size parameters in the geometric optics limit.

One complication in the backscattering and depolarization experiments has been the effect of multiple scattering. Through multiple scattering events, the incident electric vector is transferred from the initial reference plane to the plane of scattering, and therefore, partial depolarization is produced, even for clouds consisting of spherical water droplets. The relative significance of multiple scattering in backscattering experiments involving clouds is generally associated with the field of view of the detector. Multiple backscattering from cloud particles has been a subject of extensive research since the 1970s. The most recent reference on this subject is Wandinger (1998).

7.6.3   Millimeter-Wave Radar for Cloud Study

The conventional meteorological radars typically operate at centimeter (cm) wavelengths (e.g., 10 cm and 3.21 cm radars) to circumvent problems in the interpretation of backscattering signals from precipitating clouds that contain large raindrops and snowflakes on the order of millimeter (mm) to cm sizes. Nonprecipitating clouds generally consist of particles that are much smaller than mm sizes and do not produce significant radar backscattering signals for their detection. Radar meteorology is a well-developed discipline and will not be covered in this text. However, the technical development of mm-wave radar and its application to cloud studies is a subject of contemporary research. In particular, when mm-wave radar data are combined with lidar measurements, comprehensive cloud structure and composition can be inferred.

The selection of wavelength for a radar operated in the earth's atmosphere is restricted to those spectral regions where absorption by atmospheric gases is smaller. In reference to Fig. 7.23, the windows of H_2O and O_2 absorption are located at 35 GHz (8.6 mm, K_a-band), 94 GHz (3.2 mm, W-band), 140 GHz (2.14 mm, F-band), and 220 GHz (1.36 mm, G-band). The first mm-wave radar designed for meteorological use was a 35 GHz system for cloud deck monitoring. It was subsequently equipped with Doppler and polarization capabilities and employed for the observation of clouds. A 94 GHz system with a shorter wavelength was further shown to provide effective observations of the liquid/ice water content of clouds (Lhermittee, 1990). Millimeter-wave radars have two distinct advantages over cm-wave radars in that very narrow beams can be produced with small antenna size and the gain from Rayleigh scattering can reduce the need for high-power transmitters. In recent years, both 35 and 94 GHz radars have been well developed for the detection of nonprecipitating clouds.

Since cloud particles are normally much smaller than mm wavelengths, the Rayleigh scattering theory presented in Section 3.3.1 may be followed. The scattering

cross section for a cloud particle may be expressed by

$$\sigma_s = \frac{128\pi^2}{3\lambda^4} \left(\frac{3}{4\pi N_c} \right)^2 \left| \frac{m^2 - 1}{m^2 + 2} \right|^2, \tag{7.6.13a}$$

where the number density of spherical particles $N_c = 1/V$ and the volume $V = 4\pi a^3/3$. Letting $K = (m^2 - 1)/(m^2 + 2)$, we have

$$\sigma_s = \frac{128\pi^2}{3\lambda^4} a^6 |K|^2. \tag{7.6.13b}$$

Referring to Eq. (7.6.4), noting the Rayleigh backscattering phase function $P^R(\pi) = 1.5$, and using the diameter $D = 2a$ for a cloud particle, the backscattering cross section (in units of cm^2) can then be written in the form

$$\sigma_\pi = \sigma_s \cdot P^R(\pi) = \frac{\pi^5}{\lambda^4} |K|^2 D^6. \tag{7.6.14}$$

Let the cloud particle size distribution be $n(D)$. The backscattering coefficient (in units of cm^{-1}) is then

$$\beta_\pi = \frac{\pi^5}{\lambda^4} |K|^2 Z, \tag{7.6.15}$$

where the radar reflectivity factor

$$Z = \int D^6 n(D) \, dD. \tag{7.6.16}$$

The average return power without accounting for attenuation can now be written in the form

$$\bar{P}_r(r) = \frac{C}{r^2} |K|^2 Z, \tag{7.6.17}$$

where C is a constant associated with the radar characteristics. Measurements of $\bar{P}_r(r)$ versus r allow the calculation of Z, which in turn can be related to the cloud properties.

The radar reflectivity factor defined in Eq. (7.6.16) is related to the particle diameter to the sixth power. As discussed in Section 7.3.5, the liquid (or ice) water content (LWC/IWC) is associated with the particle radius to the third power. Thus, one may correlate the radar reflectivity factor with the cloud LWC/IWC. The 35 GHz cloud radar has been developed specifically for the determination of the vertical profile of IWC in high-level cirrus clouds (Mace *et al.*, 1998). Moreover, with the Doppler technique, some information about the ice-crystal size based on the fall velocity may also be inferred. The development of a combination of the reflectivity and Doppler spectrum technique for the simultaneous retrieval of the vertical profile of IWC and ice-crystal size in cirrus is still in its embryonic stage. In Fig. 7.32, we demonstrate a time series of the retrieved IWC and ice crystal size in terms of D_e, defined in Eq. (5.1.1), as functions of height for a cirrus cloud case observed in Oklahoma on April 18, 1997, based on the backscattering return of a 35 GHz Doppler radar. The cloud top heights were nearly constant between about 10 to 11 km, but the cloud base heights varied significantly. The retrieved IWC and D_e ranged from 0 to 0.6 g m^{-3} and 0 to 170 μm, respectively. Substantial variabilities in both the
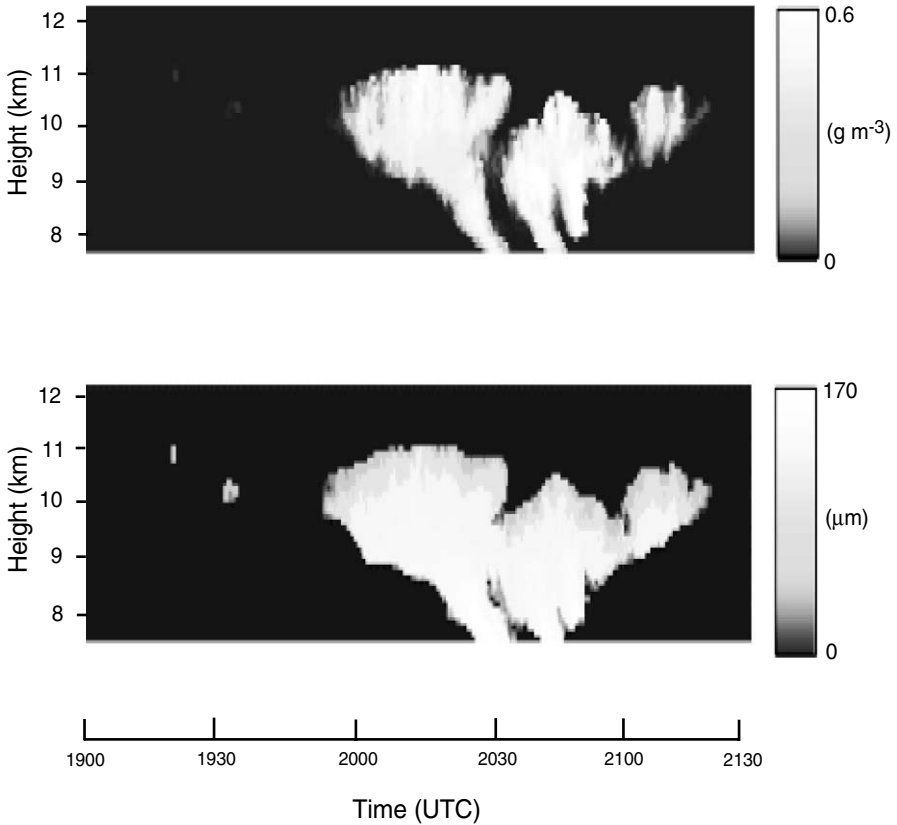
Figure 7.32   Time series of the ice water content (IWC, top panel) and mean effective ice crystal size (D_e, lower panel), determined from the backscattering return of a 35 GHz Doppler radar, as functions of height for a cirrus cloud case observed in Oklahoma on April 18, 1997 (data provided by Gerald Mace of the University of Utah).

vertical and horizontal directions are clearly displayed. It is evident that the successful development of mm-wave cloud radar will revolutionize our understanding of the structure of inhomogeneous clouds, particularly for high-level cirrus.

Exercises

7.1 (a) Derive Eq. (7.2.7) from Eqs. (7.2.5) and (7.2.6) and show that

$$k = \pi (2\pi)^{\nu^* - 2} \int_0^{z_\infty} C(z) \, dz \int_{x_1}^{x_2} \frac{Q_e(x) \, dx}{x^{\nu^* - 1}},$$

where the extinction efficiency Q_e is expressed in terms of the size parameter x. (b) Direct solar radiation measurements are made with a multiple wavelength radiometer. The aerosol optical depths derived from the observations are 0.17

and 0.1 at 0.63 and 0.86 μm, respectively. Assuming a Junge size distribution and a constant k, what would be the shaping factor ν^*?

7.2 Consider the following Fredholm equation of the first kind:

$$g(k) = \int_0^1 e^{-kx} f(x) \, dx,$$

where the kernel is given by a simple exponential function. Let the unknown function be given in the form

$$f(x) = x + 4x\left(x - \frac{1}{2}\right)^2.$$

(a) Derive an analytical expression for $g(k)$ and compute $g(k_i)$ for k_i in the interval $(0, 10)$ using $\Delta k_i = 0.5$ ($i = 1, 2, \ldots, 20$).

(b) Write the integral equation in summation form as

$$g(k_i) = \sum_{j=1}^{20} f(x_j) e^{-k_i x_j} \Delta x_j, \qquad i = 1, 2, \ldots, 20.$$

Letting $\Delta x_i = 0.05$, compute $g(k_i)$ again and compare with those computed from the exact integration.

(c) Let

$$A_{ij} = e^{-k_i x_j} \Delta x_j.$$

Compute $\|A_{ij}\|$, which is a 20×20 matrix. Use the direct linear inversion method to recover $f(x_j)$. Compare the retrieval results with the exact values.

7.3 Prove Eq. (7.2.25) from Eq. (7.2.23) by assuming $M = N = 2$. Using the first, second, and third differences, derive the **H** matrices similar to that shown in Eq. (7.2.26).

7.4 A seven-channel sunphotometer is used to measure aerosol optical depth following the procedure discussed in Section 7.2.1. The measured optical depths corresponding to the wavelengths depicted in Fig. 7.3 are $\tau_1(0.382\mu\text{m}) = 0.645$, $\tau_2(0.451\mu\text{m}) = 0.562$, $\tau_3(0.501\mu\text{m}) = 0.513$, $\tau_4(0.526\mu\text{m}) = 0.491$, $\tau_5(0.778\mu\text{m}) = 0.338$, $\tau_6(0.861\mu\text{m}) = 0.306$, and $\tau_7(1.060\mu\text{m}) = 0.249$. Using the weighting functions given in this figure, determine the aerosol size distribution from the following procedures:

(a) Use Eq. (7.2.12) and expand $f(a)$ in a seven-term Legendre polynomial defined by

$$P_j(a) = \frac{1}{2^j j!} \frac{d^j}{da^j} (a^2 - 1)^j.$$

(b) Then, from Eq. (7.2.13b), compute

$$A_{ij} = \int_{a_1}^{a_2} P_j(a) K_i(a) da, \qquad i = 1, 2, \ldots, 7,$$

where $a_1 = 0.01$ μm and $a_2 = 1$ μm. Use the data presented in Table 7.2 and a quadrature integration method in the computation.

Table 7.2

Weighting Functions as Functions of Aerosol Radius for Seven Sunphotometer Wavelengths

Radius (μm)	Weighting functions						
	1	2	3	4	5	6	7
0.0100	4.4328	2.2811	1.4978	1.2327	0.2575	0.1717	0.0747
0.0176	13.7007	7.0492	4.6281	3.8086	0.7953	0.5302	0.2307
0.0260	29.9713	15.4296	10.1313	8.3375	1.7407	1.1602	0.5049
0.0308	42.0547	21.6767	14.2381	11.7184	2.4469	1.6309	0.7097
0.0466	93.8568	49.0855	32.3937	26.7002	5.5989	3.7324	1.6241
0.0509	110.4079	58.2449	38.5510	31.8052	6.6892	4.4599	1.9409
0.0690	177.1635	100.1537	68.0051	56.5812	12.2394	8.1761	3.5645
0.0766	198.6910	117.1921	81.0726	67.8926	15.0261	10.0546	4.3907
0.0878	222.1855	138.4621	99.1376	84.1119	19.5691	13.1463	5.7637
0.0989	244.8080	153.7768	113.6846	97.9175	24.3999	16.4917	7.2761
0.1013	251.0553	156.6501	116.4091	100.5890	25.5108	17.2721	7.6341
0.1107	278.9088	167.4753	125.3450	109.3831	29.8075	20.3415	9.0670
0.1273	309.0414	193.7464	139.8560	121.7655	37.3108	25.9747	11.8390
0.1306	307.8837	200.0057	143.3598	124.3373	38.7264	27.0920	12.4191
0.1496	287.9718	221.6949	168.0708	143.8293	45.9078	33.1677	15.8485
0.1586	288.5376	218.4273	176.9670	154.0849	48.6430	35.7095	17.4849
0.1668	293.5934	212.1231	179.6682	160.7122	50.7921	37.7829	18.9532
0.1759	292.5142	206.8395	177.1622	162.9790	52.8937	39.7875	20.5186
0.2157	246.2814	203.6015	169.9123	151.7108	63.7010	46.7642	26.1580
0.2357	221.1176	182.9026	167.6034	155.3636	70.7781	51.2328	28.1459
0.2469	201.5677	177.9200	159.1576	152.3555	73.4846	54.2184	29.1279
0.2549	192.6196	176.6381	152.7078	147.4533	74.3904	56.3492	29.8385
0.2600	189.4106	175.0724	149.2663	143.8085	74.4998	57.5937	30.3113
0.2777	172.3674	159.3578	143.7655	133.2944	72.8265	60.4652	32.1875
0.2871	156.2557	148.8443	142.3785	130.9186	71.3910	60.8324	33.3749
0.2917	148.8346	144.4151	140.8010	130.4095	70.7245	60.7327	34.0098
0.3075	133.4110	135.7173	129.9356	127.2397	69.2935	59.4388	36.2900
0.3245	119.9005	126.8022	116.7393	116.6808	69.6569	57.5826	38.5157
0.3372	101.8229	113.8690	111.0767	107.9117	70.6203	56.6867	39.6402
0.3521	87.9238	100.7208	107.1272	101.2790	70.9368	56.5918	40.1344
0.3882	60.6246	81.6000	83.1148	87.1008	64.9331	57.9546	38.6334
0.4093	52.7835	65.6209	76.3747	74.6244	61.1072	56.2177	37.5694
0.4263	43.3359	61.1699	69.2994	69.8766	59.7750	53.5649	37.2795
0.4441	32.8936	52.4110	58.1053	64.5868	59.1438	50.8691	37.5811
0.4628	32.5212	41.2741	50.9002	54.4527	56.9318	49.1611	38.1275
0.4953	21.5198	34.6967	41.5344	45.1617	49.9987	48.1017	37.6474
0.5085	23.7100	28.7729	35.4682	42.3528	47.6895	46.9398	36.7315
0.5286	19.8040	23.0721	30.7868	34.1439	45.7240	43.9804	35.0077
0.5419	17.9112	23.8040	30.2158	29.7947	44.8635	41.7830	33.9158
0.5681	19.3692	17.9502	22.3759	27.5200	41.0542	38.4228	32.4880
0.6218	19.5171	14.4908	16.2054	16.9793	32.4441	34.4953	31.2234
0.6679	19.6098	13.9251	13.7338	12.4354	27.7156	28.0536	27.4974
0.7033	17.9602	13.5937	10.6527	12.3184	22.3268	25.8595	25.1727
0.7363	16.7441	13.8903	11.4802	9.7987	20.5210	23.0045	24.2301
0.7768	14.0616	13.6846	10.5095	10.2743	16.2295	18.3615	21.8955

Continues

Continued

Radius	Weighting functions						
(μm)	1	2	3	4	5	6	7
0.8101	13.0399	13.0259	11.3784	9.3696	13.0756	16.8683	19.2823
0.8485	9.7714	12.8928	11.9151	10.2819	12.1259	14.3272	17.4424
0.8695	8.8943	12.0394	11.2795	9.7739	10.3275	12.3727	16.9763
0.8917	7.7516	11.1963	10.6176	10.8465	8.5943	10.8745	16.0946
0.9151	7.2615	10.1764	11.0882	10.3081	7.7314	10.4032	14.5823
0.9396	6.5278	9.2237	10.6382	9.5603	7.9324	9.8656	12.9847
0.9523	6.7532	9.3616	9.8044	10.1288	7.3905	9.0824	12.3006
0.9784	6.3343	7.9969	9.5029	9.6135	6.1033	7.4553	11.3872
0.9918	6.2839	7.4044	9.1160	9.3268	5.5344	6.7934	11.1889
1.0055	6.2318	7.1540	8.9166	8.7280	5.2022	6.3777	11.0159

(c) Based on Eq. (7.2.27), compute $\mathbf{f}$ ($j = 1, 2, \ldots 7$) by using the $\mathbf{H}$ derived for the second difference obtained from Exercise 7.3. The aerosol radii corresponding to the peaks of the weighting function are, respectively, $a_1 = 0.127$, $a_2 = 0.150$, $a_3 = 0.167$, $a_4 = 0.176$, $a_5 = 0.260$, $a_6 = 0.287$, and $a_7 = 0.352$ for wavelengths ranging from 0.382 to 1.060 μm. Use $\gamma = 10^{-3}$ and 10^{-6} in the inversion exercise.

(d) Compute the column aerosol size distribution from Eq. (7.2.9a) by assuming $v^* = 3$ and compare your results with those displayed in Fig. 5.1.

7.5 Observations from satellite visible imagery have shown that ships can influence the composition and radiative properties of shallow clouds (stratus and stratocumulus) over the oceans via their stack effluents. It is hypothesized that the additional aerosols serve as effective condensation nuclei upon which small water droplets form. This is referred to as the indirect aerosol effect in climate studies. Consider Eqs. (7.3.13b) and (7.3.13c) and use a mean effective radius $\bar{a}$ in the integrand. Define the total number density of water droplets as $N = \int n(a) \, da (\# \text{ cm}^{-3})$. What would be the increase in optical depth if N increases by a factor of 2? Remote sensing of the optical depths and droplet sizes of disturbed and pristine stratiform clouds over the oceans is a subject of considerable importance for the study of aerosol–cloud interactions.

7.6 Given the temperature profile and transmittances for the six VTPR channels (669.0, 676.7, 694.7, 708.7, 723.6, and 746.7 cm^{-1}) in Table 7.3:

(a) Compute and plot the weighting function $\Delta T_i(p)/\Delta \ln p$ as a function of the pressure on a logarithmic scale. What is the physical meaning of the weighting function?

(b) Assuming that the calculated radiances are the values observed from the NOAA 4 VTPR instrument, recover the temperature profile from these radiances utilizing the relaxation method outlined in Subsection 7.4.3.1. Use a linear

Table 7.3

Atmospheric Profiles and Transmission Functions for VTPR Channels

Pressure mb	Temperature (K)	Transmittances					
		1	2	3	4	5	6
0.8	270.7	.9198	.9817	.9890	.9922	.9931	.9968
1.4	265.0	.8846	.9733	.9837	.9891	.9906	.9953
2.1	256.4	.8429	.9637	.9777	.9861	.9879	.9940
3.1	248.3	.7979	.9508	.9704	.9817	.9848	.9925
4.4	241.9	.7520	.9344	.9612	.9783	.9810	.9906
5.9	238.2	.7061	.9139	.9497	.9732	.9763	.9885
10.3	232.7	.6094	.8591	.9188	.9597	.9645	.9828
13.1	228.8	.5562	.8239	.8980	.9506	.9570	.9790
16.5	226.3	.5001	.7831	.8740	.9403	.9485	.9747
20.4	222.5	.4423	.7369	.8470	.9290	.9392	.9701
24.9	221.1	.3840	.6853	.8168	.9167	.9290	.9652
30.2	219.5	.3266	.6291	.7831	.9033	.9180	.9600
36.1	219.0	.2716	.5691	.7458	.8887	.9065	.9546
42.9	218.5	.2203	.5064	.7051	.8728	.8945	.9489
50.5	217.9	.1738	.4424	.6609	.8555	.8821	.9431
59.1	217.4	.1329	.3785	.6136	.8366	.8695	.9370
68.6	216.8	.0980	.3160	.5638	.8162	.8567	.9307
79.2	217.3	.0693	.2563	.5119	.7941	.8437	.9241
90.9	218.0	.0468	.2008	.4584	.7699	.8304	.9173
103.8	218.8	.0299	.1510	.4043	.7436	.8163	.9101
117.9	219.7	.0179	.1080	.3508	.7152	.8029	.9026
133.3	220.7	.0100	.0727	.2988	.6847	.7884	.8946
150.2	221.7	.0052	.0456	.2496	.6520	.7731	.8861
168.5	222.6	.0024	.0264	.2042	.6175	.7570	.8771
188.4	223.6	.0010	.0139	.1634	.5812	.7397	.8674
209.9	225.2	.0004	.0066	.1275	.5431	.7212	.8569
233.1	227.5	.0001	.0028	.0968	.5033	.7011	.8454
258.0	229.7	.0000	.0011	.0711	.4615	.6792	.8325
284.8	230.2	.0000	.0004	.0508	.4195	.6561	.8187
313.6	231.8	.0000	.0001	.0354	.3782	.6321	.8043
344.3	232.8	.0000	.0000	.0237	.3365	.6064	.7883
377.2	234.2	.0000	.0000	.0151	.2940	.5782	.7701
412.2	235.5	.0000	.0000	.0090	.2514	.5475	.7493
449.5	236.9	.0000	.0000	.0050	.2099	.5142	.7253
489.2	241.6	.0000	.0000	.0026	.1706	.4785	.6992
531.2	245.4	.0000	.0000	.0012	.1343	.4402	.6687
575.8	249.0	.0000	.0000	.0005	.1017	.3993	.6326
623.1	252.8	.0000	.0000	.0002	.0740	.3565	.5917
673.0	256.8	.0000	.0000	.0000	.0516	.3127	.5467
725.7	260.5	.0000	.0000	.0000	.0346	.2689	.4983
781.3	263.9	.0000	.0000	.0000	.0221	.2261	.4476
839.9	267.5	.0000	.0000	.0000	.0134	.1852	.3952
901.5	272.1	.0000	.0000	.0000	.0076	.1456	.3371
966.3	277.0	.0000	.0000	.0000	.0039	.1064	.2682
1019.8	279.5	.0000	.0000	.0000	.0019	.0770	.2099

interpolation between the recovered temperatures and use the true temperatures for the surface and the top layer. Plot the retrieved temperature profile on a logarithmic scale and compare it with the true temperature profile.

Suggested Reading

Baker, J. (1990). *Planet Earth: The View from Space*. Harvard University Press, Cambridge, MA. This book, written for the lay public and beginning students interested in remote sensing, contains illustrative presentations of the objectives of remote sensing and the key atmospheric and surface parameters that can be determined from various types of satellite systems.

Houghton, J. T., Taylor, F. W., and Rodgers, C. D. (1984). *Remote Sounding of Atmospheres*. Cambridge University Press, Cambridge, U.K. Chapter 7 provides a systematic discussion of retrieval theory, particularly for temperature and minor gas profiles.

Janssen, M. A., ed. (1993). *Atmospheric Remote Sensing by Microwave Radiometry*. Wiley, New York. This monograph collects important information on the remote sensing of the atmosphere and the surface based on microwave emission. Chapters 3 and 6 are specifically relevant to the discussion presented in the text.

Kidder, S. Q., and Vonder Haar, T. H. (1995). *Satellite Meteorology*. Academic Press, San Diego. Chapter 2 contains a useful discussion of satellite orbits and viewing geometries and also gives a comprehensive list of meteorological satellite programs up to 1994.

Stephens, G. L. (1994). *Remote Sensing of the Lower Atmosphere*. Oxford University Press, New York. This is a useful text that covers remote sensing subjects of interest in atmospheric sciences. Specifically, Chapter 8 provides a concise presentation of active remote sensing of atmospheric particulates using radar and lidar.

Twomey, S. (1977). *Introduction to the Mathematics of Inversion in Remote Sensing and Indirect Measurements*. Elsevier, New York. Twomey's book presents the fundamental theory of, and background materials on, the inversion of radiometric measurements.